Consideration of real-time effects for improved coordination of multi-messenger campaigns

Patrick Reichherzer

Thèse de doctorat

NNT : 2022UPASP068

Consideration of real-time effects for improved coordination of multi-messenger campaigns

Prise en compte des effets temporels pour une meilleure coordination des observations multi-messagers

Thèse de doctorat de
l'université Paris-Saclay et de la Ruhr-Universität Bochum

École doctorale n° 576, Particules, Hadrons, Énergie et Noyau : Instrumentation, Imagerie, Cosmos et Simulation (PHENIICS)
Spécialité de doctorat : Astroparticules et Cosmologie
Graduate School : Physique. Référent : Faculté des sciences d'Orsay

Thèse préparée dans les unités de recherche **Département de Physique des Particules** (Université Paris-Saclay, CEA) et **Institut für Theoretische Physik IV** (Ruhr-Universität Bochum), sous la direction de **Fabian SCHÜSSLER**, Ingénieur-Chercheur, et la co-direction de **Julia TJUS**, Professeure

Thèse soutenue à Bochum (Allemagne), le 1er Juillet 2022, par

Patrick REICHHERZER

Composition du jury

Heiko KRABBE Professeur, Ruhr-Universität Bochum, Allemagne	Président
Markus AHLERS Professeur, Københavns Universitet, Danemark	Rapporteur & Examinateur
Kumiko KOTERA Directrice de recherche (HDR), IAP/CNRS, France	Rapporteure & Examinatrice
Julia TJUS Professeure, Ruhr-Universität Bochum, Allemagne	Co-directrice de thèse & Rapporteure
Tiina SUOMIJÄRVI Professeure, Université Paris-Saclay, France	Examinatrice
Fabian SCHÜSSLER Ingénieur-Chercheur, Université Paris-Saclay, France	Directeur de thèse

université PARIS-SACLAY

ÉCOLE DOCTORALE
Particules, hadrons, énergie et noyau : instrumentation, imagerie, cosmos et simulation (PHENIICS)

RUB

Title : Consideration of real-time effects for improved coordination of multi-messenger campaigns
Keywords : Astrophysics, multi-messenger, multi-wavelength, real-time effects, high-energy, blazar

Abstract : The joint observation of gravitational waves and the electromagnetic counterparts of a binary neutron star merger and the compelling evidence for a blazar being a source of high-energy neutrino in 2017 ushered in the era of multi-messenger astronomy. The real-time effects of cosmic-messenger propagation on observable multi-messenger signatures are investigated, whose implications are derived and confirmed by numerical tools developed and improved in this thesis. In addition, the holistic platform Astro-COLIBRI has been developed for coordinating multi-messenger campaigns, which facilitated the detection of the most distant active galaxy with a very-high-energy signal conducted within the thesis. The acquired insights and developed tools contribute to improved coordination of multi-messenger campaigns.

Titel : Berücksichtigung von Echtzeiteffekten zur besseren Koordination von Multi-Messenger-Kampagnen
Schlagwörter : Astrophysik, Multi-Messenger, Multi-Wellenlänge, Echtzeiteffekte, Hochenergie, Blazar

Abstrakt : Die gemeinsame Beobachtung von Gravitationswellen und Photonen bei der Verschmelzung eines binären Neutronensterns sowie der stichhaltige Hinweis auf einen Blazar als Quelle hochenergetischer Neutrinos im Jahr 2017 trugen wesentlich dazu bei, die Ära der Multi-Messenger-Astronomie einzuläuten. Die Auswirkungen von Echtzeiteffekten der Propagation kosmischer Messenger auf beobachtbare Multi-Messenger-Signaturen werden hergeleitet und mit Hilfe der in dieser Arbeit entwickelten und verbesserten numerischen Tools bestätigt. Darüber hinaus wurde die Plattform Astro-COLIBRI zur Koordinierung von Multi-Messenger-Kampagnen entwickelt, die den Nachweis der am weitesten entfernten aktiven Galaxie mit einem sehr energiereichen Signal im Rahmen dieser Arbeit ermöglichte. Die gewonnenen Erkenntnisse und entwickelte Software tragen zu einer verbesserten Koordination von Multi-Messenger-Kampagnen bei.

Titre : Prise en compte des effets temporels pour une meilleure coordination des observations multi-messagers
Mots clés : Astrophysique, multi-messager, multi-longueur d'onde, effets temporels, haute énergie, blazar

Résumé : L'observation conjointe des ondes gravitationnelles et des contreparties électromagnétiques de la fusion d'une étoile à neutrons binaire et l'indice qu'un blazar est une source de neutrino de haute énergie en 2017 ont inauguré l'ère de l'astronomie multi-messagers. Les effets en temps réel de la propagation des messagers cosmiques sur les signatures multi-messagers sont étudiés, dont les implications sont dérivées et confirmées par des outils numériques développés et améliorés dans cette thèse. De plus, la plateforme holistique Astro-COLIBRI a été développée pour coordonner les campagnes multi-messagers, ce qui a facilité la détection d'une galaxie active la plus lointaine avec un signal de très haute énergie réalisée dans le cadre de la thèse. Les connaissances acquises et les outils développés contribuent à une meilleure coordination des campagnes multi-messagers.

Contents

Chapter 1

Introduction

1.1 Scientific Drivers & Scope

Joint measurements of gravitational waves (GWs) [4] or neutrinos [89] and their electromagnetic counterpart provided recently deep insights into transient phenomena, thus contributing significantly to ushering in the era of multi-messenger astronomy. The temporal and spatial correlation of detections of one neutrino and gamma-rays with 3σ significance hints at the source's capability of creating high-energy cosmic rays, another astrophysical messenger, which is a critical intermediate in producing those neutrinos. Despite these breakthroughs, a complete understanding of particle production, propagation, and escape within astrophysical sources of high-energy messengers is still missing. To further constrain analytical theories, extended observations of transient phenomena are needed, which cover a wide range of the electromagnetic spectrum in addition to neutrinos and GWs, as each messenger provides insights into specific source regions and physical processes. In light of the lack of predictive capabilities for transient phenomena, it is necessary to react spontaneously and immediately to transient event alerts with follow-up observations. This thesis aims to improve the coordination of follow-up campaigns with a twofold approach:

1. First, the thesis investigates real-time effects that improve the understanding of timescales of transient phenomena. In this pursuit, the present study invokes another layer of complexity in analytical and numerical modeling of transient phenomena by explicitly considering the real-time propagation effects of messenger in sources and their subsequent journey to Earth.

2. The development of Astro-COLIBRI as a holistic planning tool for follow-up observations is presented. Its use in the High Energy Stereoscopic System (H.E.S.S.) and its contribution to successfully detecting the most distant very-high-energy (VHE) signal from an active galactic nuclei (AGN) are highlighted.

1.2 Declaration

This dissertation is based on my research in the context of my bi-nationally supervised Ph.D. (Cotutelle) at the Ruhr-Universität Bochum and the Université Paris-Saclay. My work is original, except when referenced to other work. The research results presented summarize my findings published in journals during my doctoral studies and highlight their key messages in the overall context of the research topic as listed below, sorted by submission date. Corresponding authors are marked with the sign *. For publications that I did not lead, I provide a brief description of my contribution.

1. L. Schlegel*, A. Frie, B. Eichmann, **P. Reichherzer**, and J. Becker Tjus, "Interpolation of Turbulent Magnetic Fields and Its Consequences on Cosmic Ray Propagation", *The Astrophysical Journal*, 889, 2, 2020 — doi:10.3847/1538-4357/ab643b,
   where I developed statistical criteria to quantify the effect of turbulence interpolation on cosmic-ray propagation. Furthermore, I supported L. Schlegel in finding the final simulation setup;

2. **P. Reichherzer***, J. Becker Tjus, E.G. Zweibel, L. Merten, and M.J. Pueschel, "Turbulence-level dependence of cosmic ray parallel diffusion", *Monthly Notices of the Royal Astronomical Society*, 498, 4, 2020
   — doi:10.1093/mnras/staa2533;

3. **P. Reichherzer*** et al., "Astro-COLIBRI—The COincidence LIBrary for Real-time Inquiry for Multimessenger Astrophysics", *The Astrophysical Journal Supplements Series*, 256, 1, 2021 — doi: 10.3847/1538-4365/ac1517;

4. H. Ashkar*, ..., **P. Reichherzer** et al., "The H.E.S.S. gravitational wave rapid follow-up program", *Journal of Cosmology and Astroparticle Physics*, 3, 2020 — doi:10.1088/1475-7516/2021/03/045,
   where I contributed with Astro-COLIBRI developements;

5. **P. Reichherzer***, L. Merten, J. Dörner, J. Becker Tjus, M.J. Pueschel, and E.G. Zweibel, "Regimes of cosmic-ray diffusion in Galactic turbulence", *SN Applied Sciences*, 4, 15, 2022 — doi:10.1007/s42452-021-04891-z;

6. **P. Reichherzer***, J. Becker Tjus, E. G. Zweibel, L. Merten, and M. J. Pueschel, "Anisotropic cosmic-ray diffusion in isotropic Kolmogorov turbulence", *Monthly Notices of the Royal Astronomical Society*, 514, 2, 2022
   — doi:10.1093/mnras/staa2533.

7. **P. Reichherzer*** and J. Becker Tjus, "PropPy — Correlated random walk propagation of cosmic rays in magnetic turbulence", *Journal of Open Source Software*, 7, 74, 2022 — doi:10.21105/joss.04243,

8. J. Becker Tjus, ..., **P. Reichherzer** et al., "Propagation of cosmic rays in plasmoids of AGN jets – implications for multimessenger predictions", *MDPI Physics*, 4, 2, 473-490, 2022 — doi:10.3390/physics4020032,
   where I developed the theory for quantifying the time needed to achieve certain levels of diffusivity. I applied the timescales needed for the transition to diffusive propagation to plasmoid settings.

9. J. Dörner, **P. Reichherzer**, J. Becker Tjus, and V. Heesen, "Cosmic-ray electron transport in the galaxy M 51", submitted to A&A (2022) — arXiv:2206.11670,
   where I developed the model for the energy-independent diffusion coefficients of cosmic-ray electrons employed in the study.

23 additional co-authorships are held, 14 of which in the context of the H.E.S.S. Collaboration, eight in the IceCube Collaboration, and one in the CTA Collaboration. I have presented my results at numerous international conferences, workshops, and symposia in invited talks, contributed talks, or posters, which resulted in the publication of three proceedings as first author and four as co-author (only counting few-author proceedings with my significant contribution).
Two more publications with my significant contributions are currently in the planning stages, one for CRPropa and one for the H.E.S.S. Collaboration.

Patrick Reichherzer
Bochum, Germany
01. July 2022

1.3 Structure

This thesis is structured as follows:

1. **Introduction**
   Chapter 1 introduces this thesis's scientific drivers and scope. This chapter also serves to declare my work published in scientific journals. The present outline structures the individual papers in the overall context of the thesis.

2. **Real-Time Multi-Messenger Astrophysics**
   Chapter 2 shall introduce the concept of real-time multi-messenger Astrophysics. This approach combines information about messengers from different source regions in a holistic approach to provide a comprehensive picture of transient phenomena. In the pursuit of this introductory chapter, the individual messengers shall be introduced along with their specific set of physics that contribute to the multi-messenger approach. Subsequently, transient astrophysical sources are reviewed, whose nature is explored in multi-messenger campaigns. Finally, the chapter concludes with an introduction to real-time effects that can explain temporal variations of the observed transient phenomena.

3. **Real-Time Multi-Messenger Tools**
   The first part of Chapter 3 summarizes tools used to plan and conduct multi-messenger follow-up campaigns of transient events. This overview also serves to illustrate the patchwork of different specific tools in the multi-messenger ecosystem. The chapter discusses how the development of Astro-COLIBRI facilitates the coordination of follow-up observations by providing a user-friendly platform. The usage of Astro-COLIBRI is illustrated by the example of the detection of the most distant very-high-energy AGN. The second part, Section 3.2, of the chapter discusses numerical simulation codes, focusing on CRPropa and PropPy, as both can resolve the difficult-to-evaluate trajectories of charged particles. Emphasize is put on essential aspects for the study of multi-messenger signatures.

4. **Cosmic-Ray Transport in Astrophysical Sources**
   Chapter 4 deals with the physics of charged particles in astrophysical sources. The focus is on the transport properties of charged particles. The influence of the source environment on the escape times and spectrum of charged particles is illustrated. Inheritance of these properties to secondary particles has far-reaching consequences for multi-messenger signals, including real-time effects, and must therefore be considered in multi-messenger campaigns. In discussing this aspect in detail, new analytical expressions for the expected escape times of charged particles from source regions are derived and confirmed by numerical simulations.

5. **Journey of Messengers from Sources to Earth**
   The findings obtained in Chapter 4 are generalized for the transport from the

sources to the Earth in Chapter 5. This includes the presentation of a criterion for diffusive transport of charged particles depending on particle energies and source distances. The study helps estimate at what energies cosmic rays may be correlated with sources and thus potentially contribute to the multi-messenger approach.

6. **Conclusions & Outlook**
   Chapter 6 summarizes how the consideration of real-time effects and the usage of Astro-COLIBRI improves the planning of multi-messenger campaigns. The most important findings are elaborated on and provided with an outlook on future work.

Chapter 2

Real-Time Multi-Messenger Astrophysics

2.1 Multi-Messenger Approach

After decades of progress in observing techniques with significant breakthroughs in understanding the observable properties of astrophysical sources, a fundamentally new research domain has recently revealed its first results: real-time multi-messenger astrophysics. While observations by eye and basic telescopes were historically constrained to optical-wavelength photons, we explore the Universe nowadays in its entire wealth manifested in the complete electromagnetic spectrum and with complementary messengers. Combining these pieces of messenger information from different source regions in a holistic approach yields a comprehensive picture. This approach is shown schematically in Figure 2.1, where different messenger originating from a source can be observed at Earth. An observatory, however, comes with characteristics rooted in the underlying detector physics that allow for observations of only one messenger within a constrained energy window. This aspect draws parallels to a Buddhist parable, in which a group of blind men is supposed to examine an elephant. The analogy arises from the fact that each of the blind men can study only one part of the elephant's body, similar to how an observatory can observe only one aspect of a transient phenomena. This limitation within the realm of multi-messenger astrophysics requires the observation of a transient event with several telescopes simultaneously, which coins the phrase real-time multi-messenger astrophysics. To achieve simultaneous observations, a sophisticated real-time communication between the observatories is necessary, whose details shall see more emphasis in Chapter 3. Whereas the blind men in the parable accuse each other of lying because of their different observations, multi-messenger astrophysics uses complementary observations to come to a conclusive overall picture of the event. The multi-messenger astrophysics portfolio is introduced below.

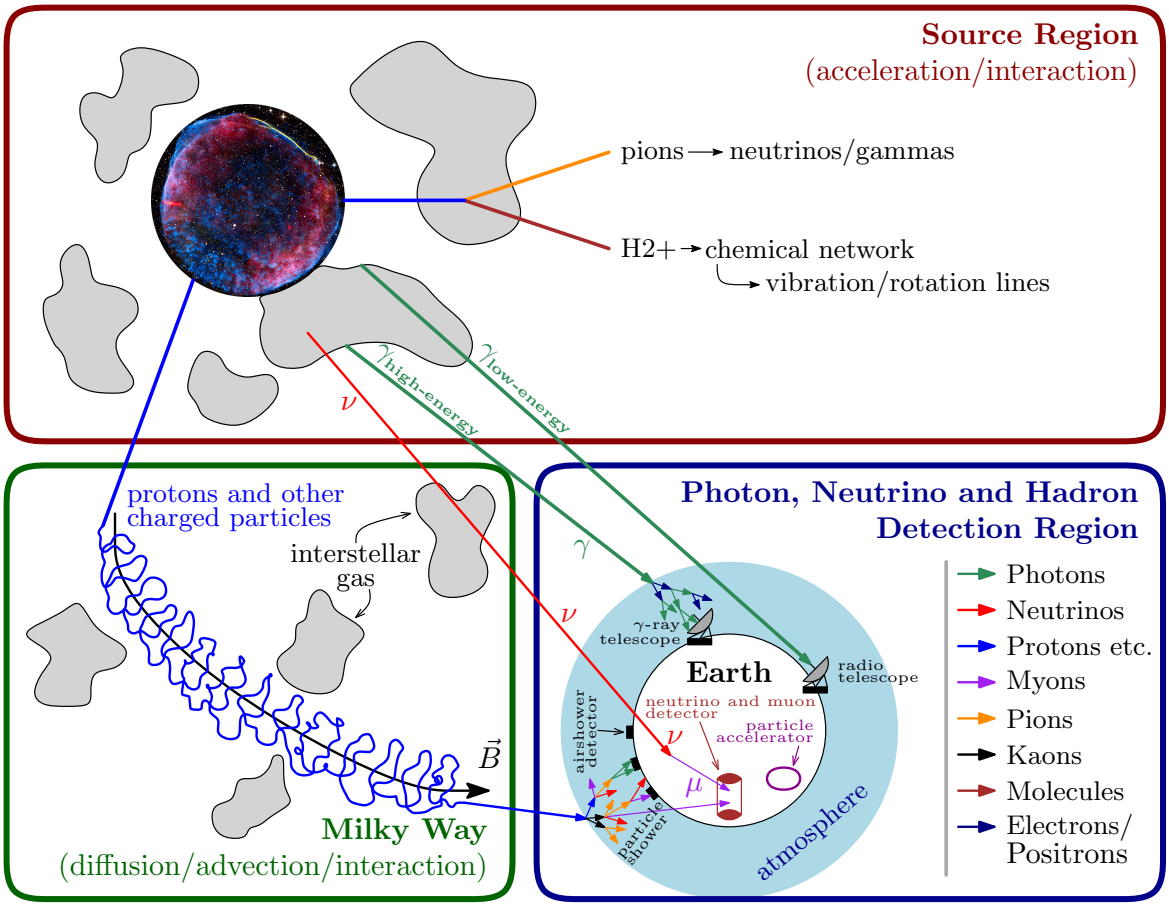

Figure 2.1: Schematic view of the non-thermal multi-messenger emission from astrophysical particle sources. Taken from [24].

Cosmic Rays The term cosmic rays (CRs) encapsulates different types of charged particles. The CR composition above GeV energies is dominated by protons supplemented by a smaller contribution from heavier nuclei and a minor component of electrons and positrons [189]. The acceleration of CRs up to energies from a few GeV up to beyond 10^{20} eV is described by different acceleration mechanisms, including both Fermi mechanisms. During Fermi-acceleration mechanisms, particles accumulate energy in subsequent acceleration processes in turbulent magnetic fields in e.g. collisionless shock fronts. This mechanism leads to a power-law energy spectrum close to E^{-2}. Deviations from this theoretical prediction in observations of the cosmic-ray spectrum arise from complex plasma-physical effects during the transport and the acceleration processes that modify the simplified Fermi-mechanism predictions (e.g., see mechanisms described in [26, 53]). The observed cosmic-ray energy spectrum $\mathrm{d}N/\mathrm{d}E = \Phi(E) \propto E^{-\alpha_{\mathrm{CR}}}$ above $\sim 10\,\mathrm{GeV}$ can approximately be described as a

broken-power law with three different regimes [24],

$$\alpha_{\mathrm{CR}} \approx \begin{cases} 2.67 \pm 0.02 & 10 < E/\mathrm{GeV} < 10^{6.4} \\ 3.07 \pm 0.07 & 10^{6.4} < E/\mathrm{GeV} < 10^{9.7} \\ 2.33 \pm 0.33 & E/\mathrm{GeV} > 10^{9.7} \end{cases} . \tag{2.1}$$

Figure 2.2 shows the cosmic-ray flux with indications of the so-called knee and ankle, which label the transitions between the three regimes. Note that over the last years, measurements with increasing resolution have shown that more spectral features are present, such as a 2nd knee at energies around a few 10^5 TeV. The formation of

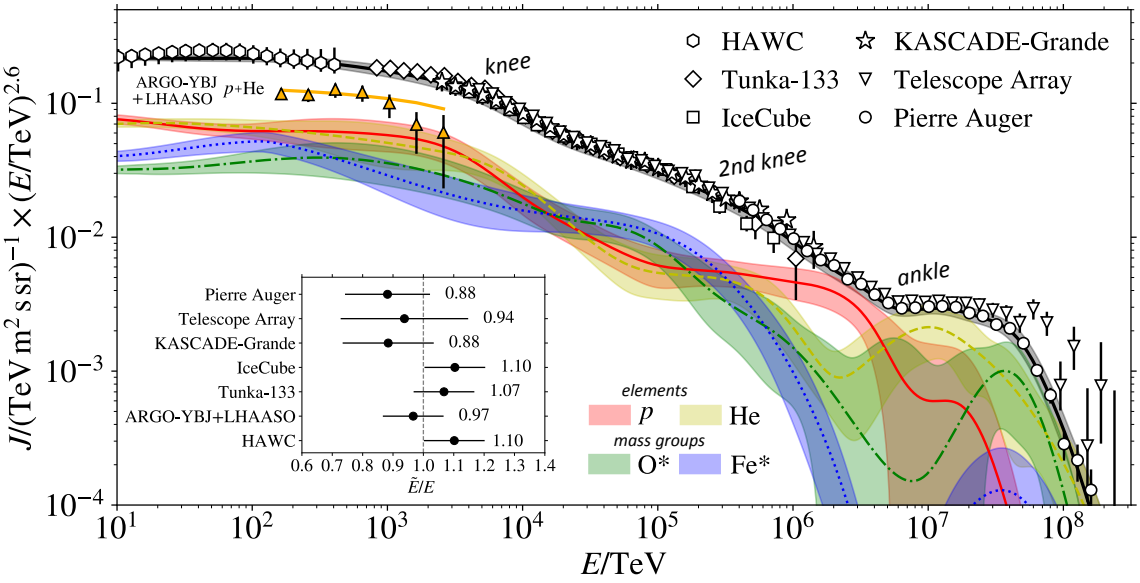

Figure 2.2: Cosmic-ray flux scaled with $E^{2.6}$ vs particle energy. Note that spectra from different experiments have been multiplied by a constant to adjust them to a common energy scale as described in [155] in more detail, where this figure is taken from.

these different regimes suggests an energy-related change in the origin of CRs. The ankle marks the transition from Galactic to extragalactic CRs [24]. Possible reasons for the knees include the acceleration by two different source types with different maximum rigidities [32] and the rigidity-dependent transport around CR sources [177]. In addition, the transport of CRs through turbulent magnetic fields not only changes their energy spectrum (see Section 2.3.2) and their escape times but is also responsible for their isotropization. The resulting CR highly-isotropic arrival directions complicate identifying CR acceleration sites. The observed weak large-scale an-isotropies can be modeled by accounting for the source distribution and the relative motion of the Earth. However, the observed small-scale an-isotropies may permit deductions about the local turbulent magnetic field (see [11] for a comprehensive review).

A vital role in the quest for finding the CR origin plays the discussion about

hadronic versus leptonic source models. Therefore, the generation of high-energy neutrinos is a clear sign for hadronic processes that require the existence of high-energy CRs in astrophysical sources or emission regions.

High-Energy Neutrinos High-energy neutrinos come equipped with their very unique set of physics. The small interaction cross section of neutrinos allows for deep insights into the central areas of astronomical particle accelerators. Relativistically accelerated CRs produce high-energy astrophysical neutrinos in interactions via different production channels with the proton, and photon target densities in accelerator sites [24]. Therefore, observations of high-energy neutrinos play an essential role in finding CR sources. Consequently, the diffuse high-energy neutrino flux of up to PeV high-energy neutrinos of astrophysical origin detected by IceCube [88] implies the existence of source classes that produce high-energy neutrinos via (photo-)hadronic interactions. The flux contains a significant extragalactic component [24]. Several potential associations of neutrinos with extragalactic objects have been identified with 3σ confidence, with the blazar TXS 0506+056 being the first one. This source lies well within the uncertainty region of the neutrino event reported by IceCube via the IceCube-170922A alert. *Fermi*-LAT observed a flaring state of this source during the IceCube detection and thus exhibits temporal and spatial correlation with a 3σ significance [89].

A 5σ detection of a high-energy neutrino source has not been announced yet by this generation's most sensitive neutrino detector, the IceCube observatory, nor by the ANTARES and Baikal neutrino telescopes.

Photons Observations of photons from astrophysical sources cover the entire electromagnetic spectrum with energies ranging from the radio regime $E = 10^{-6}\,\mathrm{eV}$ up to gamma rays above $E = 10^{14}\,\mathrm{eV}$. Photon energies are related to their frequency ν via

$$E = h\nu \approx 4.1 \frac{\nu}{10^{15}\,\mathrm{Hz}}\mathrm{eV}, \tag{2.2}$$

where h is the Planck constant.

Astronomy began with observing photons from the optical domain via the human eye. Since then, observations have been extended to the whole spectrum by ground- and space-based telescopes. This extension of observations to the complete electromagnetic spectrum is phrased as multi-wavelength astrophysics. The success of observing this messenger stems from the ease of tracing the straight-line trajectories back to their origin, which facilitates finding their sources. Thus, observations provide direct information about the sources, similar to neutrino observations. In contrast to neutrinos, photons can be detected much more easily, especially in the optical range. However, interactions and absorptions of photons in source regions and our atmosphere entail some disadvantages. For instance, X-rays require observation from satellite-based telescopes, and some source environments are utterly opaque to high-energy photons. Figure 2.3 gives an overview of the sensitivity of current and future

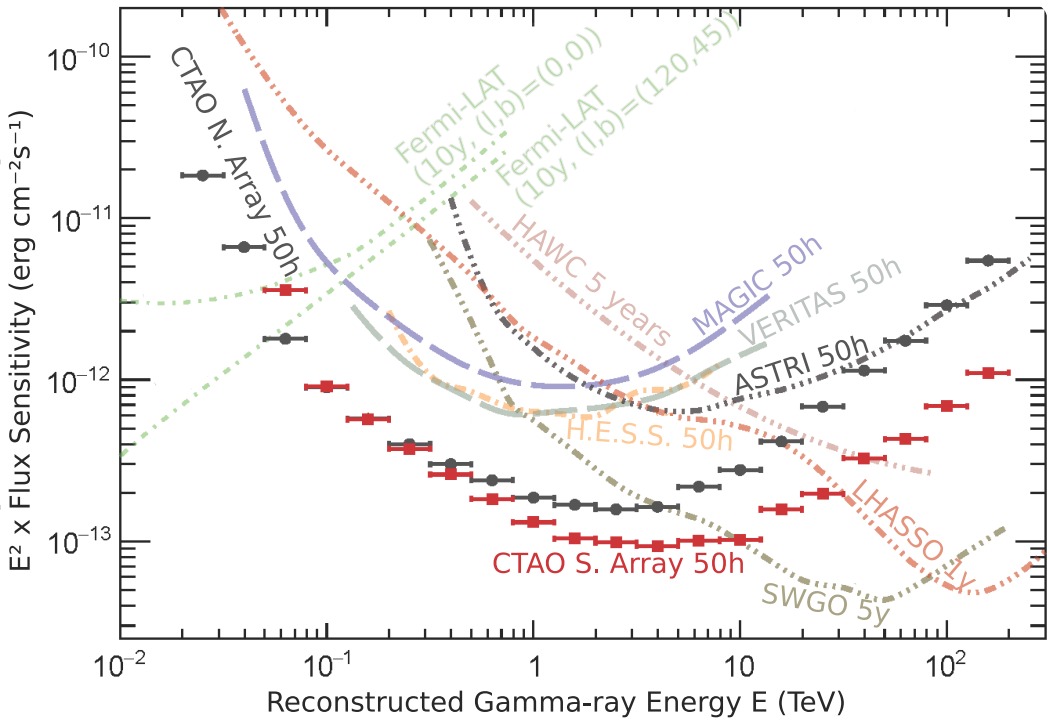

Figure 2.3: Comparison of the sensitivity of current and future GeV and TeV observatories. Figure slightly modified from [128].

GeV and TeV observatories, a range that is most relevant for the discussion in this thesis.

Gravitational Waves The existence of gravitational waves (GWs) follows as predictions from the general theory of relativity, as these space-time waves are a solution of the Einstein field equations

$$R_{\mu\nu} - \frac{1}{2} R\, g_{\mu\nu} + \Lambda\, g_{\mu\nu} = \frac{8\pi G}{c^4} T_{\mu\nu}, \tag{2.3}$$

where R and $R_{\mu\nu}$ denote the Ricci scalar and tensor, $g_{\mu\nu}$ the space-time metric, Λ the cosmological constant, and $T_{\mu\nu}$ labels the energy-momentum tensor. GWs are predicted and observed to originate from particularly massive, strongly accelerated objects, which include non-rotationally symmetric systems but also the merging or asymmetric collapse of massive objects, such as black holes or binary neutron stars. Interferometer-based GW observatories, such as LIGO and Virgo, have detected an increasing number of such events over the last years [3, 6, 7].

GWs allow for deep insights into sources as they cannot be absorbed by matter and pose an important constituent in the multi-messenger approach. These characteristics open up new promising opportunities in multi-messenger campaigns. However, large

uncertainties in the sky localization of current GW observatories impose challenges to the search for multi-messenger and electromagnetic counterparts and associated sources. Upcoming improvements of the Virgo and LIGO observatories will increase their sensitivity. Furthermore, the KAGRA interferometer in Japan and LIGO-India will join the global network [5] resulting in reduced localization uncertainties.

2.2 Transient Events

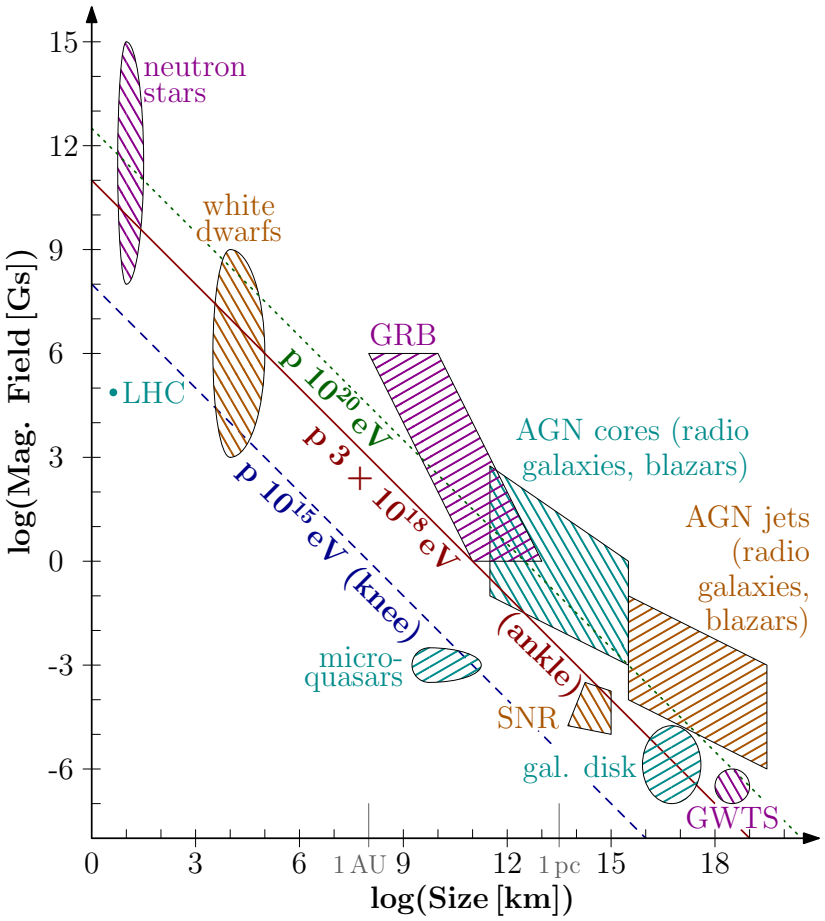

Figure 2.4: Hillas plot taken from [24].

The study of transient phenomena in the sky is a novel and rapidly increasing field of astronomy. Here, transient phenomena refer to astrophysical sources that show an unpredictable temporal evolution that exhibits a flaring character in emitted messengers caused by, e.g., explosions or mergers. Figure 2.4 shows a Hillas-plot that presents an overview of astrophysical source properties and their ability to accelerate CRs up to high energies. The maximum energies attainable in sources through acceleration are given by the Hillas criterion [84], which states that particles are confined until their

gyroradii $r_{\rm g}$ exceed the source size R

$$r_{\rm g} = \frac{E}{qcB} \lesssim R. \tag{2.4}$$

Source classes known for their transient character are introduced in the remaining part of this subsection.

Active Galactic Nuclei Galaxies with a black hole in the center that actively accretes matter and forms jets perpendicular to their accretion disk represent systems that can accelerate particles to extreme energies. These systems are called active galactic nuclei (AGN). Extreme conditions prevail in AGN jets because of strong magnetic fields, photon fields, and high mass densities. In relativistically accelerated plasmoids with high target densities and strong magnetic field strengths moving along the jet axis, secondaries are created through various mechanisms that include hadronic interaction processes [36, 86]. These moving plasmoids introduce variability of AGN jet emission on different timescales and frequencies [39, 77, 82, 100].

The subclass of AGN that points with one jet towards Earth is called a blazar. A blazar, TXS 0506+05, was the first extragalactic object from which a neutrino was detected during its flaring state with a temporal and spatial correlation with the significance of 3σ [89]. Figure 2.5 shows the broadband spectral energy distribution (SED) of TXS 0506+05 within a period of 14 days of the IceCube-170922A detection. This figure shows a typical blazar SED covering the electromagnetic spectrum with two characteristic bumps demanding advanced multi-wavelength and multi-messenger modeling with constraints from possible neutrino detections.

Gamma-Ray Bursts Gamma-ray bursts (GRBs) are powerful explosions that are primarily observed as short but very intense pulses of high-energy radiation in the sky. Subsequently, photons are emitted in the afterglow phase, posing an exciting object for multi-wavelength observations. There exist two general GRB subclasses that differ in their flare duration and result from different formation mechanisms. Whereas both flares occur on short timescales and thus must originate from relatively compact objects, the particularly short bursts last only a fraction of a second and are associated with mergers of binary neutron stars. The longer GRBs that last a few seconds up to minutes have been shown to originate from the collapse of a single massive star to form a black hole or a neutron star and were found connected to (superluminous) supernovae [185].

The list of open questions about GRBs is long. It contains aspects of their flare time evolution, the maximum energy reached, the progenitor's properties, the circumburst environment, and the dependencies of the jet opening angle. Rapid follow-up observations across the electromagnetic spectrum are needed to answer these questions. Combined multi-messenger observations that take GWs detections into account will

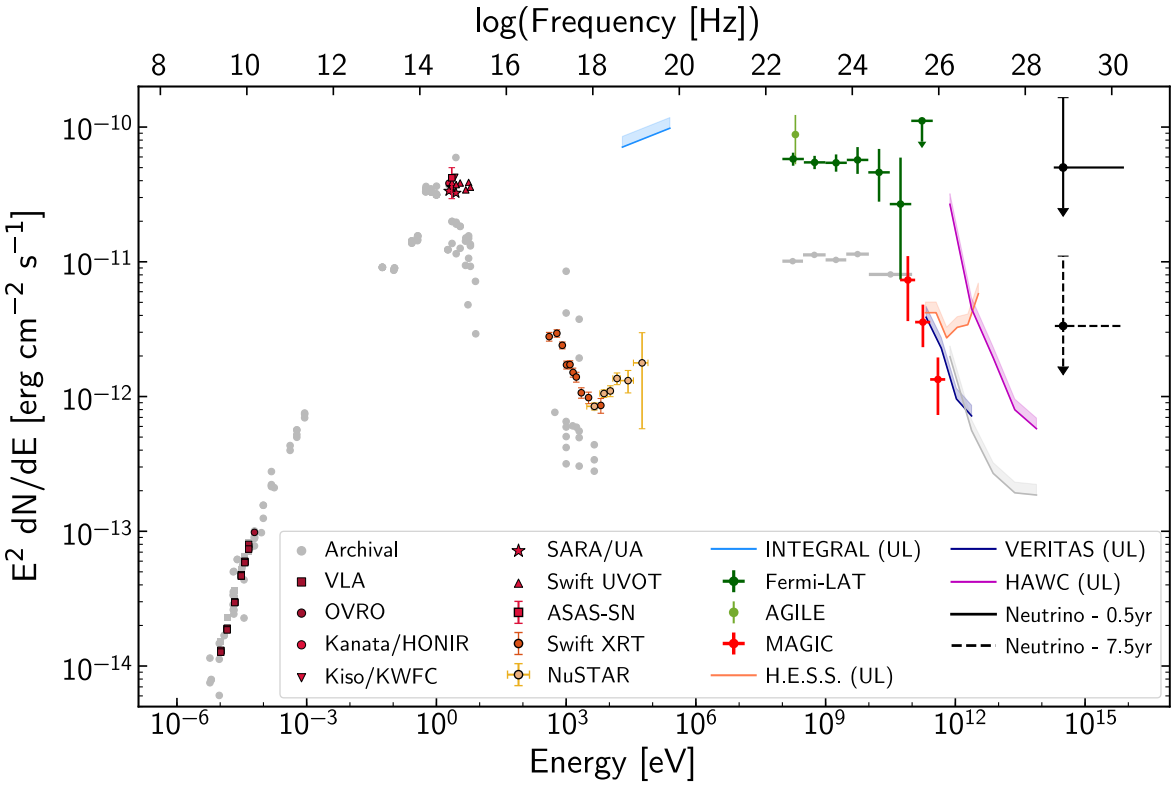

Figure 2.5: Broadband SED for the blazar TXS 0506+056 observed within 14 days of the detection of the IceCube-170922A event in comparison with archival data. Figure is taken from [89] while modifying font sizes.

shed further light on the nature of GRBs, especially when caused by binary neutron star mergers. Binary neutron star mergers cause both GRB and kilonovae [4].

GRBs also qualify as ideal objects for studying Lorentz invariance violations (LIV), as the tiny effects accumulate into potentially noticeable effects over the long source-to-earth trajectories. See an overview in the Appendix A of the study of LIV effects using a multi-messenger, real-time approach.

Fast-Radio Bursts Fast-radio bursts (FRBs) are very short-flaring radio transients caused by a not yet understood physical mechanism. The duration of the radio pulse typically ranges from microseconds to milliseconds. A first multi-wavelength insight was achieved by observing an FRB in coincidence with a short X-ray burst [116]. Because of the short burst durations, follow-up observations of the afterglows are crucial since direct observation of the burst is typically not possible outside of coordinated multi-wavelength campaigns. Figure 2.6 shows the number of FRB detections that are publicly distributed through the transient name server (TNS).

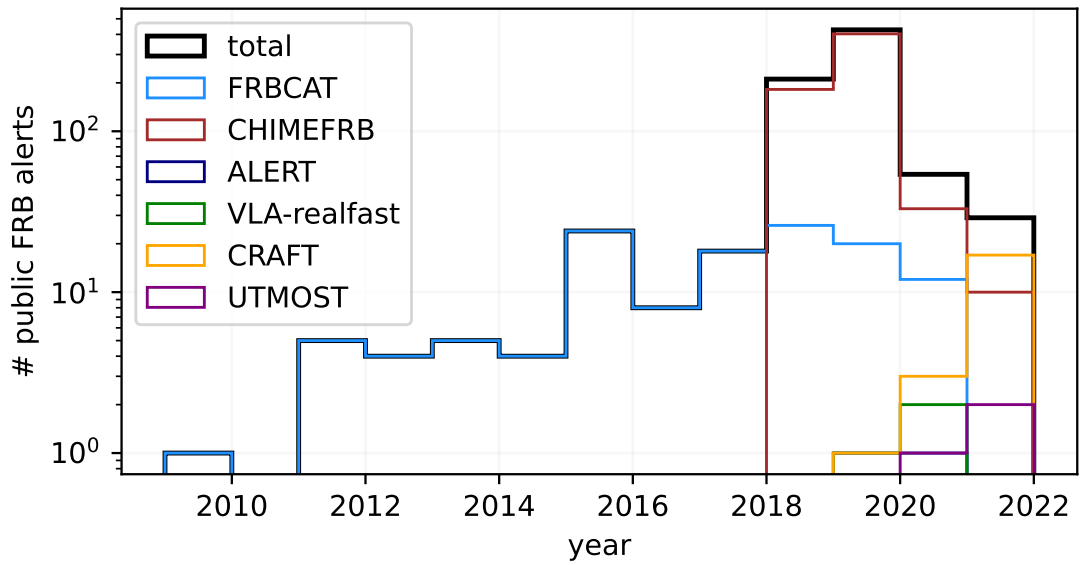

Figure 2.6: Statistic of publicly distributed FRB detections generated by evaluating data stored in TNS for different telescopes. Displayed data is taken from the TNS website. Note that the decrease since 2020 is caused by not all detections being distributed publicly anymore e.g. from CHIMEFRB.

Tidal Disruption Events A Tidal Disruption Event (TDE) is believed to originate from an orbiting star approaching its hosting supermassive black hole (SMBH) such that the gravitational forces disrupt the infalling star. These events are accompanied by long flares through the emission from the accretion of the stellar debris on the SMBH. TDEs are sometimes accompanied by jets. The possible association of neutrinos with TDEs [170] triggered renewed interest in this research direction in the context of a multi-messenger approach.

Flaring Stars Flares of stars are, by definition, events in which a sudden, substantial increase in the photon flux of an object occurs. These events have been observed and studied in the Sun for a long time. The knowledge gained from these investigations can largely be transferred to flares of other stellar objects under the assumption of similar underlying physical effects [129]. Furthermore, based on (semi-)empirical statistical relation properties of the flare can be deduced from observed quantities [28, 44, 132]. It is also assumed that during stellar flares of M dwarfs, high proton energies up to some GeV are possible – in extreme cases, even up to TeV [83, 129].

The study of these M-dwarf flares poses exciting insights into the propagation of CRs from M dwarfs to estimate the potential radiation load on Earth-like planets in their system. Thus, statements can be made as to how realistic it is to find life on these planets and whether the radiation intensity could prevent possible life.

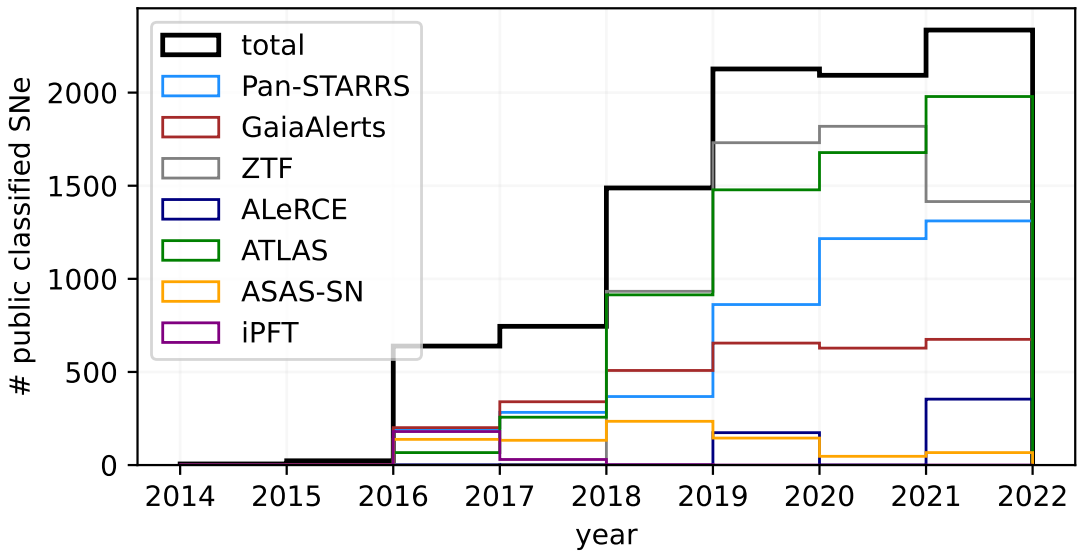

Figure 2.7: Statistic of publicly distributed and classified SN generated by evaluating data stored in TNS for different telescopes or brokers.

Novae A nova is a flare in a close binary system consisting of a white dwarf and its companion star. This transient event is caused by the accretion and heating of material from the companion star into the outer layer of the white dwarf. Exceeding a critical temperature leads to a sudden thermonuclear explosion. H.E.S.S. [78] and MAGIC [112] observed very-high-energy photons ($\gtrsim 100\,\mathrm{GeV}$) during the recurrent nova RS Ophiuchi outburst in 2021. Theoretic interpretation suggests the acceleration of charged particles to hundreds of GeV in the nova shock.

Supernovae Supernovae (SNe) are transient events caused by a powerful explosion of a star. Such an event can be triggered by stars in their final life cycle or in a binary system composed of a white dwarf and its companion star. The number of classified SNe increased due to improved observatories and more sophisticated analysis pipelines. Figure 2.7 presents the number of classified SNe as a function of time broken down to the observatories with the most classified detections.

2.3 Real-Time Effects

Due to prevailing particle densities and magnetic fields, there are various interaction and energy-loss processes of high-energy particles in transient astrophysical sources. Section 2.3.1 explains these processes in more detail and highlights their influence in the context of real-time multi-messenger astrophysics. Strong magnetic fields with turbulent components also introduce transport effects on charged particles that influence

their propagation and escape times, which in turn alter observable multi-messenger signatures. This is explained in Section 2.3.2.

2.3.1 Particle Interactions

The influence of particle interactions on the real-time effects of transient phenomena is complex. The challenge in multi-messenger astrophysics is to map the different messengers to the correct production mechanisms. A key aspect here is the temporal association of the signatures with the underlying physical processes. A related factor is the determination of the production regions of individual signatures. Due to the extended source regions, different processes may occur in other areas. One prominent example is the emission of blazars, where the resolution of the production regions along the jet is not possible through observations. Furthermore, there may be overlaps of different processes which are not spatially separable by observations.

The nonlinear interplay of different particle interaction processes adds to the complexity, especially in electromagnetic cascades. In addition to the primary particles, all secondary particles also interact while serving as target material for other processes.

Considering the example of broad-band fits on observed SEDs introduced in Section 2.1 shows the presence of numerous interaction processes from source regions. In blazars, for example, dominant leptonic processes are invoked in the literature to explain the observed SED [136, 148, 182]. Here, leptonic processes shape the first SED bump, the so-called synchrotron bump, through charged particles gyrating in the magnetic field. Whereas the whole modeling of the SED, particularly the time-dependent evolution during flares, is still subject to current research [25], the simultaneous observation of the flare in the electromagnetic spectrum with the neutrino observation is explainable by employing hadronic models. Note that the large proton and target photon density required to produce neutrinos through photo- and hadron-hadron interactions increase the $\gamma\gamma$ opacity [67, 79, 125]. A large $\gamma\gamma$ opacity introduces a reduced γ emission [100] resulting in a temporarily γ-suppressed jet. Figure 2.8 presents a schematic overview of the different interaction processes involved in creating γ-transparent and γ-suppressed jet states.

2.3.2 Particle Transport

CR transport is mostly investigated by means of the phase-space distribution function $n = n(t, \vec{r}, \vec{p})$ of CRs (see [24] for a review) at a given position $\vec{r}$, momentum $\vec{p}$, and time t. The relevant property-changing effects on n of relativistic charged particles appear on shorter timescales than those on which magnetic fields change. Therefore, magnetic fields are set to be stationary [61, 92]. This ansatz with predefined, stationary magnetic fields simplifies studies in various astrophysical environments. Therefore, the method pursued here corresponds to the test-particle approach since the feedback of particles on the environment is neglected.

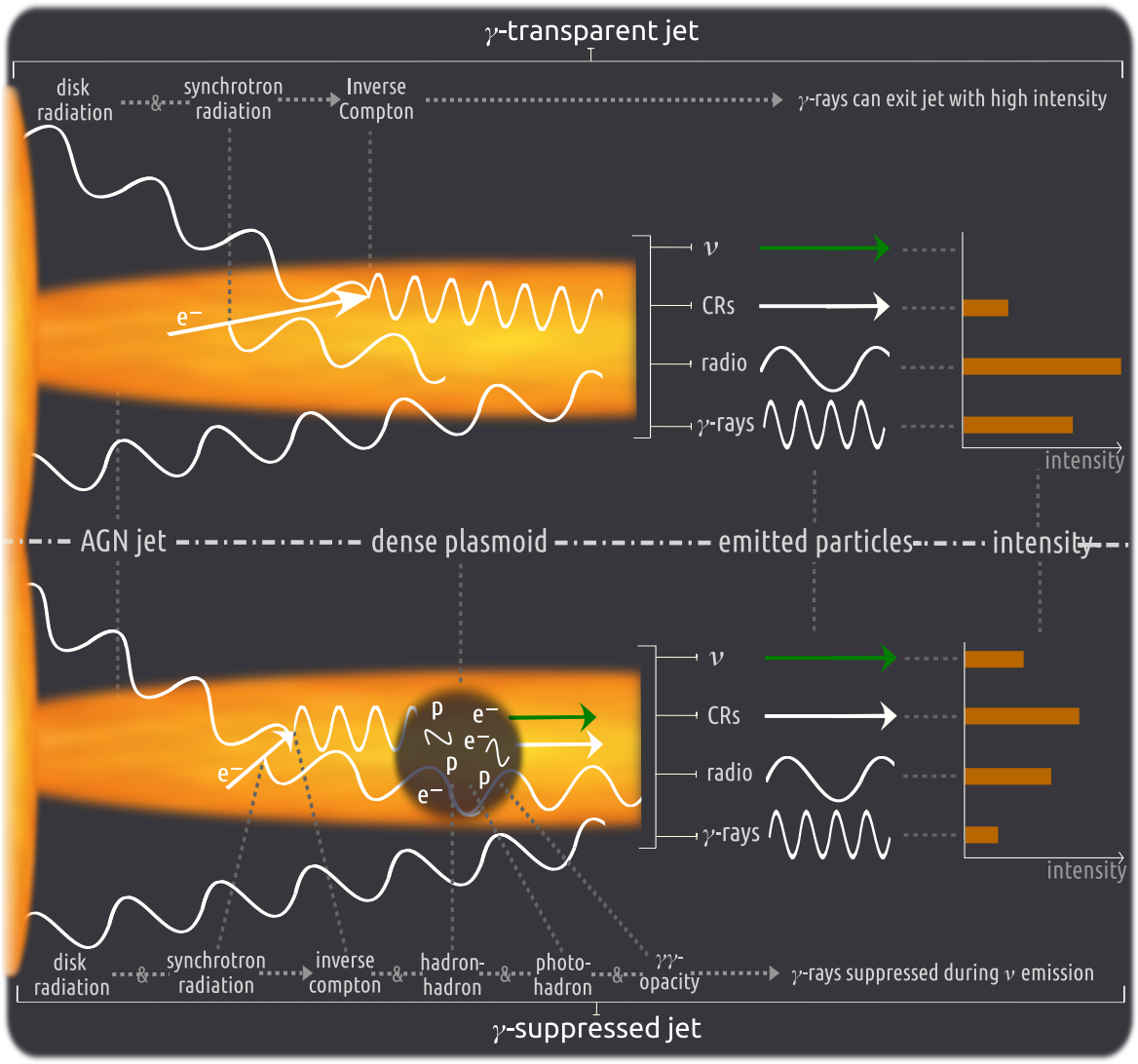

Figure 2.8: Schematic overview of the different interaction processes for γ-transparent and γ-suppressed jets. For example, large proton and photon target densities in the plasmoid in the γ-suppressed jet state shown in the lower panel increase the $\gamma\gamma$ opacity and temporarily reduce the γ-ray flux. On the other hand, the jet is transparent for γ-rays without the large proton and photon target densities. For this γ-transparent jet state, the neutrino production is assumed to be suppressed due to missing hadronic interactions, as illustrated in the upper panel.

Transport Equation The Parker-transport equation commonly describes the dynamics of the particle distribution function n of CRs in magnetic fields with near-isotropy in momentum space (e.g. [24, 57, 101, 188])

$$\frac{\partial n}{\partial t} = \underbrace{\nabla \cdot (\hat{\kappa} \nabla n)}_{\text{Spatial diffusion}} - \underbrace{\vec{u} \cdot \nabla n}_{\text{Advection}} + \underbrace{\frac{1}{p^2} \frac{\partial}{\partial p} \left(p^2 \kappa_{pp} \frac{\partial n}{\partial p} \right)}_{\text{Momentum diffusion}} + \underbrace{\frac{p}{3} (\nabla \cdot \vec{u}) \frac{\partial n}{\partial p}}_{\text{Ad. energy changes}} + \underbrace{S}_{\text{Source}} . \tag{2.5}$$

Here, κ_{pp} is the momentum diffusion scalar, $\vec{u}$ is an advection speed, p is the momentum, and $\hat{\kappa}$ is the spatial diffusion tensor. Note that interaction losses and drifts (see [186] for a discussion about the influence of drifts in the Galaxy) are neglected in this description governed by Equation (2.5) and that isotropy in momentum space is assumed. Thus only the magnitude of p appears, and only the diagonal elements of the spatial diffusion tensor $\hat{\kappa}$ are considered.

The physical processes involved in the Parker-transport equation are discussed shortly below, focusing on their real-time influence on observables.

- **Spatial diffusion**: The influence of spatial diffusion is dominant in many astrophysical systems. Neglecting all other terms of the Parker-transport equation yields the diffusion equation

$$\frac{\partial n}{\partial t} = \nabla \cdot (\hat{\kappa} \nabla n). \tag{2.6}$$

  The general solution of the diffusion equation for point sources at position x_i and an initial flare at t_0 governed by the initial condition $n(x, t = t_0) = \delta(x - x_i)$ yields a Gaussian distribution

$$n(x_i, t) = \frac{1}{2\sqrt{\pi \kappa_{ii}}} \exp\left(-\frac{x_i^2}{4 \kappa_{ii} t} \right), \tag{2.7}$$

  where i indicates the three spatial directions. The diffusion coefficients κ_{ii} are the diagonal elements of the diffusion tensor and are considered to be constant here. Computation of the second moment provides the definition of spatial diffusion

$$\left\langle (\Delta x_i)^2 \right\rangle = \int_{-\infty}^{+\infty} \mathrm{d}x_i \, x_i^2 n(x_i, t) = 2t \, \kappa_{ii}, \tag{2.8}$$

  with the running diffusion coefficient

$$\kappa_{ii} = \frac{\left\langle (\Delta x_i)^2 \right\rangle}{2t}. \tag{2.9}$$

  These equations illustrate the influence of diffusion effects on the temporal evo-

lution of charged particles in turbulent magnetic fields for a given diffusion coefficient. Furthermore, the variation of system parameters in source environments, such as radially decreasing magnetic field strengths, change the diffusion coefficients $\kappa_{ii}(B, E)$ and thus introduce complex time- and space-dependent dynamics of particle transport that is not governed anymore by the simple solution given in Equation (2.7) for constant diffusion coefficients. Therefore, the influence of diffusion has profound effects on the residence time of CRs in source regions with high particle and photon target densities and thus significantly influences the intensity and variability of the secondaries produced in particle interaction cascades.

- **Spatial advection**: This effect often describes a galactic wind, where charged particles stream with a certain velocity represented by the term $\vec{u} \cdot \nabla n$. Similar to diffusion, but much easier to model, advection eventually also modifies the escape times in sources [25].

- **Momentum diffusion**: Diffusive change in momentum is also governed by a Markov process

$$\frac{1}{p^2}\frac{\partial}{\partial p}\left(p^2 \kappa_{pp} \frac{\partial n}{\partial p}\right). \tag{2.10}$$

  Here, isotropy in momentum space is assumed. This term is relevant for diffusive reacceleration models such as the second-order Fermi acceleration that is caused by moving magnetic irregularities [131].

- **Adiabatic energy changes**: Energy changes due to compressive flows are governed by the term

$$\frac{p}{3}(\nabla \cdot \vec{u})\frac{\partial n}{\partial p}. \tag{2.11}$$

  This term models, for example, the first-order Fermi acceleration.

- **Source**: Sources and sinks of CRs modeled via the transport equation are taken into account by a dedicated term S of the transport equation. This term describes the source spectrum that contains the physics of the acceleration problem.

The Parker-transport equation can be extended by taking continuous and catastrophic energy loss or gain processes into account (see e.g. [24]). Furthermore, the spatial diffusion can be modified by including a term

$$\tau \frac{\partial^2 n}{\partial t^2} \tag{2.12}$$

to take the timescale τ into account on which the transport becomes diffusive. This extension allows for the description of the initial ballistic transport phase, which shall be explained in more detail in Section 3.2.2. In this thesis, the transport is called diffusive[1] when the diffusion coefficient remains constant, i.e., has reached its steady-state value.

Leaky-Box Model The leaky-box model provides a simplified description of the transport of CRs in a closed, box-like system with escaping particles (leak out) from it. This model is applied in the description of the transport in galaxies but can also be used in comparable systems that are subject to the following conditions:

1. The physical system is considered to be in steady-state,

$$\frac{\partial n}{\partial t} = 0. \tag{2.13}$$

2. Spatial diffusion of CRs is described solely through their escape times τ_{esc} from the system via

$$\nabla \cdot (\hat{\kappa} \nabla n) = -\frac{n}{\tau_{\mathrm{esc}}}. \tag{2.14}$$

The resulting steady-state transport equation for the leaky-box model yields

$$n(E) = \tau_{\mathrm{esc}}(E) \cdot S(E), \tag{2.15}$$

where these quantities depend on the particle energies. Note that other terms of the Parker-transport equation could be considered by additional timescales such as τ_{adv} or τ_{cool} that describe advection and energy-loss processes, respectively.

Escape times for a diffusion-dominated system with space-invariant properties, such as constant magnetic fields, can be expressed via the average escape distances $\langle d \rangle$ and their energy-dependent scalar diffusion coefficients $\kappa(E)$ via

$$\tau_{\mathrm{esc}} = \frac{\langle d^2 \rangle}{\kappa(E)}. \tag{2.16}$$

Geometric considerations simplify Equation (2.16) to the extent that $\langle d^2 \rangle$ can be replaced by system-specific quantities. For spiral galaxies, particles originated in the galactic planes escape mostly perpendicularly to it after reaching the scale heights H

[1]Note that particle propagation in general turbulence, instead of the applied isotropic Kolmogorov model, may also be subdiffusive or superdiffusive, for which the running diffusion coefficients decrease or increase, respectively.

so that $\langle d^2 \rangle \approx H^2$ results in

$$n(E) = \frac{H^2}{\kappa(E)} \cdot S(E). \tag{2.17}$$

In nearly spherically symmetric systems with central sources and average escape distances of R, Equation (2.17) yields

$$n(E) = \frac{R^2}{\kappa(E)} \cdot S(E). \tag{2.18}$$

The assumption of source spectra following a power-law $S(E) \propto E^{-\alpha}$ in accordance with observations and state of the art acceleration mechanisms leads to profound conclusions concerning the particle spectrum in the leaky box

$$n(E) \propto (\kappa(E))^{-1} \cdot S(E) \propto E^{-\delta-\alpha}. \tag{2.19}$$

Here, a power-law dependency of the diffusion coefficient on the energy, $\kappa(E) \propto E^{\delta}$, is assumed following analytical theories and numerical simulations (see [69] and references therein).

2.3.3 Time Delays of Messengers at Arrival at Earth

For most extragalactic sources, the source-to-Galaxy propagation time $\tau_{\mathrm{s-MW}}$ dominates the required total propagation time $\tau_{\mathrm{tot}} = \tau_{\mathrm{esc}} + \tau_{\mathrm{s-MW}} + \tau_{\mathrm{MW}} \approx \tau_{\mathrm{s-MW}}$. Here, τ_{esc} denotes the escape time in the source and τ_{MW} the residence time in the Milky Way before reaching Earth. The time $\tau_{\mathrm{s-MW}}$ mainly depends on two aspects:

1. **Particle speeds**: The time needed to cover the distance between the source and the Galaxy depends largely on the particle speed.

2. **Trajectory length**: For rectilinear paths, the trajectory lengths correspond to the distance between the source and the Galaxy. For charged particles, deflections in the magnetic field play an important role and increase the mean trajectory lengths to values that can significantly exceed the distance.

Several effects influence these two quantities:

Relativistic Doppler Effect

The relative motion between the source and the Earth introduces time delays that can be described by the relativistic Doppler effect. This effect can be visualized by employing worldlines in 4D space-time. For simplicity and without the restriction of generality, the 3D space can be reduced into one dimension by considering only the distance between both objects as the relevant contribution in space. Figure 2.9 shows

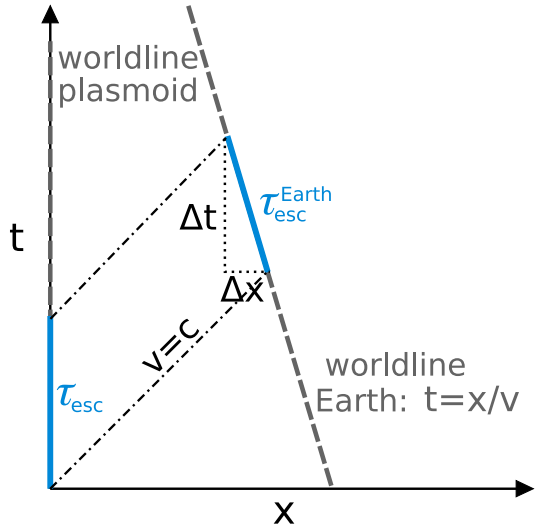

Figure 2.9: Space-time diagram of a blazar in which the plasmoid that moves relativistically along the jet axis is chosen as the reference system. Therefore, the worldline of the plasmoid follows along the y-axis. The worldline of Earth is defined as $t = x/v$, where v denotes the relative speed between the plasmoid and Earth. Diagonal lines represent the worldlines of photons.

a space-time diagram of a blazar in which the plasmoid that moves relativistically along the jet axis is chosen as the reference system. The Earth moves relative to the plasmoid with speed v on the worldline $t = x/v + t_0$, with t_0 being an offset. During the escape process, the Earth moves $\Delta x = v\Delta t$ relative to the plasmoid. With the time needed for light to pass the distance $\Delta x = c\,(\Delta t - \tau_{\rm esc})$ follows for the time Δt passed on Earth within the inertial system at the plasmoid $\Delta t = c\tau_{\rm esc}/(c - v)$. Applying the effect of time dilation yields for the escape time observed from Earth:

$$\tau_{\rm esc}^{\rm Earth} \;=\; \Delta t \left(1 - \frac{v^2}{c^2}\right)^{1/2} \;=\; \tau_{\rm esc} \left(\frac{1 + v/c}{1 - v/c}\right)^{1/2}, \tag{2.20}$$

Consequently, this factor depends only on the relative speed between the source (here, AGN jet plasmoid) and Earth and reduces the duration of the observable flare on Earth when the plasmoids are moving towards Earth $v < 0$.

Mass-Related Effect

Massless messenger travel with the speed of light c. Highly relativistic particles with energy E and non-vanishing, invariant mass m_0 travel with slightly-reduced speeds

$$v = c \cdot \sqrt{1 - \frac{1}{\gamma^2}} = c \cdot \sqrt{1 - \frac{m_0^2 c^4}{E^2}} \overset{E \gg m_0^2 c}{\approx} c - \frac{m_0^2 c^5}{2E^2}, \tag{2.21}$$

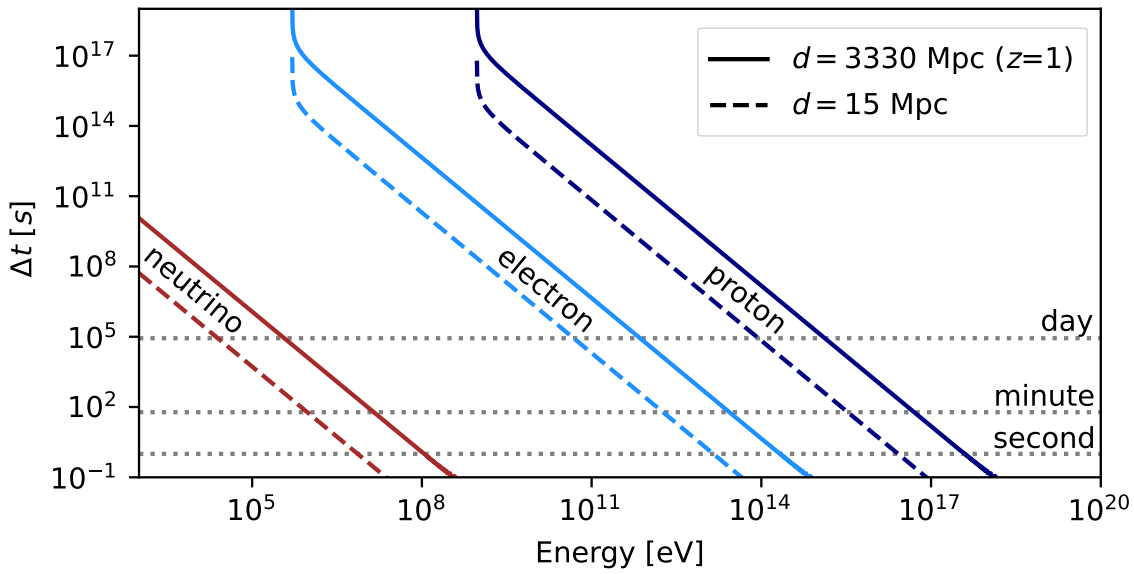

Figure 2.10: Time delay Δt of messengers with different invariant masses for different trajectory lengths according to Equation (2.22). The time delay is defined with respect to the time photons need for trajectory lengths of $d = 15\,\text{Mpc}$ and $d = 3330\,\text{Mpc}$, respectively.

where γ denotes the Lorentz factor. In the last step, the Taylor expansion around $m_0^2 c/E = 0$ is applied. The deviations from c for high-energy particles are minor, especially for neutrinos with tiny masses $m_\nu < 0.8\,\text{eV/c}^2$ (90% CL) [95]. Figure 2.10 shows the time delay Δt accumulated at different travel distances d as a function of energy that is determined with respect to the speed of light

$$\Delta t = \frac{d}{c} - \frac{d}{v} = \frac{d}{c}\left(\frac{c}{v} - 1\right) \overset{E \gg m_0^2 c}{\approx} \frac{d m_0^2 c^3}{2E^2}\,. \tag{2.22}$$

The E^{-2} scaling is visible in Figure 2.10. For particle energies close to the rest energies, this scaling breaks down.

Deflections in Magnetic Field

For the rectilinear trajectories of neutrinos, the trajectory length is equal to the distance from the source to the observer. On the other hand, charged particles deviate from rectilinear trajectories due to deflections caused by the magnetic fields. How much the trajectories are increased on average by this effect shall be investigated in more detail in the following paragraph.

When CRs propagate ballistically, they move approximately rectilinearly. The other uncharged messengers, e.g., GWs, photons, and neutrinos, move also rectilinearly. In these cases, the propagation time is approximately $\tau_{\text{tot}} \approx \tau_{\text{s-MW}} \approx d/v$, where d

denotes the distance between source and Galaxy and v the speed of the particle. The temporal variation in the particles arriving at Earth is largely dictated by the temporal evolution of the flare, as discussed in Chapter 4 and by the other effects discussed in the present chapter.

In contrast, for diffusively propagating charged CRs, the transport phase from the source to the Galaxy determines the arrival times at Earth. The time particles need to travel from sources to Earth yields

$$\tau_{\mathrm{tot}} = \tau_{\mathrm{esc}}^{\mathrm{Earth}} + \tau_{\mathrm{s-MW}} + \tau_{\mathrm{MW}} \,. \tag{2.23}$$

The individual timescales yield

$$\tau_i \approx \begin{cases} d_i^2/(2\kappa_i) & \text{diffusive} \\ d_i/v & \text{ballistic} \end{cases} \,, \tag{2.24}$$

where d_i and κ_i denote the distances and diffusion coefficients that apply in each environment along the particle trajectory, respectively.

Implications for Follow-Up Observations

The effects discussed before affect the observable signatures in different ways. The following list describes the influence of the above effects on the required time from the origin to the observation on Earth. Furthermore, the relevance and the impact on transient events' characteristics and observable multi-messenger signatures are pointed out.

Photons The escape time of photons from sources depends on the optical depth and the distance to be covered. Neither mass-related nor transport-related effects play a role. However, the escape of photons within the plasmoid that moves relative to Earth is subject to the relativistic Doppler effect. Therefore, the relativistic Doppler effect modifies the flare duration observed on Earth.

Neutrinos Whereas no transport-related effects occur, the non-vanishing mass modifies the propagation time required on the rectilinear path between the source and Earth. Relativistic Doppler effects are an additional factor. However, these effects are negligible for current neutrino observations. Therefore, the runtimes of neutrinos from sources towards Earth depend exclusively on the distance to be covered.

CRs In each transport phase, CRs can be affected by various effects. The dominant influence is caused by deflections in magnetic fields, especially if the transport can be described diffusively. The other effects are also present but can typically be neglected. Since CRs produce photons and neutrinos

through interactions in sources, the influences of CRs on secondaries are inherited. The dynamics of the CRs can therefore influence the shape of a light curve of photons and their spectrum during a flare.

GWs The GW from the binary neutron star merger GW170817 [3] arrived $\sim 1.7\,\mathrm{s}$ before the electromagnetic counterpart [4] was detected with *Fermi* GBM and INTEGRAL SPI-ACS. These observations are compatible with the assumption of propagation velocities of GWs at the speed of light [187].

Chapter 3

Real-Time Multi-Messenger Tools

The scope of this work outlined in Chapter 1 requires the use of tools that make advances in the observation of transients but also shed light on physical processes through numerical simulations. The development of Astro-COLIBRI has facilitated the time-consuming work of burst advocates and shift crews in H.E.S.S. and other observatories to evaluate transient events. The overview of the real-time multi-messenger ecosystem and Astro-COLIBRI as an overarching tool presented in Section 3.1 is based on the few-author publications where I have contributed as lead or co-author,

- **P. Reichherzer*** et al., "Astro-COLIBRI—The COincidence LIBrary for Real-time Inquiry for Multimessenger Astrophysics", *The Astrophysical Journal Supplements Series*, 256, 1, 2021 — doi: 10.3847/1538-4365/ac1517,

- H. Ashkar*, ..., **P. Reichherzer** et al., "The H.E.S.S. gravitational wave rapid follow-up program", *Journal of Cosmology and Astroparticle Physics*, 3, 2020 — doi:10.1088/1475-7516/2021/03/045,
  where I contributed with Astro-COLIBRI developements,

as well as on the proceedings [141, 156]. Section 3.2, where simulation tools in the context of real-time and multi-messenger aspects are discussed, is based on the following publications that are either in the peer-review process or in preparation

- R. Alves Batista, ..., **P. Reichherzer** et al., "CRPropa 3.2 — an advanced framework for high-energy particle propagation in extragalactic and galactic spaces", in preparation (2022),

- **P. Reichherzer*** and J. Becker Tjus, "PropPy — Correlated random walk propagation of cosmic rays in magnetic turbulence", *Journal of Open Source Software*, 7, 74, 2022 — doi:10.21105/joss.04243,

and the proceeding [17]. Table 3.1 gives an overview of my contribution statistics for the software discussed in this chapter.

Table 3.1: Contribution statistics for software tools during my Ph.D. thesis taken from GitHub and Gitlab on February 22, 2022.

Software	Contributed commits (all)	Merges (all)	Fixed issues (all)
Astro-COLIBRI	1448 (2770)	112 (240)	88 (243)
CRPropa3	148 (2418)	4 (129)	2 (231)
CRPropa3 notebooks	19 (102)	2 (10)	–
PropPy	770 (770)	29 (29)	32 (32)
FLRW tool	4 (85)	1 (2)	0 (6)

3.1 Transient Follow-Up Tools

The field of astrophysics is experiencing several fundamental changes, such as the increasing relevance of observations of transients, i.e., temporal variability of astronomical sources such as supernova explosions, fast radio bursts (FRBs), and gamma-ray bursts (GRBs). An increasing number of cosmic messengers provide crucial information about these events. The detection of a diffuse flux of high-energy neutrinos [1] and of gravitational waves from mergers of compact binaries [4] has started to supplement electromagnetic observations. Combining these complementary messengers can provide crucial insights into events in the transient sky. The advances in the multi-messenger and multi-wavelength approach are driven by new next-generation instruments dedicated to the study of the most violent phenomena in the Universe, as well as by improving real-time alert and follow-up systems. In real-time multi-messenger astronomy, to tackle the above-described rapid developments in observation mechanisms, among others, an ecosystem of numerous complimentary services has been established over the last decades. For a review of high-energy alerts in the multi-messenger era, see [55].

The study of these extreme flaring events in the multi-messenger approach requires real-time and, to a large extent, fully automated communication between telescopes (see e.g. [19, 120]) and researchers to respond instantaneously to events with follow-up observations to better understand the nature of these events through complementary observational data. This information exchange uses different data formats, e.g., those proposed by the International Virtual Observatory Alliance, and different communication channels for the dissemination of alerts. The Astro-COLIBRI tool acts as a central platform that bundles and evaluates alerts from the various channels and further automates the coordination of follow-up observations by providing and linking detailed information through its graphical interface that is easily comprehensible for humans. While the need for specialized tools hosted on various websites for certain messengers is evident, users should not be expected to have familiarized themselves with all of them in order to carry out meaningful multi-messenger astronomy. Astro-COLIBRI supports users by providing links to webpages without the user having to navigate through the ecosystem and manually search for the event each time.

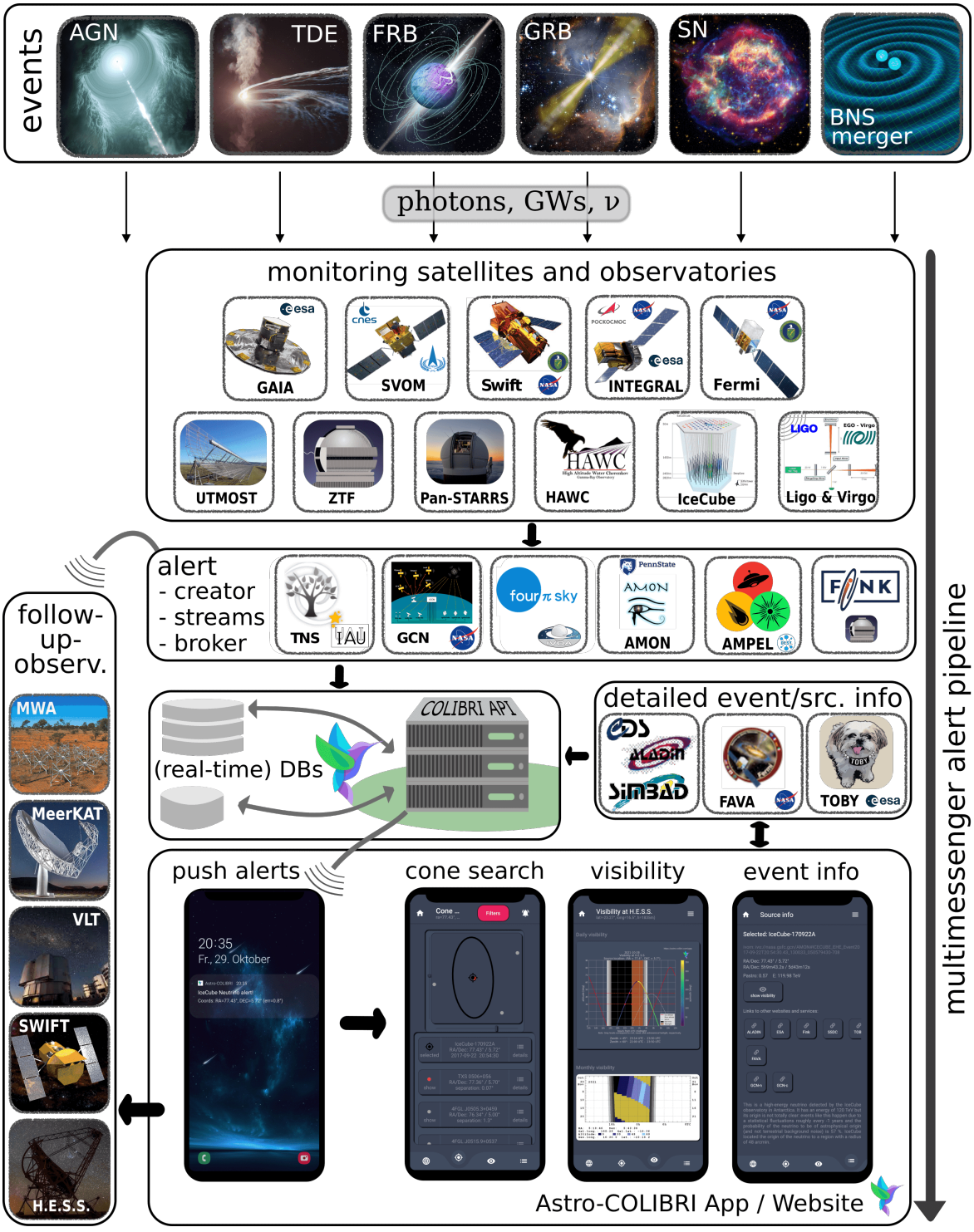

Figure 3.1: The multi-messenger pipeline from observations of transient events to the user notification and its visualization in the Astro-COLIBRI app. Details of the Astro-COLIBRI architecture are shown in Figure 3.5. Overview over alert creator, broker and streams is given in Table 3.2. Services with event information are listed in Table 3.3.

The overall workflow of transient events in the context of the real-time multi-messenger approach outlined here is summarized in Figure 3.1. When a flare is observed by a monitoring satellite or observatory, one or more alerts are sent to the community via brokers. Tools that correlate sub-threshold signals from different observations or do other detailed offline analyses complement the alert streams. An overview of alert creators, brokers, and streams is presented in Section 3.1.1. These alerts may directly trigger observatories for follow-up observations.

An ecosystem of services that provide additional information on transient events is introduced in Section 3.1.2.

Section 3.1.3 introduces Astro-COLIBRI as a holistic system with a user-friendly graphical web interface that acts as a top layer of the specific service providers presented in Section 3.1.2 as well as information and alert streams discussed in Section 3.1.1.

Section 3.1.4 presents possible automated follow-up pipelines but also outlines processes that include an Astro-COLIBRI-based discussion until a manual follow-up observation can be approved. Here, the planning of follow-up observing campaigns with Astro-COLIBRI in observatories is presented using the AGN Target of Opportunity (ToO) program in the High Energy Stereoscopic System (H.E.S.S.) as a representative example. This section employs ideas presented in

- **P. Reichherzer*** et al., "Astro-COLIBRI—The COincidence LIBrary for Real-time Inquiry for Multimessenger Astrophysics", *The Astrophysical Journal Supplements Series*, 256, 1, 2021 — doi: 10.3847/1538-4365/ac1517.

Lastly, the detection of the most distant very-high-energy AGN is presented, which I conducted as principal investigator and task-force leader. Here, Astro-COLIBRI has facilitated the coordination.

3.1.1 Alert Systems, Streams & Brokers

The fundamental pillar of real-time multi-messenger astronomy is the monitoring of satellites and observatories. These observatories cover the entire spectrum of detectable messengers and continuously scan large parts of the sky. In the case of detection in the real-time analysis that meets telescope-, event-type-, and messenger-specific criteria, further offline analyses are triggered, and alerts with basic event information may be sent to the community to initiate rapid follow-up observations.

Table 3.2: Overview over various alert creator, broker and streams. Astro-COLIBRI listens to VOEvent alerts via various brokers, parses notifications from FlaapLUC alert mails and notices from GCN, as well as from new confirmed SNs from various alert brokers distributed via TNS.

Service	Description
AMON [165]	Real-time system searching through streams of sub-threshold events from several multi-messenger facilities for correlations of spatial and temporal coincidences.
AMPEL [127]	Alert management, photometry, and evaluation of light curves (AMPEL) system. AMPEL combines the functionality of an alert broker with a generic framework to host user-contributed analysis scripts.
ATel [150]	Astronomer's Telegrams (ATels) are human-written, web-based notifications to report and comment on new astronomical observations of transient sources.
FINK [123]	Broker for automatized ingestion, annotation, selection, and redistribution of transient alerts that provides real-time transient classification that is continuously improved by using deep learning and adaptive learning techniques.
FlaapLUC [102]	Detects relative flux variations in *Fermi*-LAT data of sources and alerts users via emails. Based on the Science Tools provided by the *Fermi* Science Support Center and the *Fermi*-LAT collaboration.
Four π sky [168]	Decentralized and open infrastructure of open data-services based on the VOEvent standardized message-format for distributing transient alerts, such as a VOEvent broker and a DB that stores historical transient alerts.
GCN-Circulars [22]	The GRB Coordinates Network (GCN) distributes human-written reports (named Circulars) about follow-up observations of GRBs. Figure 3.3 shows the number of GCN Circulars distributed in each year.
GCN-Notices [22]	Machine-generated alerts about GRBs intended to trigger rapid follow-up campaigns.
TNS[1]	The Transient Name Server (TNS) is the official International Astronomical Union mechanism for reporting new SN candidates and naming spectroscopically confirmed ones. Brokers e.g. such as those listed in the row named *ZTF/LSST broker* distribute alerts via TNS.
VOEvents [134]	In order to use a standardized, machine-readable format, VOEvents were officially adopted to report observations of transients in 2006 by the International Virtual Observatory Alliance.
ZTF/LSST broker	There are dedicated brokers developed to handle large-scale astronomical survey data from ZTF and LSST. Besides AMPEL and FINK, there exist the brokers ANTARES [152], ALeRCE [62], Fritz[2], Lasair [164], MARS[3], and Pitt-Google Broker[4].

In real-time multi-messenger astronomy, alerts of transients and the assessment of their relevance for follow-up observations to the respective observatories are of fun-

[1] `https://www.wis-tns.org/`

[2] `https://github.com/fritz-marshal/fritz`

[3] `https://mars.lco.global/`

[4] `https://pitt-broker.readthedocs.io/en/latest/`

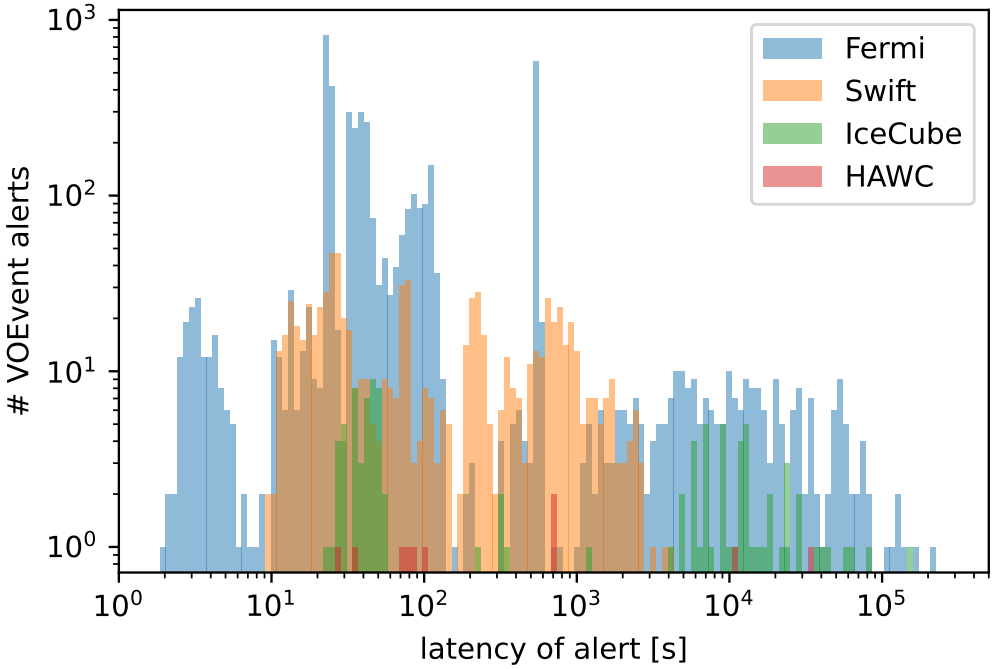

Figure 3.2: Latency of the distribution of VOEvents from different observatories during the window between 2018/01/01 and 2021/06/22. VOEvents from *Fermi* GBM, Swift BAT, Swift XRT, and VOEvents from the HAWC burst monitor are presented. All VOEvents whose ivorn contain *amon/icecube*, *ICECUBE_GOLD*, *ICECUBE_BRONZE*, *ICECUBE_Cascade_Event*, or *NU_EM_Event* are summarized in IceCube. Taken from Reichherzer et al. (2021, [143]).

damental importance. There are several channels for notifications on different platforms and different timescales. Various alert systems summarized in Table 3.2 include VOEvents, GCNs (notices and circulars), TNS notifications, and The Astronomer's Telegram (ATel), which differ in their degree of machine or human-generated content in the underlying communication technology, and the targeted scientific community. The technologies involve the usage of databases, webpages, emails, and brokers and require the community to make an effort to keep track of the ever-increasing amount of relevant information.

Figure 3.2 shows the latency of VOEvent alerts for several monitoring observatories. Note that an observatory may distribute multiple alerts for an event with varying stages in the processing, ranging from preliminary event information within the first few seconds to several minutes, hours, or even days for final analysis results. Some outliers are not shown in the figure, which are beyond the time window shown, and are caused by humans-in-the-loop due to errors of the otherwise automated analysis pipelines.

The formation of bumps in the histogram can be explained by using the Fermi

Gamma-ray Burst Monitor (GBM) as an example. *Fermi* GBM has been scanning the sky for GRBs for more than a decade. During this time, around 3000 GRBs were observed by the satellite. Each detection triggers a standard routine, where several automated or human-written messages and alerts are sent to the community. The first four steps are now fully automated (see [180] and references therein for details) with improved localization information in each iteration:

1. **GBM alert** *(automatic)*: First alert of transient with information about trigger time, and trigger significance. These alerts are not shown in Figure 3.2 because no information is included about the time of observation, and no latency can be calculated.

2. **GBM flight position** *(automatic)*: Onboard calculated localization. These rapid alerts have latencies of a few seconds and are represented by the first bump in Figure 3.2 at a few seconds. *Fermi* occasionally sends several updates of this analysis, each of which has a latency of a few tens of seconds. These alerts contribute to the extended bump in Figure 3.2 that ranges from ten seconds up to a minute.

3. **GBM ground position** *(automatic)*: Intermediate ground-based computed localization. Slightly more delayed than the flight position alerts, with a latency ranging from a few tens of seconds to a few minutes, with most arriving with a latency of a minute. There may be several ground position alerts for one event.

4. **GBM final position** *(automatic)*: Final localization and additional event information. Since early 2016, these alerts are generated based on the automated localization algorithm RoboBA [73]. The latency of RoboBA-related alerts is around 10 minutes and results in the peak in Figure 3.2 at this time. Before 2016 and afterward, in case of errors in the automatic RoboBA routine ($\lesssim 20\%$ of cases), a human-in-the-loop generated final localization is used for the alert. These alerts have larger latencies and scatter over several orders in the shown latency times in Figure 3.2.

5. **GBM GCN circulars** *(human-generated)*: Reports of follow-up observations made by the observers that also contain the assigned name of the event. The number of GCN circulars is shown in Figure 3.3. *Fermi* GCNs make up only a small fraction, as most GCNs report follow-up observations at other wavelengths from ground-based observatories around the globe that were triggered by *Fermi*, Swift, or INTEGRAL alerts in the first place.

As a consequence of the outlined procedure, the largest variations in latencies are caused by sending alerts according to differently elaborated algorithms at different stages of the complete analysis pipeline and by interventions by humans caused by errors in automated processes.

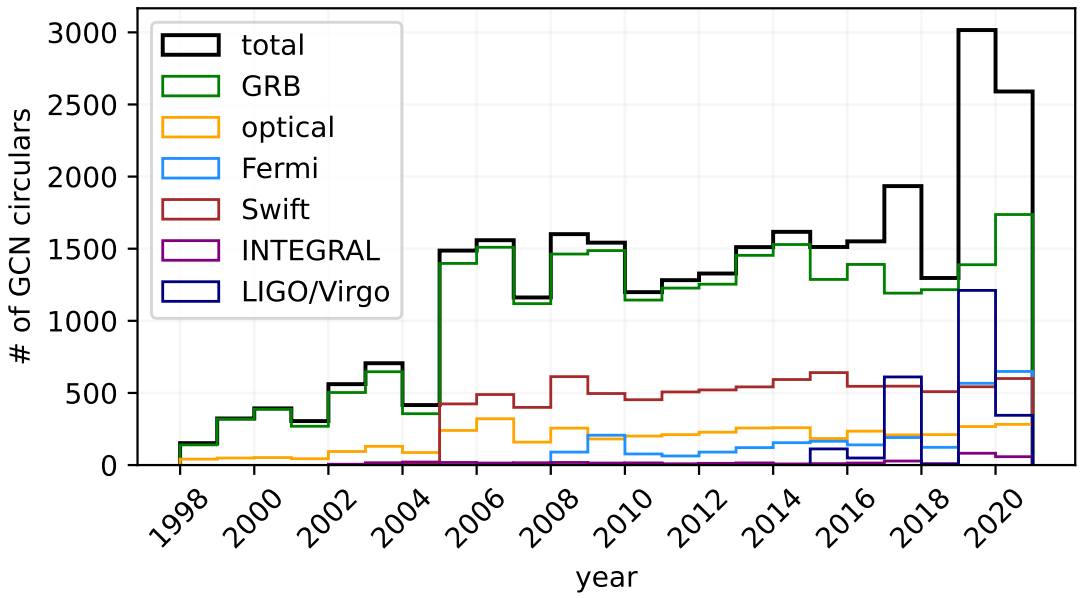

Figure 3.3: The number of GCNs circulars has steadily increased over the last years. A strong increase was due to the addition of GW observations as another messenger.

The median latencies of all alerts per quarter since 2014 for the final GRB VO-Events of INTEGRAL, *Fermi* GBM, Swift BAT, and XRT are shown in Figure 3.4. Note that the latencies caused by outliers are irrelevant, as can be seen by the constant latency of GMB alerts through the use of RoboBA after 2016. Swift latencies are also constant with different values for BAT and XRT. In the case of final offline INTEGRAL alerts, there is more variability caused by the low statistics of overall only 51 alerts, each of which is generated manually after interactive data analysis performed by a duty scientist.

3.1.2 Detailed Event Info

The large number of types of different transients, messengers, and observing telescopes has in the last decades created an ecosystem of different services that provide specific information on various aspects relevant to real-time multi-messenger astrophysics. Both the nature of the information and its distribution varies significantly. Examples include displaying information via static or dynamic webpages, databases, queryable Application Programming Interfaces (APIs), or interactive sky maps. Table 3.3 summarizes important systems, each offering particular value for studying transient events. Note that most services focus on specific types of events and only when combined with other services in the table provide a comprehensive view of transient events.

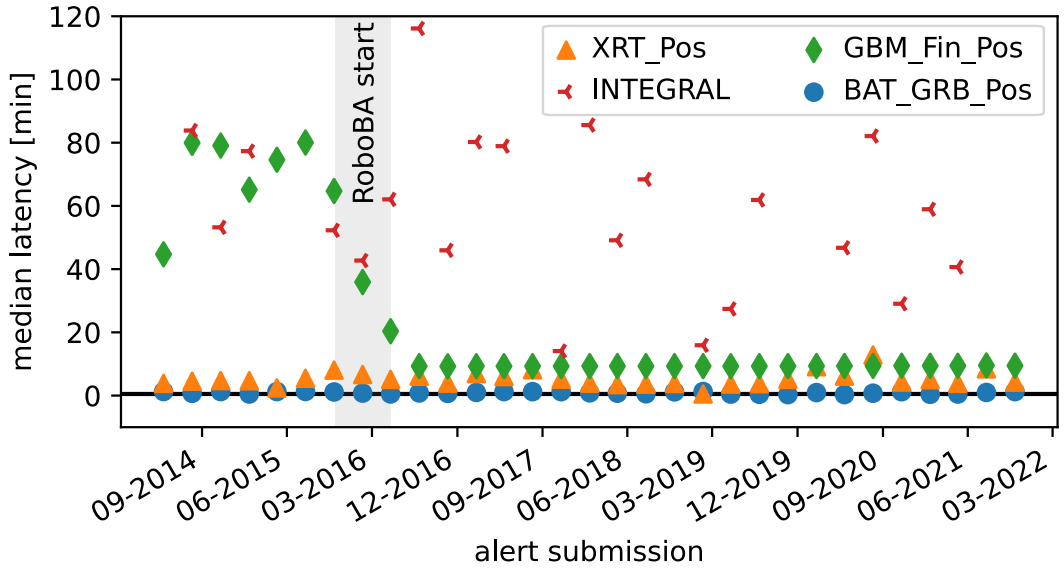

Figure 3.4: The median latencies of alerts per quarter since 2014 for the final VOEvents of the types *GBM_Fin_Pos*, *INTEGRAL#Offline*, *XRT_Pos*, and *BAT_GRB_Pos*. The vertical bar indicates approximately the start of the automated localization algorithm RoboBA used for the GBM final position alerts.

Table 3.3: Astro-COLIBRI provides customized links to the following services for each event and source (if available) to provide convenient access to specific, more detailed information on demand.

Service	Description
ASAS-SN[5]	All Sky Automated Survey for SuperNovae (ASAS-SN) is an automatic all-sky survey to detect SNs.
ALADIN [34]	Displays sources from catalogues or databases (DBs) in a sky map.
BAT [99]	Burst Alert Telescope (BAT) GRB event data processing report includes detailed info, a flux summary, spectra, and light curves.
ESA [118]	ESASky is an application that visualizes astronomical data in a sky map.
FAVA [9]	*Fermi* All-sky Variability Analysis (FAVA) for the selected position observed by the Large Area Telescope (LAT).
FINK [123]	Broker and science portal that provides source information about transients.
Gaia [85]	Gaia Photometric Science Alerts is an all-sky photometric transient survey, based on the repeated measurements of Gaia.
GBM[6]	Quicklook directory with near real-time (10-15 min after the *Fermi* BAT trigger) infos of light curves and spacecraft pointing history.
GCN-c[7]	Gamma-ray Coordinates Network circulars (GCN-c) inform in human-written reports about the observed event.
GCN-n[8]	GCN notices (GCN-n) deliver information about basic properties of transient objects in automatically generated alerts.

GraceDB[9]	Communications hub and DB with information about candidate gravitational-wave events and related electromagnetic events.
IBAS [117]	System for real-time detection of GRBs seen by INTEGRAL.
LAT-LCR[10]	DB of multi-cadence flux calibrated light curves for over 1500 variable sources from the 10 year *Fermi*-LAT point source catalog.
NED [110]	DB about galaxies and other extra-galactic objects, with more details, photometry, spectra and further references/links.
STARRS [113]	DB of images after analysis and processing obtained by the Pan-STARRS telescopes.
SkyMapper [130]	DB with a digital record of the entire southern sky, which stores images and catalogs from SkyMapper's Southern Survey.
SIMBAD [183]	Provides additional information, cross-identifications, bibliography and measurements of sources.
SSDC[11]	Display of Spectral Energy Distributions (SEDs) of astrophysical sources from the Space Science Data Center (SSDC).
Swift[12]	High-level information on the Swift BAT or XRT observations and links to other relevant references.
TeVCat [181]	Source catalog for very high energy gamma-ray astronomy with detailed source information and linked references.
TNS[13]	The Transient Name Server (TNS) provides discovery and classification reports of e.g. SNs and further info, e.g. spectra.
TOBY[14]	The Tool for Observation visiBilitY and schedule (TOBY) shows event visibility and schedule for a variety of observatories.
XRT [59]	Light curve, spectra, and comparison with other bursts provided by Swift's X-Ray Telescope (XRT).

3.1.3 Astro-COLIBRI

The various alert streams, which differ both in their level of the machine- or human-generated content and in the underlying communication technology, e.g., emails, websites, databases, and VOEvents, pose significant challenges for scientists to keep track of transients in real-time. Astro-COLIBRI is a novel tool dedicated to this challenge by evaluating and filtering transient alerts based on user-specified criteria across different alert streams described in Section 3.1.1. Through the fast generation of an overview of transient events in the relevant phase space, Astro-COLIBRI contributes

[5] `https://www.astronomy.ohio-state.edu/asassn/index.shtml`
[6] `https://heasarc.gsfc.nasa.gov/FTP/fermi/data/gbm/triggers/`
[7] `https://gcn.gsfc.nasa.gov/gcn/gcn3_archive.html`
[8] `https://gcn.gsfc.nasa.gov/`
[9] `https://gracedb.ligo.org/latest/`
[10] `https://fermi.gsfc.nasa.gov/ssc/data/access/lat/LightCurveRepository/`
[11] `https://tools.ssdc.asi.it/SED/`
[12] `https://swift.gsfc.nasa.gov/archive/grb_table/`
[13] `https://www.wis-tns.org/`
[14] `http://integral.esa.int/toby/`

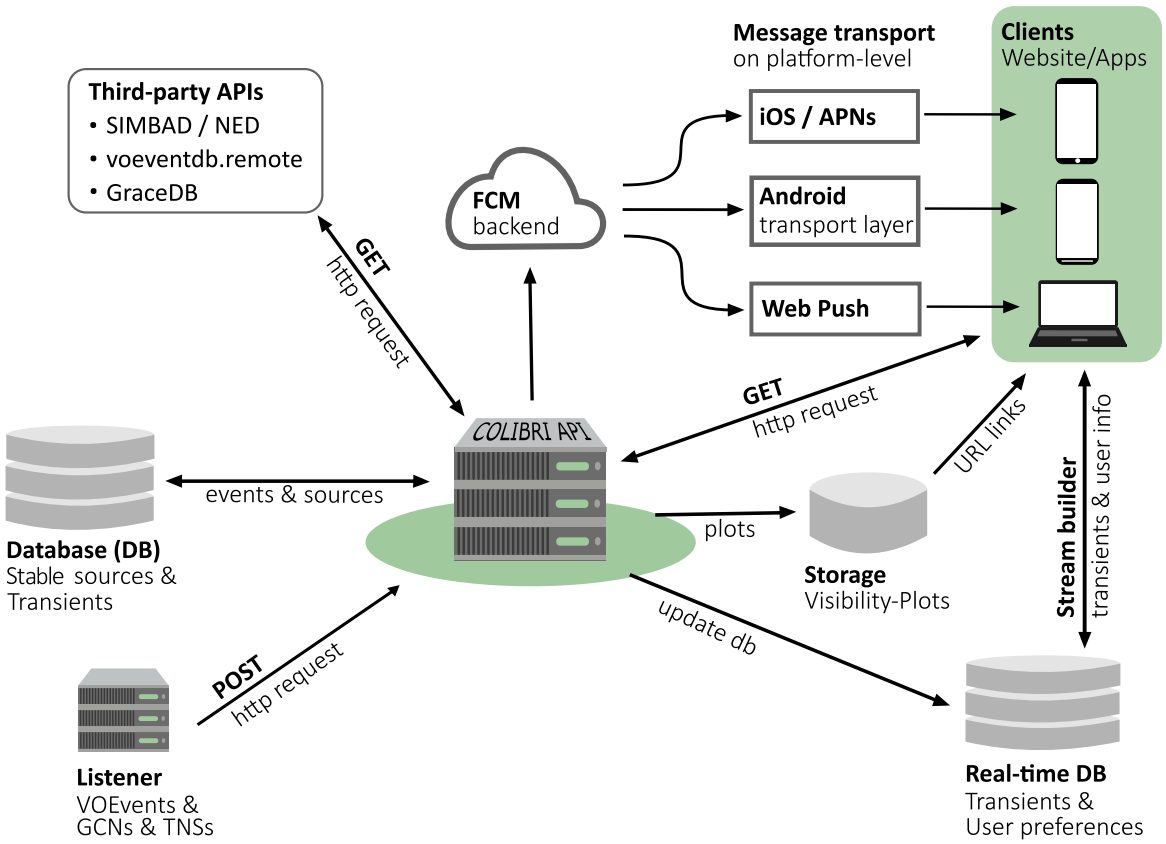

Figure 3.5: Architecture of Astro-COLIBRI comprises a REST API, both a static and a real-time database, a cloud-based alert system, as well as a website and apps for iOS and Android as clients. Public user interfaces are highlighted in green.

to an enhanced discovery potential of both serendipitous and follow-up observations of the transient sky. To accommodate the growing range of services from the real-time multi-messenger ecosystem described in Sections 3.1.1 and 3.1.2, Astro-COLIBRI is modular in design and allows easy integration of additional third-party services. The software's architecture is shown in Figure 3.5 and comprises a Representational State Transfer (REST or RESTful) API, both a static and a real-time database, a cloud-based alert system, as well as user clients in the form of a website and apps for iOS and Android. Details of the design, along with key functionalities of Astro-COLIBRI, are presented in the following paragraphs.

Transients listener

The Astro-COLIBRI transient event listener is a background process permanently running on an Amazon Web Services (AWS) server that listens to VOEvents, TNS notifications, and GCNs. The VOEvent listener is building upon the *Comet* broker [173] and evaluates incoming alerts from AMON, *Fermi* GBM, International Gamma-Ray

Astrophysics Laboratory (INTEGRAL), SuperNova Early Warning System (SNEWS), Swift BAT and XRT, as well as UTMOST. The analysis of GCN circulars and TNS notifications is performed via a dedicated email parser. Alerts that align with the Astro-COLIBRI science cases are directed to the API for further processing. The API checks whether it is a new event or an update with more accurate information on an existing event and merges the available data by also complementing the data with third-party (e.g. TNS API) information. The *Fermi* GBM pipeline outlined in Section 3.1.1 is an example where several subsequent alerts with updated information must be merged and stored as one entry in the databases.

RESTful API as the central engine

The central engine in the overall Astro-COLIBRI architecture is the RESTful API built within the Flask framework using Python as the programming language, which allows the usage of well-established astronomy packages such as astropy [20] and astroquery [71]. The API provides endpoints that can be accessed from the Astro-COLIBRI clients and external services via GET and password-protected POST requests. The latter are only accessible by the Astro-COLIBRI team and its collaborators as they may modify the databases. The API performs the specified tasks and returns a JSON file with the computed and collected information. To arbitrarily scale the computation power and run on any cloud computing platform, the API runs in a Docker container. Currently, instances of the API are hosted on the cloud-computing platforms Heroku and AWS.

The API design is based on the model-view-controller (MVC) pattern with the following structure:

- Controller: Responsible for understanding client requests and initiating the appropriate calculations by calling the model functions.
- Models: Key functionality of the API is defined here in various classes and is operated by the controllers through corresponding user requests.
- Views: The views contain all HTML and CSS files that display the static content of the API website. The functionalities of Astro-COLIBRI and usage examples are provided there. General information and news are also displayed.

Cone search

Cone searches are one of the main functions in Astro-COLIBRI and allow the representation of a transient event in the context of other already known events or sources in the relevant temporal and spatial phase space. Cone searches around events of interest display known sources and other transient events that correspond to the user-specified filter criterion, such as time window and event types. The default radius of the cone

searches is 10° and the default time window is one month. The cone search endpoint of the API returns the list of all sources and transients found within the radius of 10°. This result is processed and displayed in the frontend.

Databases

As the different transient event types come with different typical properties, Astro-COLIBRI employs a non-Structured Query Language (NoSQL) data structure for its databases, where the stored data structure is flexible. Astro-COLIBRI uses two databases that are optimized for complementary tasks.

Astro-COLIBRI stores and continuously updates events in MongoDB via the API. This information is used for API-related computations and evaluations of novel alerts. This database is also used for cone-search queries.

In order to meet the real-time approach, Astro-COLIBRI also uses a Firebase Firestore real-time database that provides a direct stream to all clients. This data stream populates changes in the databases in real-time to the frontend devices without the need to reload the web interface or application. This database is maintained from the API to stay up to date. This configuration supports offline usage, as all relevant data is saved locally on devices, and all changes are automatically synchronized between the clients and the database when the device comes back online. Expressive querying is possible through the support of combined and chained filters and queries in combination with an efficient zig-zag merge join algorithm. This offers both high-performance and flexible operation and is used for filtering by event type and time interval of the latest transients.

Push notification stream

Alerts are filtered and classified in the transient listener and sent via the cloud-based Firebase Cloud Messaging (FCM)[15] service as cross-platform push notifications to the users of Astro-COLIBRI. Users can decide the type of notifications they want to receive by changing the user settings in the menu.

Frontend user-interface

The frontends provide a graphical representation with a summary of the relevant data to allow for the fast identification of interesting phenomena along with an assessment of observing conditions at a large selection of observatories around the world. The sky map, where the events and sources are shown in the relevant phase space, can be zoomed and panned. Sources and events can be selected directly from the map or from the attached list. In the list, the sources and events contained in the cone search are listed in ascending order according to the distance to the cone-search center.

[15] `https://firebase.google.com/docs/cloud-messaging`

Cone searches around events of interest display known sources and other transient events corresponding to the user-specified filter criterion, such as time window and event types. The observation uncertainty reported in the alert of the transient event is visualized by the boundary matching the color of the marker. For the case of gravitational waves, contours of different confidence levels are shown instead.

A key feature in the frontend is the listing of detailed information and customized links that point directly to the selected event in services offered by the astronomical community. This allows for direct access to supplementary information and allows the use of Astro-COLIBRI as a single platform providing the user with an easy-to-access overview of relevant information. Table 3.3 summarizes services that are currently supported. A separate area in the frontends is dedicated to the display of the information and the links. The visibility for user-specified or known telescope locations for the transient is calculated in the API and also shown in this area.

3.1.4 Follow-Up Observations

After outlining the first steps of the pipeline presented in Figure 3.1 in the previous subsections, this subsection is devoted to the triggering of the follow-up observations to obtain a multi-messenger view of transient events. Follow-up observations can be initiated automatically by alert pipelines or by burst advocates from observatories manually. When deciding on the execution of follow-up observations, the timescales of the expected flare, the telescope capabilities, and the visibility must be considered. In addition, the pointing pattern must be chosen to maximize the probability of observing the associated multi-wavelength or multi-messenger counterpart emission from the initially observed transient event, especially when its reported localization uncertainty is large. Using efficient algorithms is essential for follow-up campaigns of GW signals with larger uncertainty regions than the field-of-view of the triggered observatories. Tiling strategies are discussed in [19] for finding a sequential order of individual pointings of IACTs, with a focus on H.E.S.S.-follow-up campaigns.

In addition to automatic follow-up observations, manually triggered ones are of great importance, especially when transients are detected at times that are not suitable for observations of a telescope due to its visibility constraints. This is, for example, the case for all alerts that are circulated during the day and can only be observed by IACTs during dark time. Then there is still enough time to trigger manual observations with an all-encompassing information overview given by e.g., Astro-COLIBRI.

AGN Follow-Up Observations with H.E.S.S.

The preceding discussion illustrates that transport-related physics introduces relevant real-time effects in multi-messenger astronomy. Especially the strong turbulent magnetic fields in source environments induce transport effects, which affect the escape times and spectra of the charged CRs. Interactions inherit these properties from CRs

to secondaries. The specifics of various interaction and acceleration processes introduce another layer of complexity.

The complexity and variety of processes and scenarios in transient phenomena require observing these events with complementary messengers. The observation duration should extend over the event-dependent characteristic timescales. Proper orientation for the expected emission variation in the context of hadronic emission is the escape times of protons from the source environment with high target density (see [25] in the context of blazar flares). Since the escape times scale with the size of the environment (quadratic for diffusive transport and linear for ballistic transport), estimates depend heavily on this often unknown parameter. These uncertainties complicate the analytical predictions for the further evolution of flares when a single measurement of an elevated state of a source is observed from a monitoring satellite.

As a result, the decision for the necessity of follow-up observations frequently undergoes evaluation by burst advocates based on pre-defined criteria and the current observation data provided by the alert. The often unclear multi-wavelength picture requires incorporating experience with similar historical events and the current visibility of the event.

The H.E.S.S. AGN ToO program serves to illustrate this process.

Burst Advocates and Shift Crews There are two active burst advocates in the H.E.S.S. AGN ToO, a monitoring person and a principal investigator (PI). The monitoring person monitors the information provided and shared by multi-wavelength observatories on the activity of sources that fall in the visibility window of H.E.S.S. and responds to alerts from monitoring satellites. Astro-COLIBRI is ideally suited to support the burst advocates for this task, as, for example, it sends relevant alerts from the FlaapLUC analysis [102] of *Fermi* sources used in H.E.S.S. directly to mobile phones as push notifications. Then, the burst advocates can evaluate the relevance of the flare directly in Astro-COLIBRI based on additional information provided in the interface. Short- and long-term light curves, spectra, and links to further resources are accessible in Astro-COLIBRI. Furthermore, Astro-COLIBRI evaluates the event's visibility for the selected follow-up observatory, where the burst advocates can instantaneously plan the observations. In case of a decision of the PI for follow-up observations, the shift crew is instructed about the observation plan with the event and visibility info provided by Astro-COLIBRI. Then, the shift crew will perform the observation.

Continuation of Follow-Up Observations After each observation night, the real-time analysis of the H.E.S.S. observations, together with the current multi-wavelength overview of the source will be discussed within the working group. Depending on the status of the follow-up campaign, an extension of the observations is scheduled. The follow-up observations can again be optimized with the visibility of the source of H.E.S.S. provided by Astro-COLIBRI, considering the telescope-specific conditions.

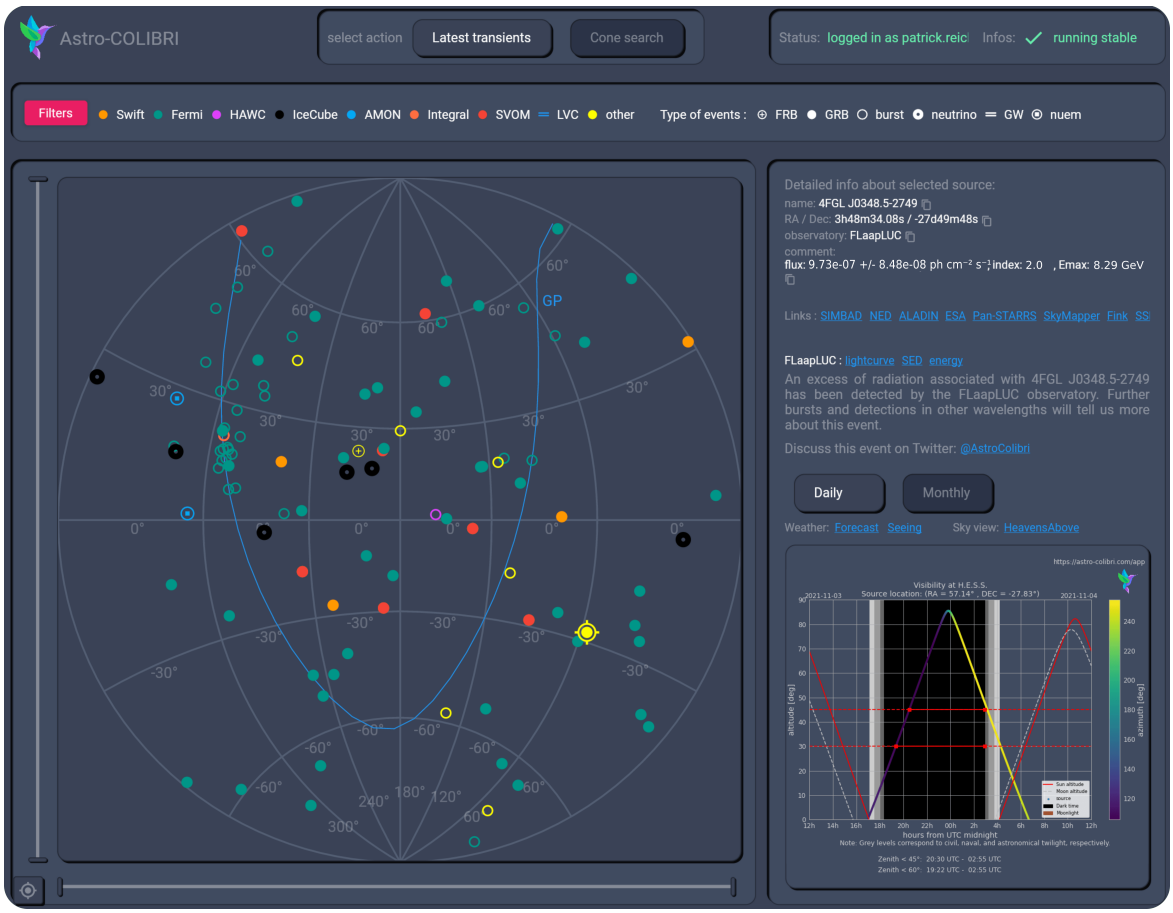

Figure 3.6: Website of Astro-COLIBRI providing necessary information for planning follow-up observations of the selected source PKS 0346-27. At the top are setting and filter options, on the left the map with the source position, and on the right detailed information about the selected event. The middle panel from the website with a list of alerts is removed in this figure. The right info area contains links to other websites with detailed information, light curves, the spectrum, and at the bottom, detailed (and long-term) visibility information for the specified observatory. Here H.E.S.S. is selected. Note that access to FlaapLUC alerts within Astro-COLIBRI is restricted to H.E.S.S. members.

H.E.S.S. Detection of the most distant VHE AGN: PKS 0346-27 I acted as a burst advocate throughout my Ph.D. One highlight is the detection of VHE emission from PKS 0346-27 discussed here. *Fermi*-LAT observed an enhanced gamma-ray flux from the flat-spectrum radio quasar PKS 0346-27 and issued on October 31 2021 a ground-generated flare alert[16]. PKS 0346-27 is a distant blazar with a redshift $z = 0.99$ [21, 184], and thus an interesting object for EBL studies [18]. Therefore, the AGN ToO within H.E.S.S. triggered follow-up observations with the H.E.S.S. observatory, given the good visibility as shown in the Astro-COLIBRI web interface in Figure 3.6.

[16] `https://gcn.gsfc.nasa.gov/other/1635691656_fermi.txt`

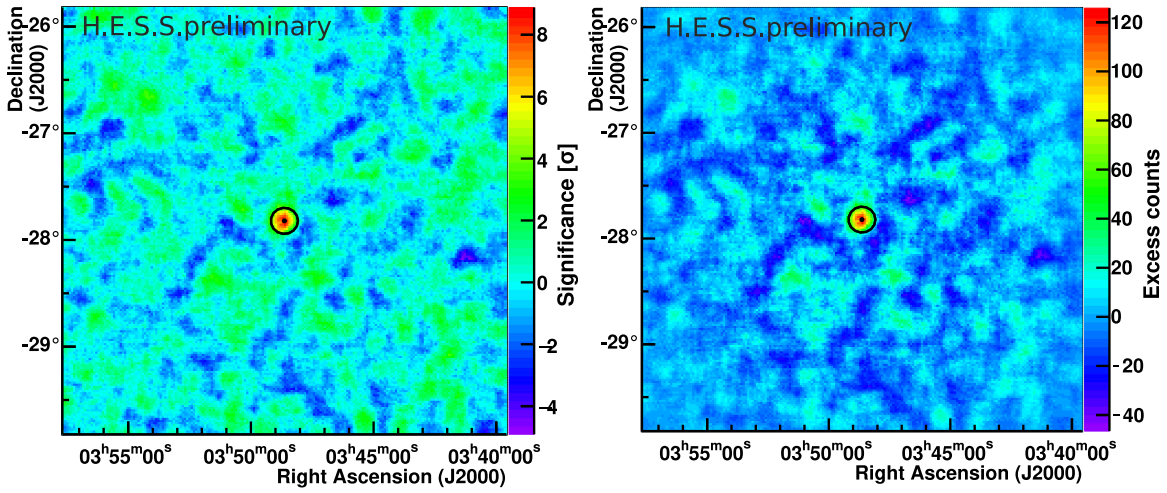

Figure 3.7: Significance (left) and excess (right) maps of the H.E.S.S. detection of PKS 0346-27 on November 3 accumulated over a total of $\approx$ 111 minutes observation.

The visibility plot on the bottom right shows the altitude of PKS 0346-27 as seen by H.E.S.S. as a function of time during 24 hours. The detection in H.E.S.S. is during the shown night.

The real-time analysis result showed the detection of the source during four observation runs on November 3, 2021, with a total of $\approx$ 111 minutes. The observation data were subsequently analyzed with the H.E.S.S Model++ data calibration, and analysis chain [48] using the H.E.S.S.I Stereo configuration. This configuration takes only events into account that were recorded by at least two out of the four 12 m-telescopes (CT1-4). Furthermore, considering the distant source (redshift $z \approx 1$) and the assumption of a soft spectrum due to EBL absorption, a *very loose cut* is employed during the analysis. This cut reduces the energy threshold compared to the standard case and increases the fraction of events passing the cut [10].

The preliminary results of this analysis are shown in Figure 3.7. The left panel shows the significance map, and the right panel shows the excess map during the four runs. The significance and excess are elevated around the center of the source region (central black dot).

The number of gamma-like events as a function of their squared-angular distance Θ^2 to the center of the source region is shown in the histogram in Figure 3.8. Here, the *ring background* method (see [30] for details) is employed, exploiting the wobble observation mode and classifying the gamma-like events (ON) in a central circular region with radius r_{ON} around the camera center. The background gamma-like events are labeled as OFF within a hollow circular disc, whose inner radius is larger than r_{ON}. The acceptance in the ON and OFF region is the same, and only their geometrical size is different. The α factor accounts for the different exposure of the ON and OFF

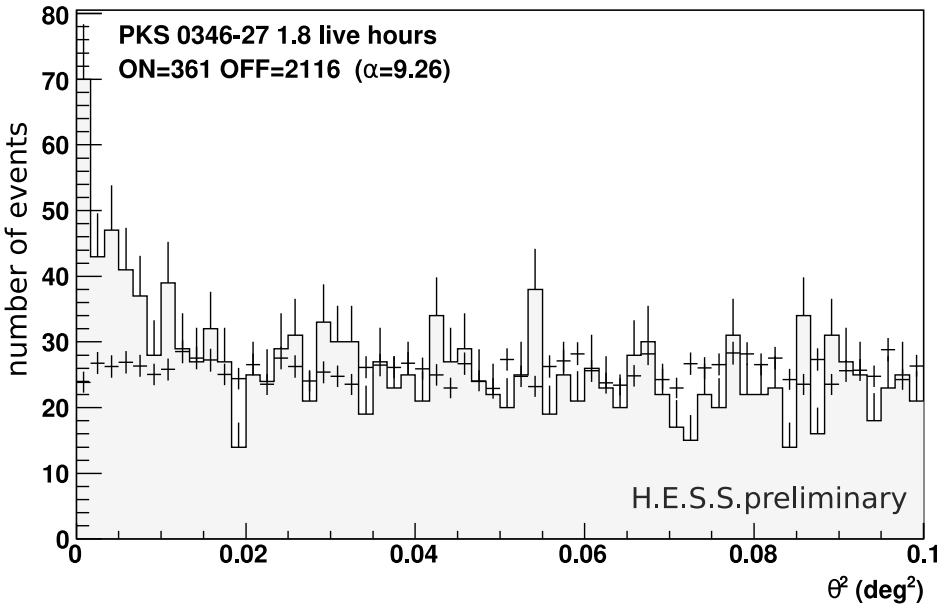

Figure 3.8: Histogram of the squared angular distance of ON and OFF events. Latter are scaled by the factor α and presented as data points with uncertainties.

region [104]. This factor scales the OFF events displayed in Figure 3.8. A clear excess of the ON events over the rather constant number of OFF events is visible at the source region (small Θ^2), leading to a detection with a significance of $7.6\,\sigma$.

This detection elevates the source PKS 0346-27 to the most distant very-high energy AGN, surpassing the blazar S3 0218+35 ($z = 0.944$) [12]. This finding was communicated with an ATel #15020[17] and is currently in preparation for publication.

[17] https://www.astronomerstelegram.org/?read=15020

3.2 Simulation Software

In Chapter 2, various transient phenomena were introduced. With the ever-increasing amount of complementary information provided by observations of different messengers and photon wavelengths during transient events, sophisticated theoretical models of the underlying physical processes are required to explain the combined multi-messenger and multi-wavelength signatures. While analytical models may describe the basic properties of transient objects, details of the flaring character of transients remain largely unresolved. To address this problem, numerous simulation software have been developed and optimized for different applications. The software differ not only in their degree of generality but also in their use case. For example, there is software that is optimized for modeling AGN jets [25, 36, 43, 54, 66, 86]. Currently, it is not possible to describe the entire transient event in detail, from potential jet generation (e.g. in the case of GRBs [74]), to the generation of relativistic plasmoids, to the complex and nonlinear transport and interaction dynamics of the particles within the rapidly changing system. Therefore, software must focus on individual aspects of the overall picture and take as input, or boundary conditions, findings from other simulations, analytical theories, and observations.

With the observable multi-messenger signatures playing a key role in the scope of this work, the following discussion focuses on modeling the nonlinear transport and interaction properties of particles within systems of transient events. Due to this focus and the limitation of current numerical simulations in the context of the currently available computing power, components such as the magnetic field, external photon fields, and matter densities are taken as input. Note that these components cannot all be dynamically modeled self-consistently in one simulation at all astrophysical scales. In the following, these input components are addressed sequentially.

3.2.1 Magnetic Fields in Simulations and Astrophysics

The transport properties of charged particles depend on the magnetic field structure through which they move. Figure 3.9 presents a schematic overview of magnetic fields that CRs encounter during their propagation from sources towards Earth. These magnetic field components have to be modeled in numerical simulations. The complexity of the different regions can be broken down to the superposition of turbulent fields and oriented background fields with a wide variety of scales and properties. These two components are discussed in more detail below.

Magnetic turbulence Magnetic turbulence plays a crucial role in particle transport and radiation processes in many astrophysical environments. Since turbulence is driven on many scales, from system sizes to kinetic scales by cosmic rays themselves [29], it affects particles of all energies up to ultra-high-energy CRs (UHECRs) in strong magnetic fields. To account for these important effects on multi-messenger signatures,

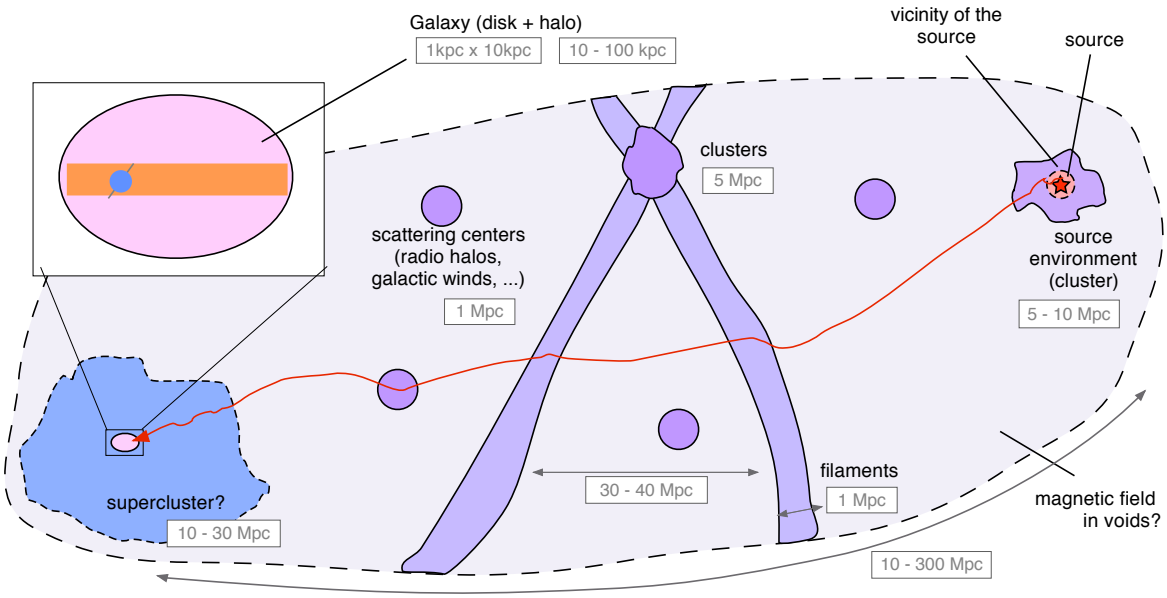

Figure 3.9: Schematic representation of magnetic fields that CRs encounter during their propagation from sources towards Earth. Figure taken from [98].

the large dynamic scales of turbulence must be modeled as realistically as current computing power allows in numerical simulations. The magnetic field dynamics are negligible [61] when compared to the relevant timescales of transport effects of high-energy CRs discussed in the present thesis, i.e., irregularities of the magnetic field move at the Alfvén speed. These irregularities are thus much slower than particles that move relativistically with $\sim c$ (see further details in [92]). For this reason, stationary magnetic fields without electric fields will be considered in the following.

There are two fundamentally different approaches to generating stationary magnetic turbulence in astronomical environments. On the one hand, these can be generated by magnetohydrodynamic simulations. This approach includes further aspects of the known properties of the turbulence and results in realistic descriptions of turbulence. Note that this complexity may obscure the fundamental relationships between the spectrum of turbulence and the transport behavior of the particles through the introduction of additional effects. On the other hand, simple models based on analytical considerations as well as direct and indirect measurements of magnetic turbulence can be employed. These models characterize the energy spectrum and orientation of the magnetic fluctuation (see [24] for a review). In this work, we follow the literature (see, e.g., [42, 69, 166]) and focus on the 3D isotropic Kolmogorov turbulence with a 3D spectral behavior of $G(k) \propto k^{-11/3}$ with k being the wavenumber, although many of the findings are applicable to other models, such as the Kraichnan turbulence model. Whereas magnetohydrodynamic turbulence is more realistic, the generated dynamical scales are much smaller than possible with Kolmogorov models.

Technically, the generation of Kolmogorov turbulence for numerical simulations

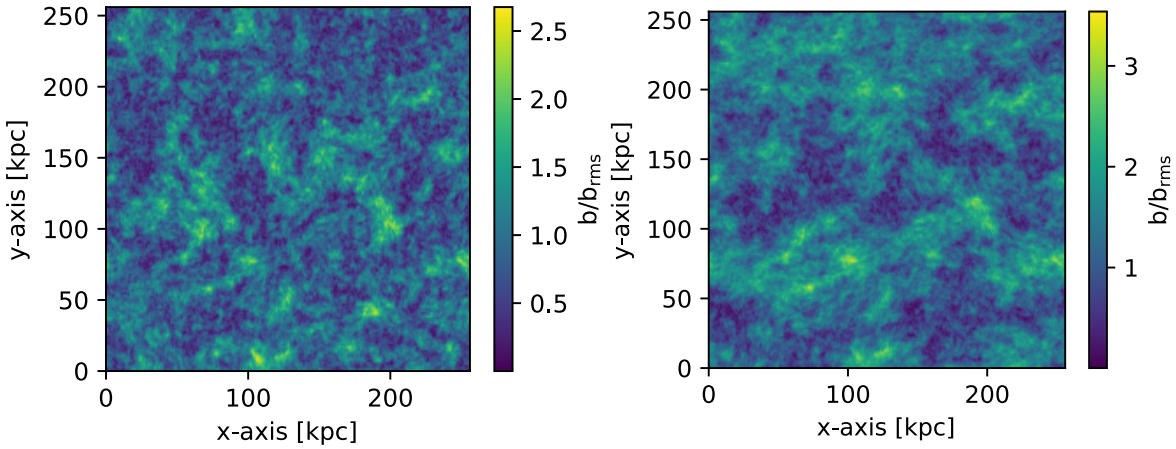

Figure 3.10: Slice plots of the synthetic Kolmogorov turbulence with $\delta B = 1\,\mu$G (left) and its superposition with a background field with $B_0 = 1\,\mu$G aligned in y-axis direction. The grid-method with 512^3 grid points is used for generating the field, which is sampled using the linear interpolation routine. The outer scale $l_{\mathrm{max}} = 100\,$kpc and the minimum fluctuations $l_{\mathrm{min}} = 1\,$kpc of the turbulence determine the correlation length $l_{\mathrm{c}} \approx 20\,$kpc.

can be implemented by means of the summation of planar waves with different wave numbers, amplitudes, and directions. The generated turbulence can either be stored as discrete magnetic field vectors on a large grid with N^3_{grid} grid points by using a discrete inverse Fourier transform in advance of the numerical simulation. At any location, the magnetic field vector is computed via interpolating the surrounding grid points (see e.g. [153]). Figure 3.10 shows a slice of the turbulence structure (left panel) and compares it with its superposition of an ordered background magnetic field in y-direction (right panel). Alternatively to storing the turbulence on a grid in advance, the summation of different amplitudes, wavenumbers, and directions can be performed at run time at the exact position needed (*plane-wave* (PW) *turbulence*) [69, 174]. See [153] for a detailed comparison of both approaches.

In fact, findings on the transport behavior of charged particles in Kolmogorov turbulence models constitute an important contribution to the field of multi-messenger modeling, where substantial current work relies on Kolmogorov turbulence models. Furthermore, it provides a useful stepping stone for studies with more realistic magnetohydrodynamic turbulence models.

Large-scale magnetic field In addition to turbulence, many astrophysical environments have formed a directional, large-scale magnetic field. Examples of this are the spiral field of the Milky Way and other galaxies, but also large-scale structures in jets. The latter can be studied with general-relativistic magnetohydrodynamics simulations. Figure 3.11 shows the large-scale 3D morphology of the M87 jet and disk from a 3D general-relativistic magnetohydrodynamics simulation of a magnetically arrested

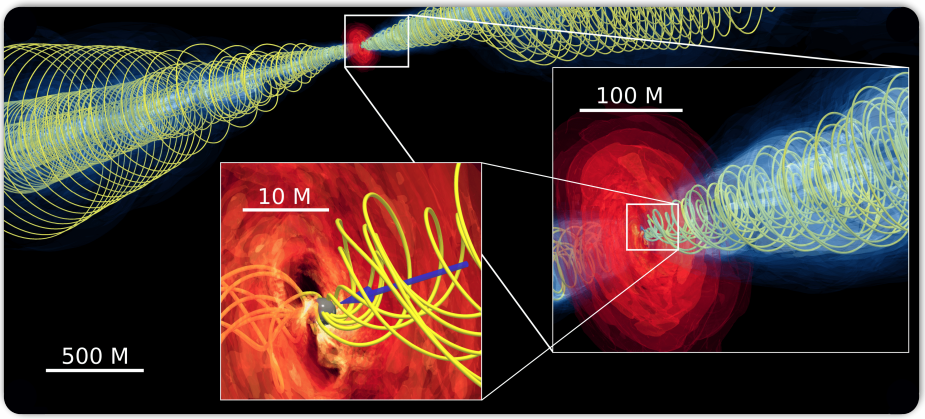

Figure 3.11: Large-scale 3D morphology of the M87 jet (blue) and disk (red) from a 3D general-relativistic magnetohydrodynamics simulation. The spiral magnetic field is shown in yellow. Taken from [47] and slightly modified.

disk around a central black hole. The large-scale spiral magnetic field is displayed in yellow.

The Galactic magnetic field is not only relevant for Galactic CRs, but also for extra-galactic UHECRs. The Refs. [91] describe a popular magnetic field model of the Milky Way. Ref. [96] is an updated model without violations of the magnetic divergence constraint and an improved x-shaped poloidal halo field in the Galactic disc. Combined with models for the Galactic center zone [76], the halo [176], and an outer Archimedean spiral component [93], a realistic, large-scale model of the galactic magnetic field can be used in numerical simulations.

3.2.2 Charged Particle Propagation Methods

Current simulation frameworks propagate charged particles through magnetic fields either by ballistic codes solving the Lorentz force at each step or by using particle distributions arising from the solution of the classical diffusion equation. Whereas the former method accurately describes the particle trajectories using small step sizes, this method is computationally expensive. Therefore, the accompanied simulation times are substantial for low particle energies with small gyroradii that must be resolved. The method based on the diffusion equation, on the other hand, is extremely fast since the particle distribution is analytically given at each time point. But, by the nature of the method, particles can only be described statistically. Nevertheless, for applications in which statistical statements and averaging over many particles are intended, this method is preferred in many areas of astronomy because of the short simulation times, e.g., in the Galaxy. It is essential to note that the diffusion equation guarantees a formal description of the particles only in the limit of infinitely large times. Numerically, however, this approach can also be used as soon as a diffusive behavior

occurs. This typically happens after a simulation time in the order of magnitude of the mean-free paths divided by the speed (details are discussed in Chapter 4).

Solving the Equation of Motion

The Equation of Motion (EoM) is given by the Lorentz-Newton equation

$$\frac{\mathrm{d}\mathbf{v}}{\mathrm{d}t} = \frac{q}{mc}(\mathbf{v}(\mathbf{r},t) \times \mathbf{B}(\mathbf{r},t)) \,, \tag{3.1}$$

with the mass m, speed c, particle velocity $\mathbf{v}$, magnetic field $\mathbf{B}$, and charge q of the particle. Integrating the EoM of charged particles in magnetic fields yields their trajectory. Note that the local magnetic field vector $\mathbf{B}(\mathbf{r},t)$ must be known in each integration step. There are many different algorithms available for computing the particle trajectory. The Runge-Kutta type Cash-Karp (CK) method [41] and the Boris-Push (BP) method [35] are two well-tested ones [17, 137]. Both algorithms support adaptive step sizes. The BP method is intrinsically energy-conserving. The BP method applies a leapfrog integration scheme.

The first order differential equation $\mathrm{d}\mathbf{v}/\mathrm{d}t = f(t,\mathbf{v})$ can be numerically solved with an embedded nth order Runge-Kutta method via

$$v_{n+1} = v_n + h\sum_{i=1}^{s} b_i k_i \,, \tag{3.2}$$

with

$$\begin{aligned} k_1 &= f(t_n, v_n) \,, \\ k_2 &= f(t_n + c_2 h, v_n + h(a_{21}k_1)) \,, \\ &\vdots \\ k_i &= f\left(t_n + c_i h, v_n + h\sum_{j=1} i - 1 a_{ij} k_j\right) \,. \end{aligned}$$

Here, the error in an integration step is determined by comparing the nth-order formula with different lower-order Runge-Kutta expressions. In order to limit the local error, the step size can be adapted accordingly. A popular algorithm with adaptive step sizes to integrate the EoM of charged particles in magnetic fields is the CK method. The CK method does not conserve particle energy, even when only considering a charged particle in a magnetic field without electric fields or other energy-loss processes. This issue can be fixed by manually enforcing the conservation of energy. See the CRPropa framework for an example of such an energy-conserving implementation. This fix influences the evolution of the momentum components and may cause numerical errors over large simulation times. The issue of the missing energy conservation can alter-

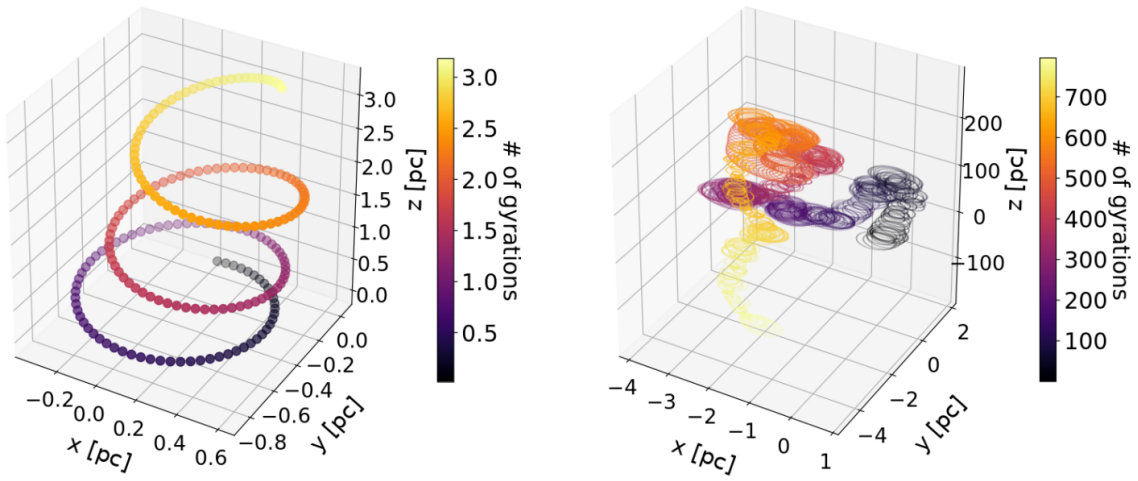

Figure 3.12: Charged particle trajectory in turbulence plus an ordered magnetic field along the z-axis simulated with an EoM approach. The first gyrations (left panel) show the initial ballistic character of the trajectory, while the diffusive behavior dominates in the limit of large times (right panel). Taken from Reichherzer (2018, [146]).

natively be solved by choosing small step sizes that result in a good resolution of the particle trajectory. In doing so, the local numerical error remains small. This ensures an almost energy- and momentum-preserving behavior for the propagation of charged particles in the magnetic field.

In contrast to implicit methods, explicit methods only evaluate the Lorentz-Newton equation from the previous step, which requires smaller step sizes but improves the simulation speed per step.

Figure 3.12 shows the trajectory of a charged particle in a large-scale magnetic field along the $x_3(:= z)$-axis plus a turbulent component. While both panels show the same trajectory, only the first three gyrations are shown in the left panel. This initial phase is dominated by the gyration motion caused by the directed field. After many gyrations, the random-walk character caused by the turbulent component of the magnetic field becomes dominant. This chaotic motion (right panel) can be statistically described by a transport equation, leading to an efficient propagation routine, as described below.

Solving the Transport Equation

Besides solving the equation of motion of single particles, the dynamics of particles as an ensemble can be described statistically via the Parker-transport equation introduced in Section 2.3. This equation describes the temporal change in n by taking into account spatial diffusion and advection, momentum diffusion, adiabatic energy changes as well as sources and sinks.

The transport equation can be solved numerically either discretized in real and

momentum space (e.g. [60, 171]), or by transformation into stochastic differential equations [119].

- **Diffusion Equation:** Assuming position-independent spatial diffusion as the only transport mechanism and neglecting all other terms from the Parker-transport equation results in the diffusion equation

$$\frac{\partial n}{\partial t} = \sum_i \kappa_i \frac{\partial^2 n}{\partial x_i^2} \,, \tag{3.3}$$

  where i indicates the three spatial directions.

- **Telegraph Equation:** The telegraph equation modifies the diffusion equation by taking the initial ballistic propagation phase into account by means of an additional term [106–108, 175]

$$\frac{\partial n}{\partial t} + \tau_{\text{diff}} \frac{\partial^2 n}{\partial t^2} = \sum_i \kappa_i \frac{\partial^2 n}{\partial x_i^2} \,, \tag{3.4}$$

  where τ_{diff} is the timescale for particles to become diffusive. The relevant parameters of the correlated random walk (CRW) can be determined from the diffusion coefficient. In contrast to the diffusion equation, the telegraph equation describes the particle density also during the initial ballistic transport. By neglecting adiabatic focusing, the diffusion timescale yields [25, 106]

$$\tau_{\text{diff}} = \frac{3v}{8\lambda_\parallel} \int_{-1}^{1} \mathrm{d}\mu \left(\int_0^\mu \mathrm{d}\mu' \frac{1-\mu'^2}{D_{\mu\mu}(\mu')} \right)^2 \,, \tag{3.5}$$

  where $D_{\mu\mu}$ denotes the pitch-angle Fokker-Planck coefficient [160]

$$D_{\mu\mu} = (1-\mu^2) D \,. \tag{3.6}$$

  Here, for strong turbulent magnetic fields δB and weak ordered background magnetic fields B_0 ($\delta B \gg B_0$) yields in the quasi-linear approximation the pitch-angle Fokker-Planck coefficient $D \propto |\mu|^{q-1}$, with $q = 1$ [92, 106]. On the other hand, the parallel mean-free path $\lambda_\parallel$ yields

$$\lambda_\parallel = \frac{3v}{8} \int_{-1}^{1} \mathrm{d}\mu \frac{(1-\mu^2)^2}{D_{\mu\mu}(\mu)} \,. \tag{3.7}$$

Therefore, τ_{diff} can be expressed in the quasi-linear approximation with $q = 1$ as

$$\tau_{\mathrm{diff}} = \frac{\lambda_{\parallel}}{v} = \frac{3\kappa_{\parallel}}{v^2}. \tag{3.8}$$

This equation is derived alternatively in Section 4.3 (see Equation (4.43)) using the Taylor-Green-Kubo (TGK) formalism and exponentially decaying velocity correlations. Note that the simple diffusion equation is obtained as a limit of $\tau_{\mathrm{diff}} = 0$ from the telegraph equation. With this choice, particle transport is considered diffusive from the beginning. This is inaccurate in the initial transport regime, as shown in Figure 3.12.

Correlated Random Walk

The concept of the correlated random walk (CRW) has been discussed in various contexts in the literature, such as when describing animal trails (see e.g. [45]). Cosmic-ray propagation can also be described via a CRW [157] as will be demonstrated in the following.

First, when considering only one dimension, particles can move in the positive direction α, and in the negative direction β. In each propagation step of the CRW, two substeps are performed. The particle changes its direction with the probability $\epsilon = \xi\tau_{\mathrm{s}}$ in the first substep. The second substep moves the particle along the direction established in the first substep for a time interval τ_{s}.

Therefore, the particle distributions in both directions after one propagation step yields

$$\alpha(x, t + \tau_{\mathrm{s}}) = (1 - \xi\tau_{\mathrm{s}})\alpha(x - \chi, t) + \xi\tau_{\mathrm{s}}\beta(x - \chi, t), \tag{3.9}$$
$$\beta(x, t + \tau_{\mathrm{s}}) = \xi\tau_{\mathrm{s}}\alpha(x + \chi, t) + (1 - \xi\tau_{\mathrm{s}})\beta(x + \chi, t). \tag{3.10}$$

The transport equation follows after a few computations described in e.g. [45] and presented in the following. For convenience the definitions $\alpha(x, t) \coloneqq \alpha$ and $\beta(x, t) \coloneqq \beta$ are introduced. Expanding Equations (3.9) and (3.10) for small propagation steps $\tau_s, \chi \to 0$ yields

$$\frac{\partial\alpha}{\partial t} = -v\frac{\partial\alpha}{\partial x} + \xi(\beta - \alpha), \tag{3.11}$$
$$\frac{\partial\beta}{\partial t} = v\frac{\partial\beta}{\partial x} - \xi(\beta - \alpha). \tag{3.12}$$

Summing Equations (3.11) and (3.12) for each component yields

$$\frac{\partial(\alpha + \beta)}{\partial t} = v\frac{\partial(\beta - \alpha)}{\partial x}. \tag{3.13}$$

The time derivative is

$$\frac{\partial^2(\alpha+\beta)}{\partial t^2} = v\frac{\partial^2(\beta-\alpha)}{\partial t\,\partial x}. \tag{3.14}$$

Substracting component-wise Equation (3.11) from Equation (3.12) and derivating with respect to x results in

$$\frac{\partial^2(\beta-\alpha)}{\partial t\,\partial x} = v\frac{\partial^2(\alpha+\beta)}{\partial x^2} - 2\xi\frac{\partial(\beta-\alpha)}{\partial x}. \tag{3.15}$$

Inserting Equation (3.15) into Equation (3.14) yields

$$\frac{\partial^2(\alpha+\beta)}{\partial t^2} = v^2\frac{\partial^2(\alpha+\beta)}{\partial x^2} - 2\xi v\frac{\partial(\beta-\alpha)}{\partial x}, \tag{3.16}$$

while inserting Equation (3.13) into Equation (3.16) yields

$$\frac{1}{2\xi}\frac{\partial^2(\alpha+\beta)}{\partial t^2} = \frac{v^2}{2\xi}\frac{\partial^2(\alpha+\beta)}{\partial x^2} - \frac{\partial(\alpha+\beta)}{\partial t}. \tag{3.17}$$

Finally, with $n = \alpha + \beta$, the following transport equation is derived:

$$\frac{1}{2\xi}\frac{\partial^2 n}{\partial t^2} = \frac{v^2}{2\xi}\frac{\partial^2 n}{\partial x^2} - \frac{\partial n}{\partial t}. \tag{3.18}$$

In fact, assuming local homogeneity, this approach can be generalized for 3D into the telegraph equation defined in Equation (3.4). As the statistics of particles that follow CRW can be described by the telegraph equation [107, 175], both the initial ballistic phase and the diffusive phase can be modeled. Therefore, the propagation mechanism based on the correlation of the directions of motion from subsequent propagation steps exhibits an enhancement of the classical random walk. The PropPy software propagates charged particles by means of the CRW.

3.2.3 Modeling Interaction and Energy-Loss Processes

Software for the numerical investigation of transient phenomena must model not only the transport of particles but also their interactions, as they influence the observed multi-messenger signatures, as discussed in Section 2.2. Essential aspects that tools have to cover are outlined in the following.

While individual interaction processes can be described analytically, realistic studies require numerical modeling of the nonlinear interplay of the different processes, in which, in addition to the primary particles, all secondary particles also interact with each other and serve as target material for other processes. Figure 3.13 shows an overview of the relevant processes of the individual messengers. Different magnetic fields, particle densities, and acceleration processes of high-energy particles in different source types lead to different source-specific multi-messenger signatures through

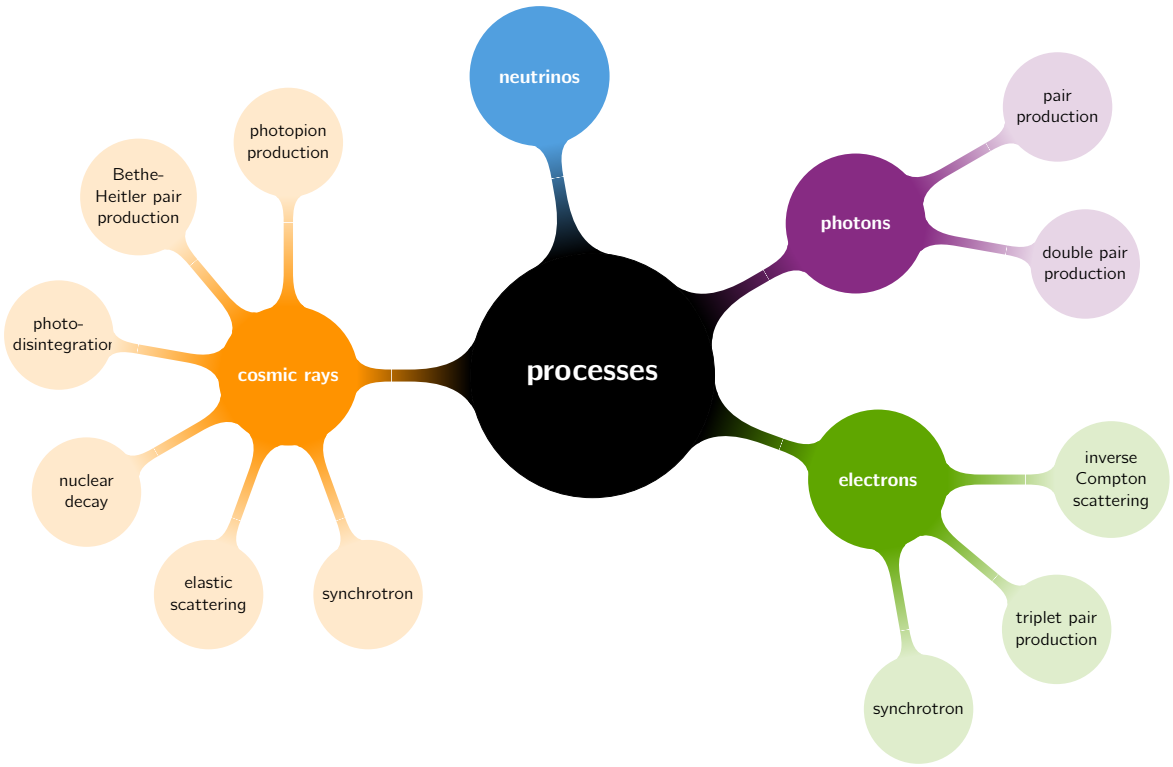

Figure 3.13: Schematic overview of various messengers and their relevant interaction and energy-loss processes. Credit: Rafael Alves Batista.

interaction processes. But also, different sources in one source class may differ due to varying conditions. Across different source types, the general discussion in the literature is centered on hadronic versus leptonic models, which may, in particular, shed light on the question of the origin of cosmic rays.

A clear sign for hadronic processes is the generation of neutrinos. Given the observed flux of high-energy neutrinos, there must be sources in which hadronic processes play a role. Numerical simulations must, therefore, provide the ability to model (photo-)hadronic interactions, where the production of pions play a key role[18],

$$p\,p \quad \rightarrow \quad \sum \pi^{\pm,0}, \tag{3.19}$$

$$p\,\gamma \quad \rightarrow \quad \begin{cases} \Delta^{+} \rightarrow (p + \pi^{0}) \,/\, (n + \pi^{+}) \\ \sum \pi^{\pm,0} \end{cases}, \tag{3.20}$$

[18]Kaons can also contribute, in particular at higher energies. Hadrons with heavier quark content can play a role in very dense environments [24]

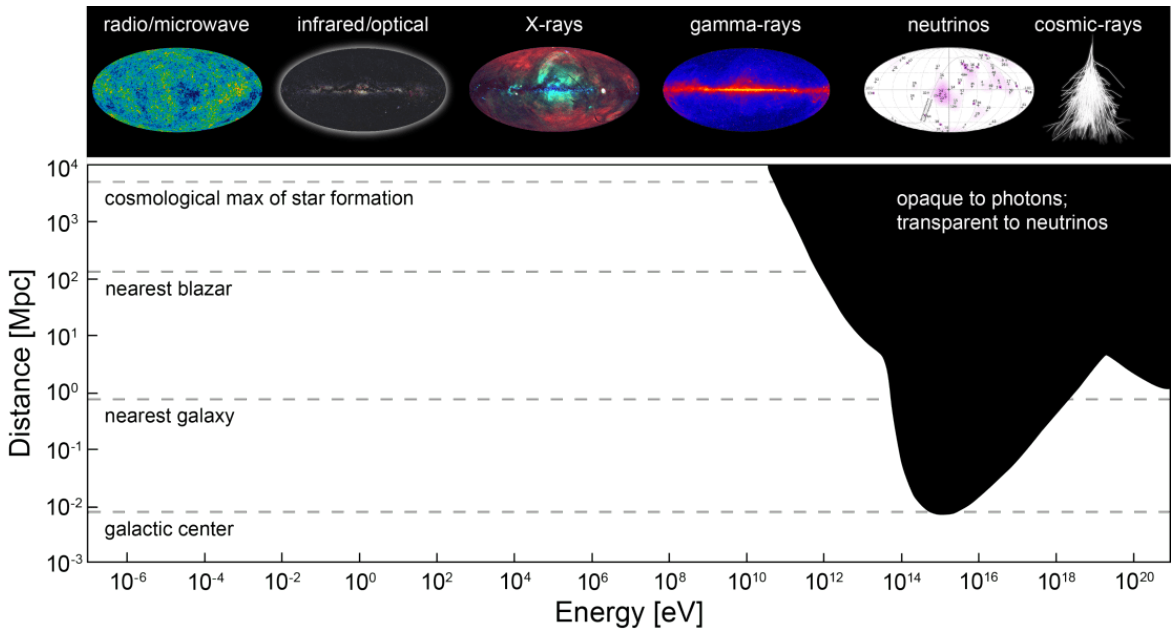

Figure 3.14: Visibility of transient events for different messengers. Figure taken from the IceCube website[19], which is based on Figure 2 in [23].

as they further decay:

$$\pi^+ \rightarrow \mu^+ + \nu_\mu \rightarrow \left(e^+ + \nu_e + \bar{\nu}_\mu\right) + \nu_\mu, \tag{3.21}$$

$$\pi^- \rightarrow \mu^- + \bar{\nu}_\mu \rightarrow \left(e^- + \bar{\nu}_e + \nu_\mu\right) + \bar{\nu}_\mu, \tag{3.22}$$

$$\pi^0 \rightarrow \gamma\,\gamma. \tag{3.23}$$

Modeling these processes requires the availability of photon fields, e.g. from the accretion disks, and matter distributions. Note that for hadronic models, the non-thermal nuclei, protons, and electrons produce similar signatures in sources. For details about leptonic continuum processes see e.g. [33, 151, 154].

Furthermore, photons from all astrophysical sources ranging across the electromagnetic spectrum comprise the Extragalactic Background Light (EBL) that interacts with high-energy particles during their source-to-Earth journey. Photon-photon absorption reduces the fraction of the particles escaping from the source region that eventually arrive at the observer. The effect is quantified by the optical depth τ_{EBL}, which predicts for $\tau_{\mathrm{EBL}} = 1$ a probability of $1/e$ with which a particle is not absorbed during propagation. Figure 3.14 visualizes this effect by shedding light on the observability of astrophysical sources in the multi-messenger approach with highlighting the drawback of distant sources being opaque to high-energy photons due to EBL and gamma-ray attenuation. In the propagation software CRPropa, work within this thesis contributed to the correct usage of various EBL models as well as user-specific photon fields with

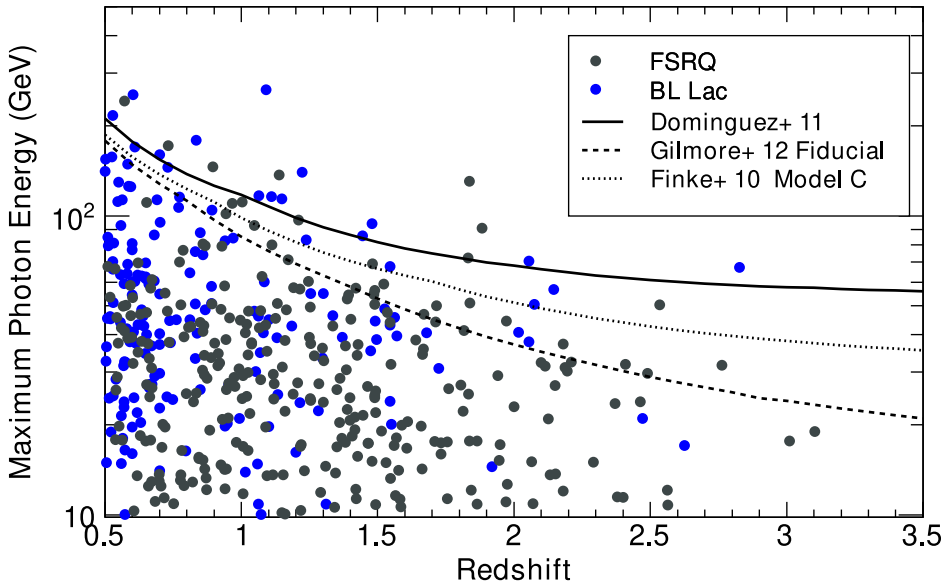

Figure 3.15: Maximum photon energy from astrophysical sources as a function of the redshift. The three curves indicate theoretical predictions of the photon energies from different models for the optical depth τ_{EBL} of 1. Taken from [13] with modifications of the plotting style.

two merged pull request[2021]. This contribution improves the study of the influence of the photon fields on the particles as they travel from sources to the Galaxy. Figure 3.15 shows the detailed prediction of τ_{EBL} for different theoretical models for the maximum photon energies as a function of the redshift of their sources. The dots show the observed photons from the Fermi 4LAC data with the highest energies from sources with the respective redshifts. These observations constrain the theoretical models. In the future, CTA will allow observations of photons from more distant sources than is possible with current ICTAs and will improve distinguishing between the models.

3.3 Summary

1. **Novel tool for the planning of follow-up campaigns**
   Tools commonly used for planning follow-up observations constitute a patchwork of disparate systems, data formats, communication techniques of relevant information, and alerts of transient phenomena. Astro-COLIBRI acts as a comprehensive platform accommodating the information transmitted through this ecosystem of real-time multi-messenger systems. The tool further automates the coordination of follow-up observations by providing bundled event information

[20] `https://github.com/CRPropa/CRPropa3/pull/366`
[21] `https://github.com/CRPropa/CRPropa3/pull/368`
[21] `https://icecube.wisc.edu/science/research/`

and linking detailed information through its graphical interface that is easily understandable for humans.

2. **Detection of most distant very-high energy AGN**
   The aspects discussed in the thesis are reconciled with detecting VHE signals from a distant ($z \approx 1$) AGN. The dynamical effects in the source region induced variability on timescales that allowed follow-up observations of H.E.S.S. based on an alert emitted by *Fermi*. Astro-COLIBRI has assisted in the coordination of follow-up observations by providing helpful information and offering mobile access, especially useful during the coordination over the weekends.

3. **Enhancing propagation routines to study real-time effects**
   Physical processes in transient sources provide a variety of highly complex phenomena with different timescales and temporal variations of multi-messenger signatures. Their understanding requires performing numerical simulations with realistic modeling of astronomical environments. Section 3.2 discusses these aspects, focusing on enhancements of the software tools CRPropa and PropPy in the scope of this thesis that include more efficient propagation routines. These improvements enable the efficient study of real-time effects in transient sources, whose findings offer input for the planning process of follow-up observation campaigns.

Chapter 4

Cosmic-Ray Transport in Astrophysical Sources

In this chapter, the transient sources introduced in Section 2.2 are investigated in detail. Emphasis is put on the transport- and interaction-induced temporal effects, which lead to characteristic multi-messenger observables. These effects shape the particle spectra and the light curves during flares. Section 4.1 addresses the running diffusion coefficients as statistical quantities that describe the transport behavior of the particles. The key properties of the diffusion coefficients, already introduced in Section 2.3.2, are revisited in the context of numerical simulations and compared with analytical descriptions. The fundamental statements about diffusion coefficients are largely based on the publication

- **P. Reichherzer***, J. Becker Tjus, E.G. Zweibel, L. Merten, and M.J. Pueschel, "Turbulence-level dependence of cosmic ray parallel diffusion", *Monthly Notices of the Royal Astronomical Society*, 498, 4, 2020 — doi:10.1093/mnras/staa2533.

The comparison between numerical simulations and theoretical descriptions of the running diffusion coefficients presented in Section 4.1 is based on studies conducted along the development of PropPy [138]. The following discussion benefits from the implementation of the Boris push as an improved and faster propagation code for CRPropa in the merge request[1]. This improvement allows more efficient propagation over large distances as discussed in the following. The work is mentioned in the proceeding [17] and will be discussed in more detail in the upcoming CRPropa 3.2 paper. The details are described in the following publications:

- **P. Reichherzer*** and J. Becker Tjus, "PropPy — Correlated random walk propagation of cosmic rays in magnetic turbulence", *Journal of Open Source Software*, 7, 74, 2022 — doi:10.21105/joss.04243,

[1] `https://github.com/CRPropa/CRPropa3/pull/222`

- R. Alves Batista, ..., **P. Reichherzer** et al., "CRPropa 3.2 — an advanced framework for high-energy particle propagation in extragalactic and galactic spaces", in preparation (2022).

The running diffusion coefficient shows the transition from ballistic to diffusive transport phase, which can be described through the telegraph equation. Section 4.2 explains this concept in more detail and illustrates its implications for transient sources at the example of blazar jets. This work is based on my contribution to the following article on the analytical theory that includes the development of an analytic expression for the propagation time needed until a diffusive description is feasible

- J. Becker Tjus, ..., **P. Reichherzer** et al., "Propagation of cosmic rays in plasmoids of AGN jets – implications for multimessenger predictions", *MDPI Physics*, 4, 2, 473-490, 2022 — doi:10.3390/physics4020032,

and ideas presented in the ICRC 2021 proceeding [144].

In the case of the diffusive behavior of charged particles in environments with an ordered background field, it is particularly worthwhile to study the different components of the diffusion tensor. Section 4.3 examines the relation between the diffusion coefficients perpendicular and parallel to the background field and explores their respective diffusion timescales. This study is discussed in more detail in the publication

- **P. Reichherzer***, J. Becker Tjus, E. G. Zweibel, L. Merten, and M. J. Pueschel, "Anisotropic cosmic-ray diffusion in isotropic Kolmogorov turbulence", *Monthly Notices of the Royal Astronomical Society*, 514, 2, 2022 — doi:10.1093/mnras/staa2533.

4.1 Running Diffusion Coefficients

The scalar diffusion coefficients introduced in Equation (2.9) shall be revisited here and evaluated analytically. This is accomplished by solving the telegraph-transport equation, which describes the particle transport in the ballistic as well as in the diffusive phase. Recall that the diffusive phase in this work is defined by a steady-state diffusion coefficient. The following calculation aims to provide an analytical expression that determines the temporal evolution of the running diffusion coefficient and thus allows statements about the particle transport at arbitrary times. The general telegraph Equation (3.4) in a turbulent plus an oriented magnetic field along the x_3-axis yields

$$\frac{\partial n}{\partial t} + \tau_{\mathrm{diff}} \cdot \frac{\partial^2 n}{\partial t^2} = \kappa_{\parallel} \frac{\partial^2 n}{\partial x_3^2} + \kappa_{\perp} \left(\frac{\partial^2 n}{\partial x_1^2} + \frac{\partial^2 n}{\partial x_2^2} \right) , \tag{4.1}$$

where the parallel diffusion coefficient $\kappa_{\parallel}$ describes the transport behavior along the ordered background field and $\kappa_{\perp}$ the behavior perpendicular to the x_3-axis.

Defining $\xi_1 \coloneqq x_1/\sqrt{\kappa_\perp}$, $\xi_2 \coloneqq x_2/\sqrt{\kappa_\perp}$, $\xi_3 \coloneqq x_3/\sqrt{\kappa_\parallel}$ and [174]

$$\nabla^2 \coloneqq \left(\frac{\partial^2}{\partial \xi_1^2} + \frac{\partial^2}{\partial \xi_2^2} + \frac{\partial^2}{\partial \xi_3^2} \right) , \tag{4.2}$$

yields

$$\frac{\partial n}{\partial t} + \tau_{\mathrm{diff}} \cdot \frac{\partial^2 n}{\partial t^2} = \nabla^2 n \, . \tag{4.3}$$

Furthermore, this equation can be converted into a Klein-Gordon-like equation

$$\left(\tau_{\mathrm{diff}} \cdot \frac{\partial^2}{\partial t^2} - \nabla^2 - \frac{1}{4\tau_{\mathrm{diff}}} \right) \eta = 0 \, , \tag{4.4}$$

if the definition of $\eta \coloneqq n \cdot \exp(t/(2\tau_{\mathrm{diff}}))$ is applied. The solution of the Klein-Gordon equation [124, 175] can be used to solve Equation (4.4) and derive n for a point source with $n(x, t = 0) = \delta(x - x_i)$ and $\xi = \sqrt{\xi_1^2 + \xi_2^2 + \xi_3^2}$ based on the expression:

$$\begin{aligned} n = \frac{e^{-t/2\tau_{\mathrm{diff}}}}{4\pi\kappa_\perp\sqrt{\kappa_\parallel}} \Bigg[& \delta\left(t - \xi\sqrt{\tau_{\mathrm{diff}}}\right) \cdot \xi^{-1} \cdot I_0 \left(\frac{1}{2} \sqrt{\frac{t^2}{\tau_{\mathrm{diff}}^2} - \frac{\xi^2}{\tau_{\mathrm{diff}}}} \right) \\ & + \Theta\left(t - \xi\sqrt{\tau_{\mathrm{diff}}}\right) \cdot \frac{1}{2\tau^{3/2}} \cdot \left(\frac{t^2}{\tau_{\mathrm{diff}}^2} - \frac{\xi^2}{\tau_{\mathrm{diff}}} \right)^{-1/2} \cdot I_1 \left(\frac{1}{2} \sqrt{\frac{t^2}{\tau_{\mathrm{diff}}^2} - \frac{\xi^2}{\tau_{\mathrm{diff}}}} \right) \Bigg] . \end{aligned} \tag{4.5}$$

Here, $\Theta(...)$ is the Heaviside step function and $I_\nu(...)$ is the modified Bessel function. The norm,

$$N = \int n \, \mathrm{d}^3 r = 1 - e^{-t/\tau_{\mathrm{diff}}} \, , \tag{4.6}$$

may be interpreted as the number of particles propagating diffusively [25]. According to this interpretation, no particles are diffusive at the beginning. With time, the number of diffusive particles increases exponentially until a steady-state value is reached. Pursuing this interpretation, the running diffusion coefficient $\kappa(t)$ is composed at time t of $N(t)$ particles that diffuse with properties governed by the steady-state diffusion coefficient κ and thus yields

$$\kappa(t) = N \cdot \kappa = \left(1 - e^{-t/\tau_{\mathrm{diff}}}\right) \cdot \kappa \, . \tag{4.7}$$

In contrast, the description of the transport via the diffusion equation yields a constant running diffusion coefficient $\kappa(t) = \kappa$ as the norm is constant

$$N_{\mathrm{diff.\,eq.}} = 4\pi \int_0^\infty \mathrm{d}r \, r^2 n_{\mathrm{diff}}(r) = 4\pi \int_0^\infty \mathrm{d}r \, \frac{r^2}{(4\pi t\kappa)^{3/2}} \exp\left(-\frac{r^2}{4\kappa t} \right) = 1 \, . \tag{4.8}$$

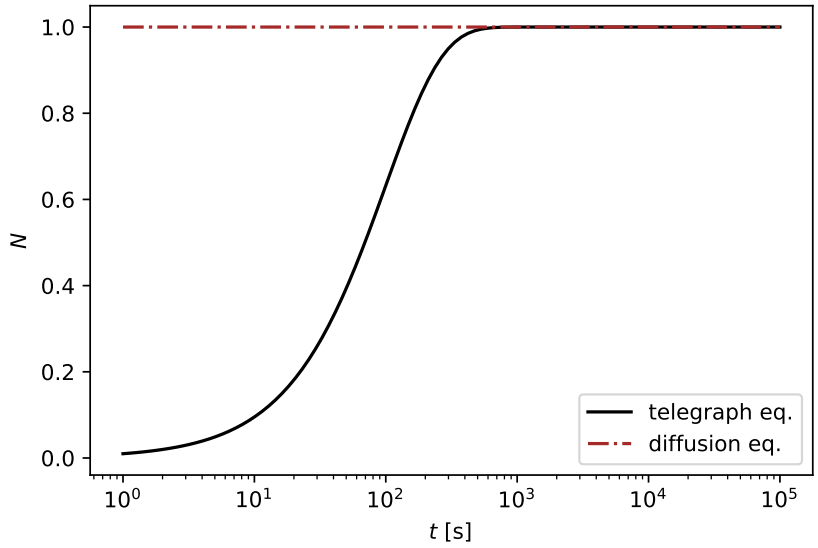

Figure 4.1: Comparison of the norms defined in Equations (4.6) and (4.8) as functions of time for the diffusion equation and the telegraph equation. The temporal evolution of the norm for the telegraph equation is given in Equation (4.6). If the transport is described via the diffusion equation, the constant norm is stated in Equation (4.8). Taken from Reichherzer et al. (2021, [144]).

Figure 4.1 compares the norm for the diffusion equation and the telegraph equation.

4.1.1 Ballistic Phase

The initial ballistic propagation phase is characterized by weakly-perturbed particle trajectories. Taking the limit of $t \ll \tau_{\mathrm{diff}}$ of Equation (4.7) yields

$$\kappa(t) = \kappa \cdot \frac{t}{\tau_{\mathrm{diff}}} \,. \tag{4.9}$$

The behavior for $t \lesssim \tau_{\mathrm{diff}}$ depends on whether there is an ordered background field adjacent to the turbulence.

Pure turbulence: Without an ordered magnetic field, charged particles move on weakly-perturbed rectilinear trajectories. The running diffusion coefficients follow approximately the description of Equation (4.9) until its transition towards the diffusive phase at $t \approx \tau_{\mathrm{diff}}$.

Turbulence plus ordered magnetic field: With a directed background field, particles move along weakly-perturbed helical paths. The diffusion coefficient component

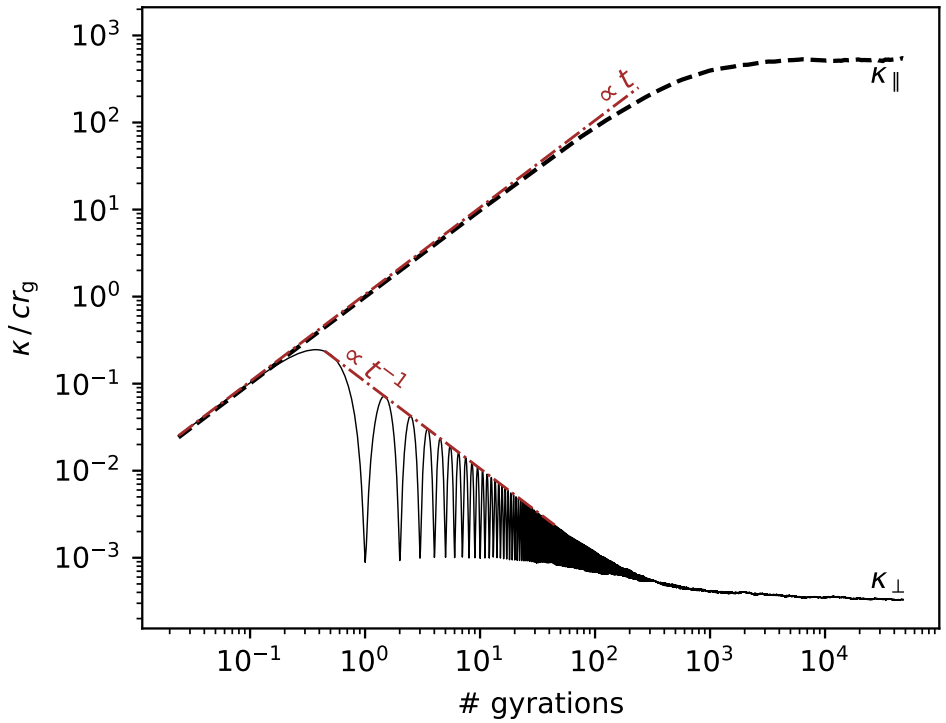

Figure 4.2: Normalized running diffusion coefficient as a function of the number of gyration radii, which scale linearly with time due to constant particle speeds. The scaling with t and t^{-1} during the ballistic phase are illustrated for the parallel and perpendicular components, respectively. Simulated with CRpropa 3.1.7 using the numerical setup described in [140].

$\kappa_\parallel$ along the background field scales linearly with time and thus has a comparable behavior as without an ordered background field:

$$\kappa_\parallel(t) = \kappa_\parallel \cdot \frac{t}{\tau_{\mathrm{diff}}} \,. \tag{4.10}$$

The movement in a plane perpendicular to the background magnetic field is dominated by the constant gyromotion with radius r_g. After each gyration, charged particles return to their origin, with minor deviations caused by deflections in the turbulent magnetic field. This behavior causes local minima in the running perpendicular diffusion coefficients $\kappa_\perp(t)$. This behavior is superimposed by the $\kappa_\perp(t) \propto t^{-1}$ scaling dictated by the distance $\Delta x_\perp$ oscillating in the range of $-r_\mathrm{g}$ and $+r_\mathrm{g}$. For $t \gg r_\mathrm{g}/c$ and $t \lesssim \tau_{\mathrm{diff}}$, the local maxima of $\kappa_\perp(t)$ scale as

$$\kappa_{\mathrm{local\,max},\perp}(t) = \frac{\langle \Delta x_\perp^2 \rangle}{2t} \propto t^{-1} \,. \tag{4.11}$$

This behavior is illustrated in Figure 4.2.

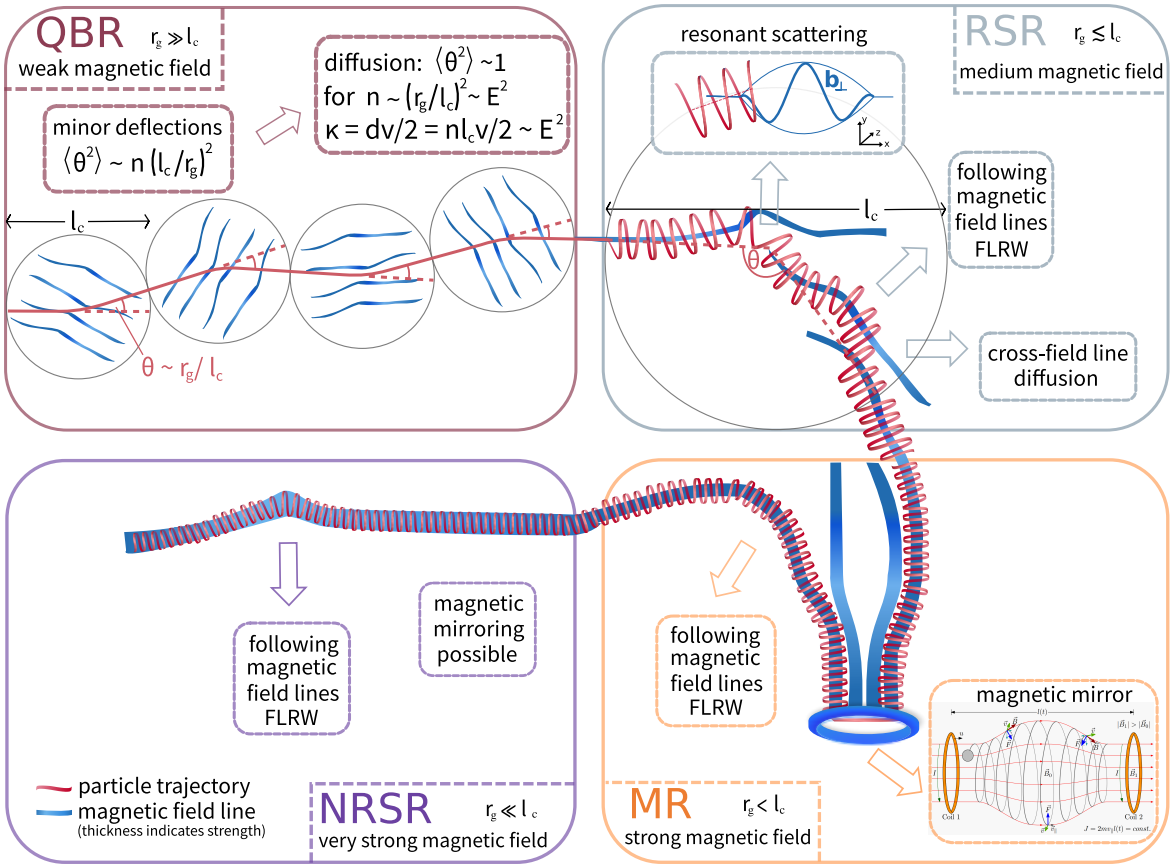

Figure 4.3: Schematic representation of the different transport regimes of charged particles in static magnetic fields with a turbulent component. An exemplary trajectory of a charged particle (red line) along magnetic fields (blue lines) visualizes typical effects contributing to a diffusive propagation behavior. Figure taken from [145] with modifications in the QBR, where the schematic representation from [97] is applied.

4.1.2 Steady-State Phase

The previous section demonstrated analytically and numerically that the transport behavior transitions from the initial ballistic to the final steady-state phase. In the current section, the focus lies on the steady-state phase. First, the aspects that affect the steady-state diffusion coefficient are described. As a general principle, the transport has to be divided into different regimes, which arise analytically based on the relation between the particle gyration radius and the correlation length of the turbulence (see [140] for the derivations). Figure 4.3 shows the different regimes in a schematic visualization of a particle trajectory (in red) in different astrophysical environments, which are characterized by the blue magnetic field line. The field-line thickness indicates the magnetic field strength. This, together with the particle energy, influences the size of the illustrated gyroradii. The regimes shown in Figure 4.3 are described in clockwise sequence, starting with the QBR regime:

Quasi-ballistic regime (QBR): This regime is characterized by large gyration motions of the charged particles that span multiple correlation lengths l_c of the turbulence $l_c \lesssim r_g$. The effects of the comparatively small turbulence scales are largely averaged out. However, particles still experience small deflections due to the turbulence that lead to a steady-state diffusion behavior after a long time. This can be understood by employing a coherence-cell concept introduced by [97], where one effective small-angle deflection appears in each cell (see schematic visualization in Figure 4.3). The average deflection angle after n scatterings is given by [172]

$$\langle \Theta^2 \rangle \approx n \left(\frac{l_c}{r_g} \right)^2 . \tag{4.12}$$

Diffusive behavior occurs as soon as $\langle \Theta^2 \rangle \approx 1$ applies, which requires $n = (r_g/l_c)^2$ scatterings. Assuming one deflection on average in each correlated turbulence volume interval, particles travel on quasi-rectilinear trajectories a distance $d = n \cdot l_c = r_g^2/l_c$ until they become diffusive. At this point, the diffusion coefficient reaches approximately the final value

$$\kappa = \frac{\langle (\Delta x)^2 \rangle}{2t} = \frac{d^2}{2d/v} = \frac{r_g^2 v}{2l_c}. \tag{4.13}$$

Therefore, these steady-state diffusion coefficients in QBR scale quadratically with the gyroradius and thus as $\kappa \propto E^2$ for fixed correlation lengths and magnetic-field strengths. It is important to mention that the perpendicular component, on the other hand, is energy independent in the QBR for low turbulence levels, as shown in [139]. The energy-independent perpendicular diffusion is caused by particles following field lines because of their large diffusion timescales.

High-energy charged particles in the intergalactic magnetic field (IGMF) or transient sources are within the QBR, as they fulfill $l_c \lesssim r_g$. While the gyroradii are large due to the weak magnetic field strength in the IGMF, the correlation lengths are small in transient sources.

Resonant-scattering regime (RSR): As soon as the gyroradii become smaller than the correlation length of the turbulence, charged particles resonantly scatter off the turbulence fluctuations. As shown in Figure 4.3, there are further effects that lead to a diffusive behavior and modify the diffusion coefficients. The RSR is constrained to the range $l_{\min} B_0/(l_c \pi \delta B) \lesssim r_g/l_c \lesssim 5/(2\pi)$. The parallel diffusion coefficient scales in the limit of low turbulence levels $\delta B \ll B_0$ as [140]

$$\kappa_\parallel = v l_c \left(\frac{r_g}{l_c} \right)^{1/3} \left(\frac{B_0}{\delta B} \right)^2 \propto E^{1/3}, \tag{4.14}$$

according to the quasi-linear theory (QLT). The isotropic components scale for high turbulence levels $\delta B \gg B_0$, which is reffered to as the Bohm limit [27]

$$\kappa = \frac{r_\mathrm{g} v}{3} \propto E\,. \tag{4.15}$$

Between both turbulence-level limits, a transition occurs, which is discussed in detail in [140]. Diffusion coefficients in the RSR and the QBR are shown in Figure 4.4 as functions of $r_\mathrm{g}/l_\mathrm{c}$ for different turbulence levels. The energy scaling yields approximately $\kappa_\parallel \propto E^2$ and $\kappa_\perp \propto E^0$ in the QBR. In the RSR, the expected transition from Bohm-diffusion scaling towards QLT predictions is observable, while the latter scaling of $\kappa_\parallel \propto E^{1/3}$ is not yet reached. Details are described in [140] and [145]. Note that in many astrophysical environments (e.g., galaxies [91, 96, 162]), similar orders of magnitude of δB and B_0 are present at the injection scales of the turbulence. The ratio $\delta B/B_0$ decreases according to Kolmogorov- or Kraichnan-like turbulence for smaller fluctuations with whom lower-energy particles resonantly scatter. The fluctuation levels labeled in Figure 4.4 are thus the global quantities.

In astrophysical scenarios, the RSR extends over many orders of magnitude of the particle energy, since typically $l_\mathrm{min} \ll l_\mathrm{c}$ holds. In contrast, this regime is limited to only a narrow range and a few orders of magnitude in energy of charged particles in numerical simulations. In grid-based turbulence methods, this is due to current computers' limited available RAM and the plane-wave summation approach due to the high runtime costs that a large fluctuation range entails.

Mirror regime (MR): The mirror regime is a bridging regime between the RSR and the non-resonant-scattering regime (NRSR). It is characterized by the decreasing fraction of particles that can resonantly scatter for decreasing particle energy. The energy that marks its minimum defines the transition to the NRSR. Equally, however, the effects of magnetic mirrors in which particles change direction are increasing for decreasing particle energies. The influence of magnetic mirrors is schematically shown in Figure 4.3. This influence of magnetic mirrors and the limited resonant scattering result in a complex energy dependence of the diffusion coefficients, whose details are the subject of current research. The MR extends over $l_\mathrm{min}/(2\pi l_\mathrm{c}) \lesssim r_\mathrm{g}/l_\mathrm{c} \lesssim l_\mathrm{min} B_0/(l_\mathrm{c}\pi\delta B)$ with negligible effects on high-energy CRs with $r_\mathrm{g} \gg l_\mathrm{min}$ relevant for the multi-messenger signatures discussed in the present thesis.

Non-resonant-scattering regime (NRSR): In this regime, there is no resonant scattering. Particles follow the field lines and are trapped and reflected in magnetic mirrors. The regime extends over $r_\mathrm{g}/l_\mathrm{c} \lesssim l_\mathrm{min}/(2\pi l_\mathrm{c})$. As in MR, the influence of propagating CRs on turbulence is relevant due to generation by fluctuations in, e.g., streaming instabilities. These effects can no longer be investigated with the test particle approach on which the numerical calculations of this work are based.

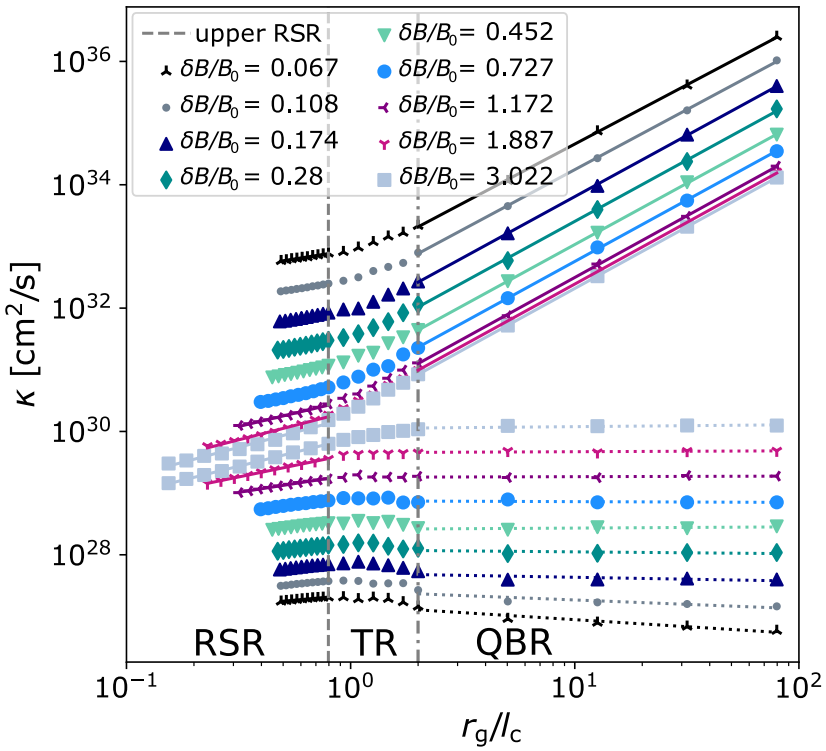

Figure 4.4: Parallel (top points and solid fits) and perpendicular (bottom points and dotted fits) diffusion coefficients as a function of r_g/l_c for different turbulence levels. Simulations are limited to the RSR with $r_g/l_c \gtrsim l_{min}B_0/(l_c\pi\delta B)$ and the QBR with $r_g/l_c \gtrsim 5/(2\pi)$. Note the transition regime (TR) that shifts the QBR towards larger values of r_g/l_c. The simulation were performed with CRPropa 3.1 as described in [145] with $l_c = 17.8$ pc, $l_{min} = 1.7$ pc, $l_{max} = 82.45$ pc, $s = 0.85$ pc, $N_{grid} = 1024$. Each data point is the mean of 20-50 diffusion coefficients, each simulated with the same parameters but with a different realization of the turbulent magnetic field. Figure taken from Reichherzer et al. (2022, [145]).

4.1.3 Running Diffusion Coefficients in AGN Jet Plasmoids

The analytical considerations on the running diffusion coefficient $\kappa(t)$ of the previous subsections are now evaluated for the example of flares of AGNs. For this purpose, the model of a relativistic plasmoid moving along the jet axis, as discussed in the literature to explain flares [25, 86], is studied. Due to the focus on the transport properties of this thesis, the acceleration mechanisms of the high-energy particles will only be considered by means of an appropriate initial condition of the investigation of the transport phase. Accordingly, particles start as a homogeneous distribution in the plasmoid. Figure 4.5 schematically presents the plasmoid model used here. In the following, the transport of highly relativistic CRs $v \approx c$ in the plasmoid-rest frame is described.

The most energetic charged particles that play a role in this model are located in

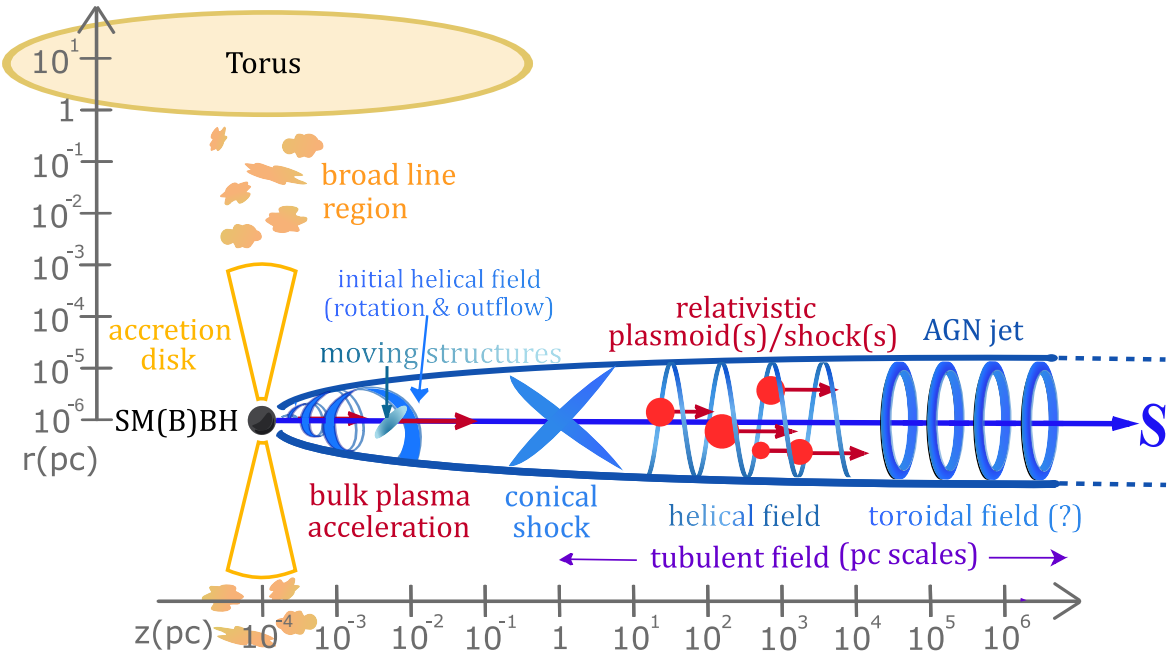

Figure 4.5: Schematic representation of an AGN consisting of a central black hole aspirating matter from the accretion disk. The symmetric jets (here one is omitted for saving space) accelerate plasmoids, which move with relativistic speeds along the jet through different magnetic field structures and emit particles thereby. Taken from [25].

the QBR, since $r_\mathrm{g} > l_\mathrm{c}$ holds, as typical correlation lengths range between $10^{10}\,\mathrm{m}$ and $10^{13}\,\mathrm{m}$, while for isotropic turbulence the gyroradius yields

$$r_\mathrm{g} = \frac{E}{q\,c\,B} \approx 3.34 \cdot 10^{12}\,\mathrm{m} \left(\frac{E}{100\,\mathrm{PeV}}\right) \left(\frac{B}{1\,\mathrm{G}}\right)^{-1}, \tag{4.16}$$

where B defines the total magentic field.

Note that for the highly relativistic particles considered throughout the thesis $v \approx c$ holds and is applied subsequently. The diffusion coefficient can be computed for the parameters given in Table 4.1 according to Equation (4.13):

$$\kappa_\mathrm{theory} = \frac{r_\mathrm{g}^2 \cdot c}{l_\mathrm{c}} \approx 3.34 \cdot 10^{22}\,\frac{\mathrm{m}^2}{\mathrm{s}} \left(\frac{E}{100\,\mathrm{PeV}}\right)^2 \cdot \left(\frac{B}{1\,\mathrm{G}}\right)^{-2} \cdot \left(\frac{l_\mathrm{c}}{10^{11}\,\mathrm{m}}\right)^{-1}. \tag{4.17}$$

This diffusion coefficient can be plugged in Equation (4.7) and results in the running diffusion coefficent

$$\kappa_\mathrm{theory}(t) \approx 3.34 \cdot 10^{22}\,\frac{\mathrm{m}^2}{\mathrm{s}} \left(1 - e^{-\frac{t}{\tau_\mathrm{diff}}}\right) \left(\frac{E}{100\,\mathrm{PeV}}\right)^2 \left(\frac{B}{1\,\mathrm{G}}\right)^{-2} \left(\frac{l_\mathrm{c}}{10^{11}\,\mathrm{m}}\right)^{-1}. \tag{4.18}$$

Table 4.1: Parameters of the plasmoid model used in Section 4.1.3.

parameters	values
turbulence model	isotropic 3D Kolmogorov
trubulent magnetic field strength	$\delta B = 1\,\mathrm{G}$
correlation length	$l_\mathrm{c} = 10^{11}\,\mathrm{m}$

Numerical simulations that compare with this analytical prediction are described below. Five different simulation setups are compared, composed of the two possible routines for magnetic turbulence generation (see Section 3.2.1) and the different propagation algorithms discussed in Section 3.2.2. The simulations use the parameters from Table 4.1. In all numerical simulations, 10^3 charged test particles are emitted isotropically from a point source. The grid-based turbulence approach uses 1024^3 grid points, while the PW-turbulence approach uses 10^3 modes, which is sufficient according to studies presented in [153].

The simulations and the presented results can be reproduced via the simulation and analysis scripts provided in the comparison folder of PropPy 1.0.0 [142]. Furthermore, the simulation results are publicly accessible [147].

Particles become diffusive at trajectory lengths of about mean-free paths

$$\lambda_\mathrm{theory} = \frac{3\kappa_\mathrm{theory}}{c} \approx 3.34 \cdot 10^{14}\,\mathrm{m} \left(\frac{E}{100\,\mathrm{PeV}}\right)^2 \cdot \left(\frac{B}{1\,\mathrm{G}}\right)^{-2} \cdot \left(\frac{l_\mathrm{c}}{10^{11}\,\mathrm{m}}\right)^{-1} . \quad (4.19)$$

In the last step, the diffusion coefficient from Equation 4.17 is inserted. In order to observe a converged running diffusion coefficient, the simulations are stopped after trajectory lengths of 10^{17} m, which is much larger than $\lambda_\mathrm{theory} = \tau_\mathrm{diff}\, c$ and therefore deemed sufficient for a steady-state transport phase.

Figure 4.6 shows a comparison of the simulation results for the calculated running diffusion coefficients for the different methods of particle propagation and turbulence generation. The simulation results are compared to the analytical running diffusion coefficient from Equation 4.18. The lower panel shows the absolute value of the deviation of the simulation results from the theoretical prediction in percent. Furthermore, the analytically derived steady-state diffusion coefficient presented in Equation (4.17) is tested numerically by averaging over 20 seeds of the same simulation with the Boris-Push (BP) method and the *plane-wave* (PW) *turbulence* method with $s_\mathrm{step} = 10^{10}\,\mathrm{m}$, which gives $\kappa_\mathrm{sim} = (3.41 \pm 0.16) \cdot 10^{22}\,\mathrm{m}^2/\mathrm{s}$.

Figure 4.7 shows a comparison of the diffusion coefficients at different trajectory lengths. The left and right panels differ only in the simulation length. In the left panel, only trajectories up to $10^{14}\,\mathrm{m}$ are considered, whereas, in the right panel, trajectories up to $10^{17}\,\mathrm{m}$ are displayed. Since the mean-free paths indicate the transition between ballistic to diffusive propagation, the left panel shows ballistic particle propagation and the right panel diffusive propagation. The top panel shows the effective diffusion

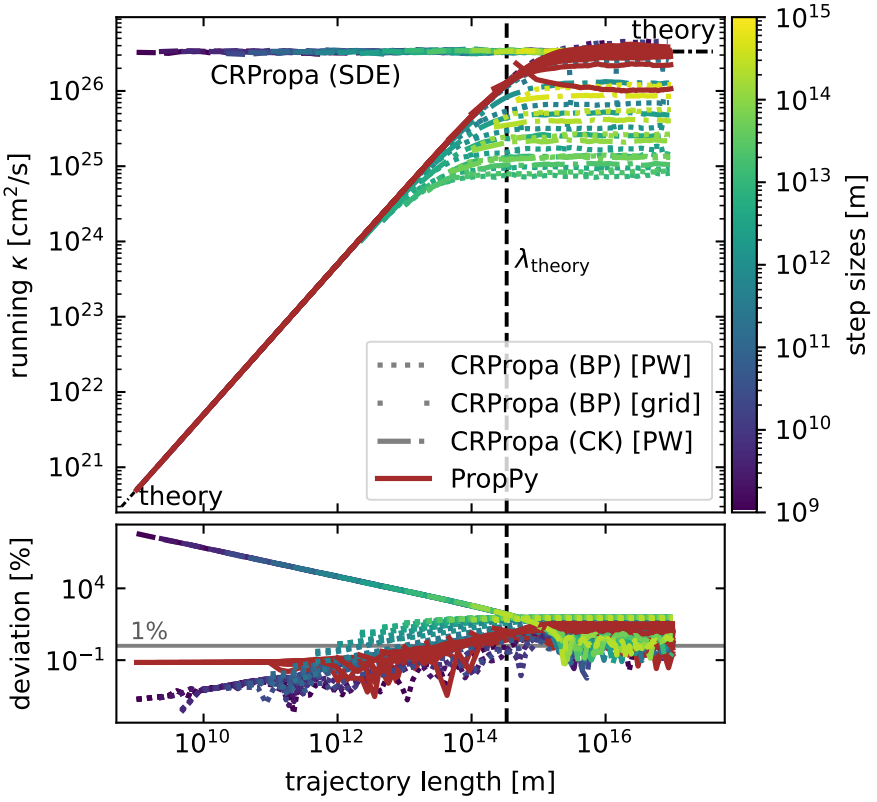

Figure 4.6: Comparison between different propagation approaches for the computation of running diffusion coefficients. 10^3 protons with $E = 100\,\text{PeV}$ simulated with parameters defined in Table 4.1. The theory expectation for the running diffusion coefficient is computed via Equation (4.18) and displayed in the upper panel (it is mostly covered by the numerical simulation results). Absolute values of the deviations from this prediction are shown in the lower plot.

coefficient at $10^{14}\,\text{m}$ on the left and the converged diffusion coefficient on the right since the running diffusion coefficient remains approximately constant beginning at the diffusive limit, as can be seen in Figure 4.6. The lower panel shows the required processor time of the simulation as a function of the step size. The same processor was used for all simulations for better comparability.

The comparisons yield the following results:

- The EoM-based propagation approaches BP and CK, as well as the correlated random walk (CRW) method from PropPy can correctly model the initial ballistic transport phase. The diffusive approach (SDE) cannot describe this initial ballistic phase by construction since it always assumes diffusive particle transport.

- The diffusive and CRW approaches can use relatively large step sizes to model the correct statistical behavior. The latter only needs to resolve the mean-free paths sufficiently well, which is guaranteed if the step size is at least ten times smaller

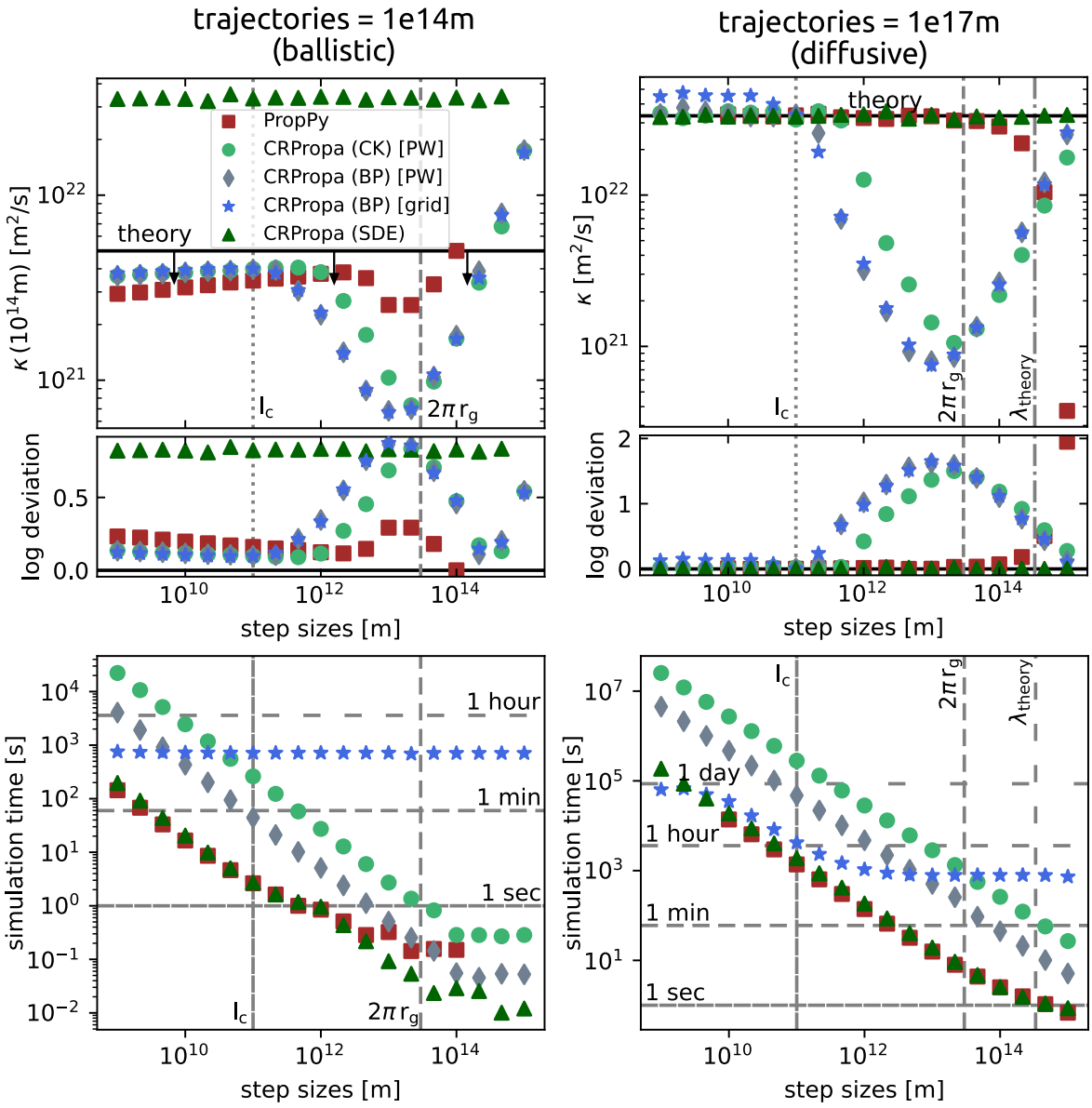

Figure 4.7: Comparison between different propagation approaches for the computation of running diffusion coefficients. 10^3 protons with $E = 100$ PeV simulated with parameters defined in Table 4.1. *Left panel* shows the ballistic propagation regime at the beginning of particle trajectories ($\approx 10^{14}$ m), where only one fourth of the particles are already diffusive according to Equation (4.6). *Right panel* shows also long trajectory lengths, for which all particles are diffusive ($\gg \lambda$). *Upper panel:* diffusion coefficients at 10^{14} m (left) and converged ones (right) as functions of different step sizes of the propagation methods. Log deviation is defined as $|\log(\kappa_{\mathrm{sim}}) - \log(\kappa_{\mathrm{theory}})|$. *Lower panel:* Simulation time per processor as functions of step sizes. Color-coded with the deviation from theoretical predictions. Usage of 260 threads for step sizes smaller than 10^{13} m. Note that the theory prediction is $\kappa_{\mathrm{theo}} = 3.34 \cdot 10^{22}\,\mathrm{m}^2/\mathrm{s}$. Averaging over 20 seeds of the same simulation with BP and PW with $s_{\mathrm{step}} = 10^{10}$ m gives $\kappa_{\mathrm{sim}} = (3.41 \pm 0.16) \cdot 10^{22}\,\mathrm{m}^2/\mathrm{s}$.

than the mean-free path. In the case of the EoM-based methods, step sizes must be small enough to resolve both the gyration motion and the scales of turbulence sufficiently well. This limitation can be seen as the diffusion coefficients in the middle right panel converge to a constant value only when the step sizes are smaller than the gyration radii and smaller than the correlation length of the turbulence.

- Smaller simulation times for given step sizes combined with the fewer step size requirements translate into a significant increase in speed for the diffusive method and the CRW method compared to the EoM-based methods.

4.2 Diffusive or Ballistic Transport?

The previous section demonstrates analytically and numerically that the transport behavior of CRs transitions from the initial weakly-perturbed (ballistic) propagation phase to the diffusive propagation phase that is defined by a steady-state diffusion coefficient. Both transport phases have fundamentally different properties that lead to significant differences in observable signatures:

1. **Particle spectrum:** Whereas an energy-dependent diffusion coefficient changes the spectrum of diffusive particles, as shown by the leaky-box model in Section 2.3.2,

$$n_{\mathrm{diff}}(E) \propto (\kappa(E))^{-1} \cdot S(E) \propto E^{-\delta-\alpha}\,, \tag{4.20}$$

the spectrum for ballistic transport remains unchanged

$$n_{\mathrm{ball}}(E) \propto S(E) \propto E^{\alpha}\,. \tag{4.21}$$

2. **Escape times:** For isotropically diffusing particles, the diffusion coefficient yields $\kappa(t) = \langle \Delta x^2 + \Delta y^2 + \Delta z^2 \rangle / 2t$. Particles travel in average an escape distance d_{esc} to reach the source surface. The above expression for the diffusion coefficient yields $\kappa(t_0) = d_{\mathrm{esc}}^2 / 2\tau_{\mathrm{esc,\,diff,all}}$. Note that in the description of diffusion coefficients, particles can diffuse several times to a distance d_{esc}, e.g. one particle can contribute several times at t_0, t_1, and t_i to the diffusion coefficient at the distance d_{esc}. In astrophysical sources, particles have, however, a vanishing probability to return back into the source region once escaping from it. Therefore, $\tau_{\mathrm{esc,\,diff}} = t_0 < \tau_{\mathrm{esc,\,diff,all}}$ holds, which yields, with the above expression for diffusion coefficients, an upper limit for escape timescales

$$\tau_{\mathrm{esc,\,diff}} \lesssim \frac{\langle d^2 \rangle}{2\kappa} \coloneqq \frac{d_{\mathrm{esc}}^2}{2\kappa}\,. \tag{4.22}$$

The equality describes the unrealistic case, where magnetic-field conditions are equal within and outside of the source region, hence allowing particles to return back into the source. Heuristically argued, the diffusion coefficient is effectively increased by suppressing scattering outside the source region.

For the ballistic transport phase, the escape times are independent of the diffusion coefficients and only depend on the escape distance

$$\tau_{\mathrm{esc,\,ball}} = \frac{d_{\mathrm{esc}}}{c}\,. \tag{4.23}$$

These significant differences require knowledge of whether the transport of charged particles in particular environments must be considered ballistic or diffusive. This applies equally to analytical predictions, numerical simulations, and analyses and interpretations of observational data.

The transition from the ballistic to the diffusive phase is investigated in the following so that statements about the propagation behavior of particles in astrophysical systems are possible. Here, the relevant question is whether particles have already become diffusive when escaping the source region. Rearranging Equation (4.6) yields an expression for the time t_N needed to have the fraction N normalized to one of the particles propagating diffusivly

$$t_N = -\ln(1-N)\,\tau_{\mathrm{diff}} = \frac{-\ln(1-N)}{c}\,\lambda_{\parallel} = \frac{-3\ln(1-N)}{c^2}\,\kappa_{\parallel}. \tag{4.24}$$

In the last steps, the connections between τ_{diff}, $\lambda_{\parallel}$, and $\kappa_{\parallel}$ according to Equation (3.8) are employed. For isotropic trubulence without an ordered magnetic field, it yields

$$t_N = \frac{-\ln(1-N)}{c^2}\,\kappa. \tag{4.25}$$

Equation (4.24) reveals by employing $t_N = \tau_{\mathrm{diff}}$ that the diffusion timescale indicates the time after which a fraction,

$$N = 1 - \exp(-1) \approx 0.63\,, \tag{4.26}$$

of the particles is diffusive. The diffusion timescale is thus suitable for indicating the transition from the ballistic to the diffusive phase and will be used for this purpose throughout the thesis.

Consequently, only if the escape times of charged particles from an astrophysical environment are larger than the diffusion timescales, a diffusive description is feasible $\tau_{\mathrm{esc}} \gtrsim \tau_{\mathrm{diff}}$. For the sake of generality, the criterion for an arbitrary fraction of diffusion particles N is chosen as the condition for defining the validity of the diffusive particle

description

$$\tau_{\mathrm{esc}} \gtrsim t_N = -\ln(1-N)\,\tau_{\mathrm{diff}}\,. \tag{4.27}$$

If N gets close to 100 %, most particles are diffusive and the expression for the escape times $\tau_{\mathrm{esc,\,diff}}$ from Equation (4.22) holds. Inserting this equation, together with the diffusion timescale from Equation (3.8) for diffusive particles, in the condition from Equation (4.27) yields

$$\frac{d_{\mathrm{esc}}^2}{2\kappa} \gtrsim -\ln(1-N)\,\frac{3\kappa}{c^2}\,. \tag{4.28}$$

Rearranging this condition results in a condition for the diffusion coefficient that has to be fulfilled in order to treat particles diffusively

$$\frac{d_{\mathrm{esc}}\,c}{\sqrt{-6\ln(1-N)}} \gtrsim \kappa = \begin{cases} c\,l_{\mathrm{c}}\left(\frac{r_{\mathrm{g}}}{l_{\mathrm{c}}}\right)^{1/3}\left(\frac{B_0}{\delta B}\right)^2 & \mathrm{RSR}: r_{\mathrm{g}} \lesssim 5l_{\mathrm{c}}/2\pi;\ \mathrm{QLT}: \delta B \ll B_0 \\ c\,r_{\mathrm{g}}/3 & \mathrm{RSR}: r_{\mathrm{g}} \lesssim 5l_{\mathrm{c}}/2\pi;\ \mathrm{Bohm}: \delta B \gg B_0 \\ c\,r_{\mathrm{g}}^2/(2l_{\mathrm{c}}) & \mathrm{QBR}: r_{\mathrm{g}} \gg 5l_{\mathrm{c}}/2\pi \end{cases}. \tag{4.29}$$

Here, the diffusion coefficient are described according to Equations (4.14), (4.15), and (4.13) for the QLT- and the Bohm-limit, and the QBR prediction, respectively. Note that for the QLT-limit, the expression for the parallel diffusion coefficient is used, which is larger than the perpendicular component. In source geometries where the perpendicular escape distance is much smaller than that along the ordered field $d_{\mathrm{esc},\perp} \ll d_{\mathrm{esc},\parallel}$, the expression for the perpendicular diffusion coefficient may need to be used instead. The condition for the diffusion coefficient can be converted into a condition for the correlation length or size of the source system, as well as the gyroradii of the particles. The latter option is especially useful to make statements for which gyroradii or energies particles can be treated diffusively in certain sources:

$$r_{\mathrm{g}} \lesssim \begin{cases} \frac{d_{\mathrm{esc}}^3\,l_{\mathrm{c}}^{-2}}{(-6\ln(1-N))^{3/2}}\left(\frac{\delta B}{B_0}\right)^6 & \mathrm{RSR}: r_{\mathrm{g}} \lesssim 5l_{\mathrm{c}}/2\pi;\ \mathrm{QLT}: \delta B \ll B_0 \\ \frac{d_{\mathrm{esc}}}{\sqrt{-2\ln(1-N)/3}} & \mathrm{RSR}: r_{\mathrm{g}} \lesssim 5l_{\mathrm{c}}/2\pi;\ \mathrm{Bohm}: \delta B \gg B_0 \\ \frac{\sqrt{d_{\mathrm{esc}}\,l_{\mathrm{c}}}}{\sqrt[4]{-3\ln(1-N)/2}} & \mathrm{QBR}: r_{\mathrm{g}} \gg 5l_{\mathrm{c}}/2\pi \end{cases}. \tag{4.30}$$

The only applied requirement for N is that when escaping, most particles have to be diffusive. As discussed above, an intuitive approach is $N = 0.63$, for which the condition from Equation (4.27) yields

$$\tau_{\mathrm{esc}} \gtrsim \tau_{\mathrm{diff}}\,. \tag{4.31}$$

This choice results in

$$r_\mathrm{g} \lesssim \begin{cases} 6^{-3/2}\, d_\mathrm{esc}^3\, l_\mathrm{c}^{-2} \left(\frac{\delta B}{B_0}\right)^6 & \mathrm{RSR} : r_\mathrm{g} \lesssim 5l_\mathrm{c}/2\pi;\ \mathrm{QLT} : \delta B \ll B_0 \\ \sqrt{3}\, d_\mathrm{esc}/\sqrt{2} & \mathrm{RSR} : r_\mathrm{g} \lesssim 5l_\mathrm{c}/2\pi;\ \mathrm{Bohm} : \delta B \gg B_0 \\ \sqrt{d_\mathrm{esc}\, l_\mathrm{c}} & \mathrm{QBR} : r_\mathrm{g} \gg 5l_\mathrm{c}/2\pi \end{cases} . \tag{4.32}$$

Here, the approximation $(2/3)^{1/4} \approx 1$ was applied for the QRB case. If gyroradii fulfill this condition, their transport can be treated diffusively. Note that the influence of large N on the final result is small and, for example, for the conservative case $N = 0.99999$ yields in the QBR the condition $r_\mathrm{g} \lesssim \sqrt{d_\mathrm{esc}\, l_\mathrm{c}}/2$, which differs only by a factor of 2 with respect to the ansatz proposed in Equation (4.31). Due to the robustness of the result with respect to the choice of N, Equation (4.32) shall be used in the following as a realistically motivated condition for the validity of the diffusion approach.

Pure isotropic turbulence ($\delta B \gg B_0$): For isotropic turbulence without an ordered background field B_0, Equation (4.32) simplifies to

$$r_\mathrm{g} \lesssim \begin{cases} \sqrt{3}\, d_\mathrm{esc}/\sqrt{2} & \mathrm{RSR} : r_\mathrm{g} \lesssim 5l_\mathrm{c}/2\pi \\ \sqrt{d_\mathrm{esc}\, l_\mathrm{c}} & \mathrm{QBR} : r_\mathrm{g} \gg 5l_\mathrm{c}/2\pi \end{cases} . \tag{4.33}$$

By visualizing this condition, fundamental insights can be illustrated. For this purpose, the condition from Equation (4.32) for the case of isotropic turbulence without an ordered background field is illustrated in Figure 4.8. This figure illustrates the parameter space for which charged particles in spherical plasmoids with correlation lengths of $10^{11}\,\mathrm{m}$ of the turbulence can be described diffusively (dotted area). The individual features of this figure that contribute to this statement are listed below:

- x-axis: The x-axis labels show the escape distance d_esc of particles in the plasmoid, which scales linearly with its spatial extension for fixed initial particle distributions. For spherical plasmoid with radius R, $d_\mathrm{esc} = R$ holds for particles that start in the plamsoid center.
- y-axis: The y-axis labels show the particle gyroradii as well as the energy for a fixed magnetic field $\delta B \approx 1\,\mathrm{G}$.
- l_max: The maximum fluctuations of the turbulence. For Kolmogorov turbulence $l_\mathrm{max} \approx 5l_\mathrm{c}$ holds.
- $5l_\mathrm{c}/2\pi$: This horizontal line marks the transition between RSR and QBR.
- black line: The black line visualizes the maximum gyroradii for which the condition from Equation (4.32) holds. The solid line visualizes the QBR prediction and the dot-dashed line the Bohm diffusion in RSR.

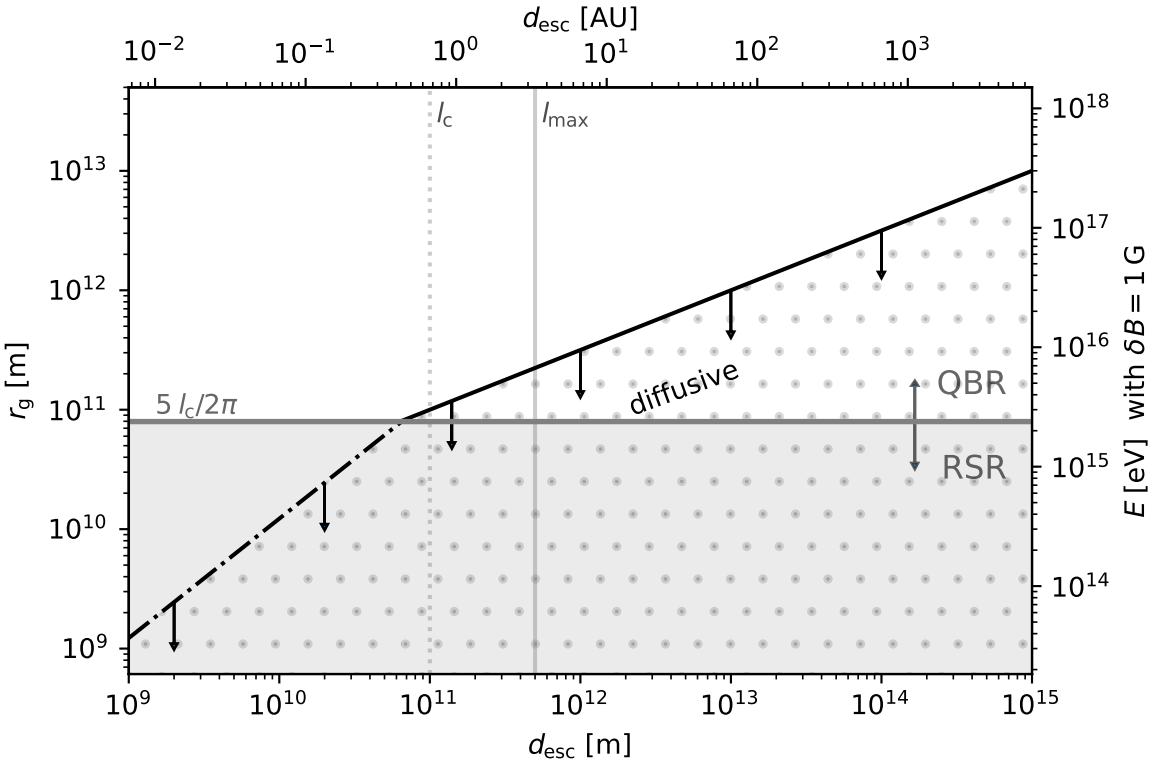

Figure 4.8: Visualization of the criterion from Equation (4.32) for determining the validity of a diffusive particle description as a function of system sizes (proportional to escape distances d_{esc}) and particle energies. Particles below the black line can be considered diffusive in the corresponding systems. The dotted area indicates this region. where in addition, the system size can entail the largest turbulence, a condition that holds in astrophysical environments. The details of the figure are discussed in the text.

gray w/o dots The parameter space for particles in the RSR that cannot be described diffusively. The maximum turbulence fluctuations have to fit into the source. Therefore, $d_{\mathrm{esc}} \gtrsim l_{\mathrm{max}}$ holds[2] and this parameter space is neglected in the following.

gray w/ dots The parameter space for which particles are in the RSR and can be described diffusively.

white w/ dots The parameter space for which particles are in the QBR but can be described diffusively.

white w/o dots The parameter space for particles in the RSR that cannot be described diffusively.

[2]Note that this condition can be violated by certain initial conditions of the particles, especially if the particles reside predominantly in the system's boundary region.

As the system sizes are larger than the maximum fluctuations, particles in the RSR can be considered as diffusive, hence the condition,

$$r_{\rm g} \lesssim \sqrt{d_{\rm esc}\, l_{\rm c}}\,, \tag{4.34}$$

can be used across regimes to determine the diffusive behavior. This condition translates into

$$E \lesssim qcB\sqrt{d_{\rm esc}\, l_{\rm c}} \approx 30\,{\rm PeV}\cdot\left(\frac{d_{\rm esc}}{10^{13}\,{\rm m}}\right)^{1/2}\left(\frac{l_{\rm c}}{10^{11}\,{\rm m}}\right)^{1/2}\left(\frac{B}{1\,{\rm G}}\right)Z\,. \tag{4.35}$$

To summarize, particles in the RSR are diffusive. Nevertheless, particles in the QBR (white area with dots) may be diffusive. However, in objects where average escape distances are not much larger than the correlation length, such as in plasmoids in AGN jets [25], the range of diffusive particles in the QBR is narrow. Therefore, particles in the RSR can be treated diffusively, while particles in the QBR need a ballistic description.

Figure 4.9 shows lines that correspond to the maximum gyroradii according to Equation (4.34) for different correlation lengths. This figure shows the parameter space of the environments explicitly discussed in this thesis, the plasmoids as high-energy particle sources, the IGMF (Section 5.1), and the Galaxy (Section 5.2).

Isotropic turbulence plus ordered background field: The inclusion of an ordered magnetic field introduces a frame of reference that introduces different transport dynamics along and perpendicular to the ordered field.

1. **Parallel escape:** The condition $\tau_{\rm esc,\parallel} \gtrsim \tau_{\rm diff,\parallel}$ has to hold for a diffusive description. This yields

$$\kappa_\parallel \lesssim \frac{d_{\rm esc,\parallel}\, c}{\sqrt{6}}\,. \tag{4.36}$$

   Consequently, the condition for $r_{\rm g}$ is similar to that given in Equation (4.32), where $d_{\rm esc}$ is the escape in parallel direction $d_{\rm esc,\parallel}$ with respect to the ordered magnetic field component.

2. **Perpendicular escape:** Using the condition $\tau_{\rm esc,\perp} \gtrsim \tau_{\rm diff,\perp}$ yields

$$\frac{d_{\rm esc,\perp}^2}{2\,\kappa_\perp} \lesssim \frac{\lambda_\perp}{c} \approx \frac{\lambda_\parallel}{c} = \frac{3\kappa_\parallel}{c^2}\,, \tag{4.37}$$

   where the assumption of isotropic mean-free paths is applied. This assumption, as well as the relation between the perpendicular and parallel components, shall

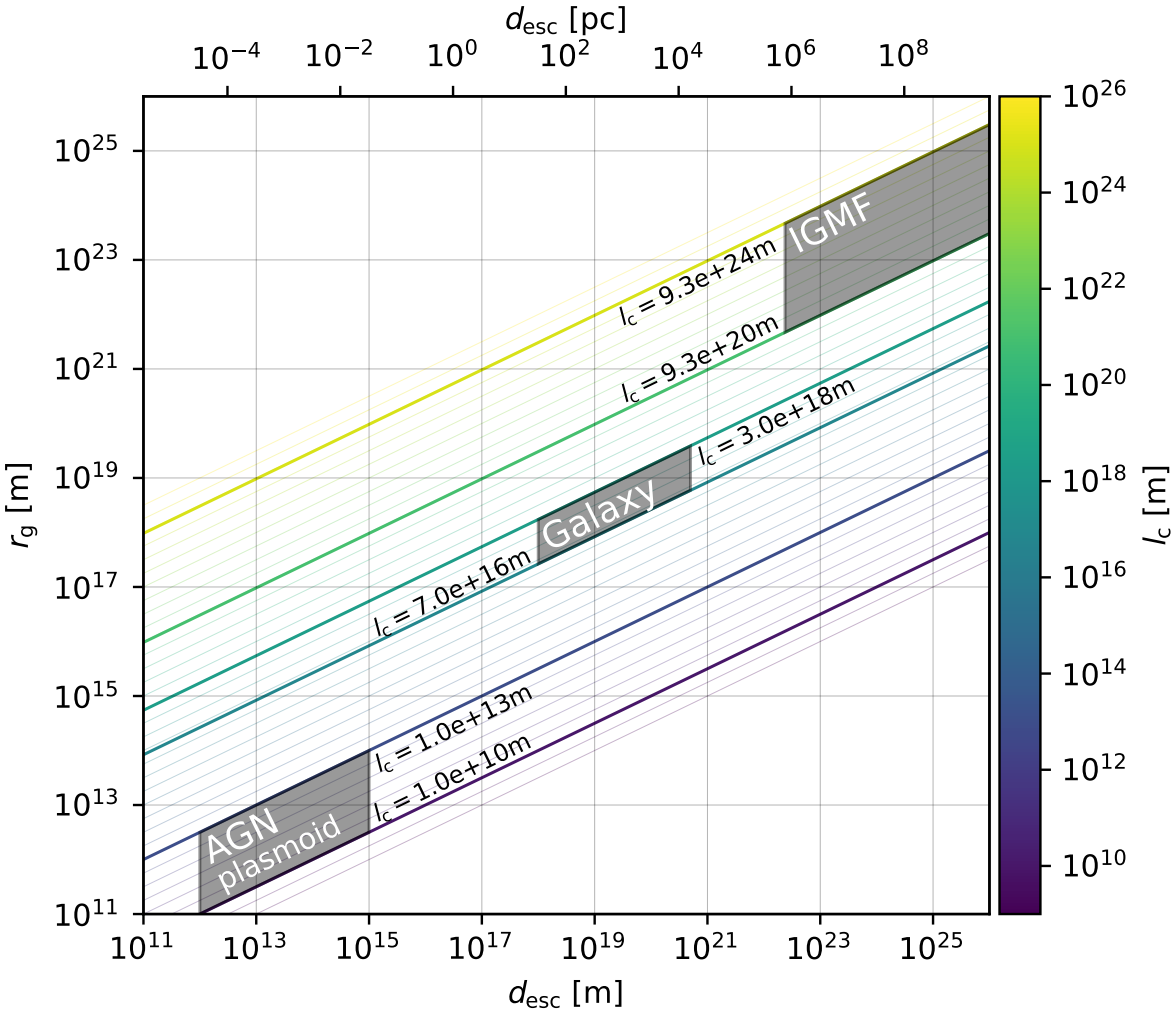

Figure 4.9: Visualization of the criterion in Equation (4.34). The lines indicate the maximum gyroradii allowed for a diffusive description for a fixed correlation length as a function of d_{esc}. The escape distances depend on the particle distribution and the source geometry but are on the order of the source size. If the gyration radius is below the line describing the system, the particle transport can be considered as being diffusive.

be discussed in the next section. Rewriting Equation (4.37) yields

$$\sqrt{\kappa_{\parallel}\,\kappa_{\perp}} \lesssim \frac{d_{\mathrm{esc},\perp}\,c}{\sqrt{6}}\,. \tag{4.38}$$

As $\kappa_{\perp} \lesssim \kappa_{\parallel}$ holds, particles can be always treated diffusively along the perpendicular direction as long as a diffusive description in parallel direction is valid for isotropic system geometries with $d_{\mathrm{esc},\perp} \approx d_{\mathrm{esc},\parallel}$. An interesting case occurs for system geometries where the perpendicular escape distances are much smaller than the parallel ones. Examples with such geometries include spiral galaxies,

flux tubes in the lobes of radio galaxies [27] and elongated jets of (AGN).

Escape times: Having derived the criterion for diffusive transport in astrophysical systems with turbulence, statements regarding the particles' escape time follow. Summerizing Equations (4.22) and (4.23) yields

$$\tau_{\mathrm{esc}} \approx \begin{cases} d_{\mathrm{esc}}/c & \text{ballistic} : r_{\mathrm{g}} \gtrsim \sqrt{d_{\mathrm{esc}}\, l_{\mathrm{c}}} \\ d_{\mathrm{esc}}^2/(2\kappa) & \text{diffusive} : r_{\mathrm{g}} \lesssim \sqrt{d_{\mathrm{esc}}\, l_{\mathrm{c}}} \end{cases} . \tag{4.39}$$

In the diffsive case, this escape time represents an upper limit (see explanation around Equation (4.22). Inserting the dependencies of the diffusion coefficients from Equation (4.29) in turbulence without a mean magnetic field gives

$$\tau_{\mathrm{esc}} \approx \begin{cases} 3\, d_{\mathrm{esc}}^2/(2\, c\, r_{\mathrm{g}}) & \text{diffusive(RSR, Bohm)} : r_{\mathrm{g}} \lesssim \sqrt{d_{\mathrm{esc}}\, l_{\mathrm{c}}} \\ d_{\mathrm{esc}}^2\, l_{\mathrm{c}}/(c\, r_{\mathrm{g}}^2) & \text{diffusive(QBR)} : r_{\mathrm{g}} \lesssim \sqrt{d_{\mathrm{esc}}\, l_{\mathrm{c}}} \\ d_{\mathrm{esc}}/c & \text{ballistic} : r_{\mathrm{g}} \gtrsim \sqrt{d_{\mathrm{esc}}\, l_{\mathrm{c}}} \end{cases} . \tag{4.40}$$

This analytical expression for the escape time is plotted in Figure 4.10, where the dashed line describes the ballistic prediction and the dashed-dotted line describes the diffusive behavior across the transport regimes RSR and QBR. The latter is an upper limit given the above arguments. The marker represents the numerical simulation results of the escape time. For this purpose, 10^3 particles were emitted in isotropic Kolmogorov turbulence at the same location. The time was measured that particles need to reach the spherical shell confining the physical system in this setting. Accordingly, the escape distance is equal to the radius. The figure shows the mean escape times of the particles and the time needed until 99% of the particles escape. Both the transport-related changes predicted from the analytical considerations and the absolute value are remarkably well matched under consideration that the diffusive description yields an upper limit.

4.3 Diffusion Coefficient Components

Besides the already addressed questions about the running diffusion coefficient and its transition from a ballistic to a diffusive phase, the question of the isotropy of the transport arises. In Section 4.1.1, Equations (4.10) and (4.11) showed the difference in the behavior of the perpendicular and parallel components due to an ordered background field. In Figure 4.2 the difference was visualized. A key question is whether the plateau develops simultaneously for both components of the running diffusion coefficients.

Studies of parallel diffusion coefficients have been advanced significantly over time [38, 42, 49, 69, 92, 94, 140, 159, 160, 166]. There remain, however, several open questions, such as what turbulence level $\delta b/B_0$ range allows for the application of QLT

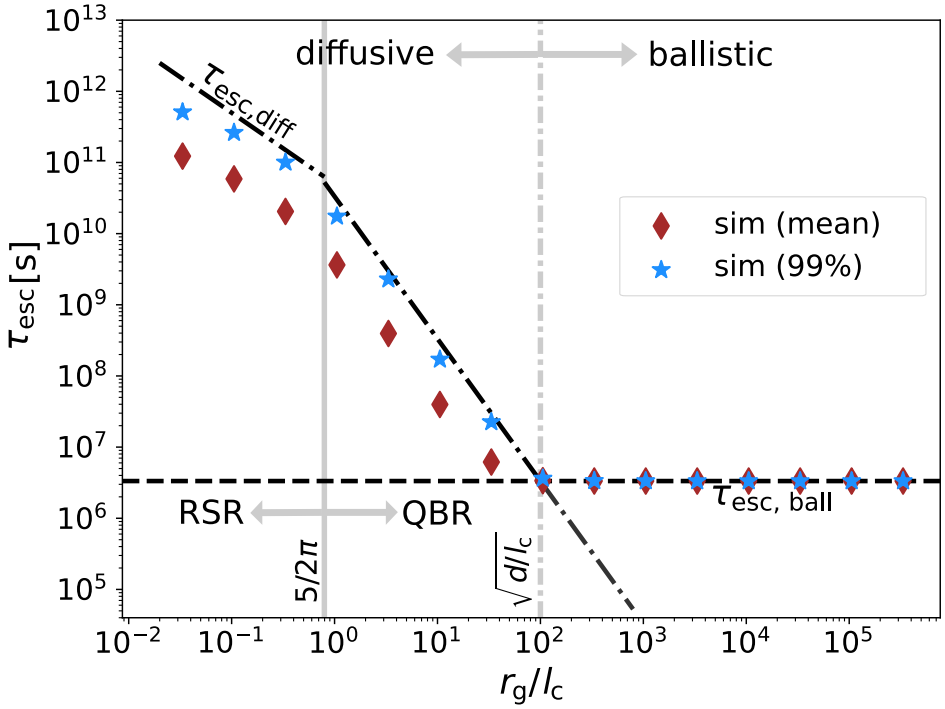

Figure 4.10: Escape time of particles as a function of their gyration radii and the correlation length of the turbulence present. Parameters as in Table 4.1. The black lines reflect the analytical predictions in the three regimes shown (diffusive RSR, diffusive QBR, and ballistic QBR). The diffusive phase spans the two energy transport regimes, RSR and QBR, each with characteristic slopes according to Equation (4.40). In the ballistic transport regime defined by the condition $r_g \gtrsim \sqrt{d_{esc}\, l_c}$, the decay times are energy independent. The markers show simulation results extending over numerous orders of magnitude in particle energy and spanning all three regimes. The time needed for 99% of the particles to escape from the plasmoid and the average escape times is shown. The diffusion limit is an upper limit based on analytical considerations. The simulation results support this.

[140] that was developed for the limit of low turbulence levels. Another aspect is the influence of intermittency on particle transport [63, 163]. Moreover, the perpendicular diffusion coefficients and their relationship to the parallel diffusion coefficient was also subject of many studies [40, 42, 50, 58, 61, 69, 70, 80, 109, 114, 121, 135, 140, 166, 172].

Relation between diffusion tensor components: Knowledge of the relationships between the diffusion coefficient tensor components is essential in determining one component with the understanding of the other one. The relation should cover a wide range of turbulence levels and energies in order to explain the different transport regimes discussed above. In the limit of high turbulence levels ($\delta b/B_0 \gg 1$), for example, equal perpendicular and parallel components of the diffusion coefficient are expected as the charged particles propagate through isotropic turbulence [31, 69, 94].

The outcome of test-particle simulations for 2D, slab, or composite (2D & slab) turbulence can be adequately explained using analytical models. The portfolio of models includes the quasilinear theory (QLT), the nonlinear guiding center theory, and the unified nonlinear theory (see, e.g., [161] for a review). However, these theories fail for isotropic 3D turbulence for particles with small gyroradii $r_{\rm g} \ll l_{\rm c}$ [58, 140]. As the description fails for the RSR, no encompassing theory exists capturing the relation between the parallel and perpendicular components that can explain simulation results over the whole range of turbulence levels for isotropic 3D turbulence.

Despite the lack of an all-encompassing theory, and the known difficulties in RSR, a basic relation of both diffusion coefficients is derived below, which is characterized by its few assumptions and resulting simplicity. Following the nonlinear theory known as the *Bieber and Matthaeus* (BAM) theory [31], deviations from the ideal helices of particles in magnetic fields are caused by the fluctuations through a continuous change of the pitch angle. In contrast to QLT, where particles move on ideal helices, the momentum of particles decorrelates over time. In BAM, the physically motivated assumption of exponentially decaying momentum (velocity) correlations applies

$$\langle v_\perp(t) v_\perp(0) \rangle = \frac{v^2}{3} \cos(\Omega t)\, \mathrm{e}^{-t/\tau_\perp} \,, \tag{4.41}$$

$$\left\langle v_\parallel(t) v_\parallel(0) \right\rangle = \frac{v^2}{3} \mathrm{e}^{-t/\tau_\parallel} \,. \tag{4.42}$$

Here, $\langle \cdot \rangle$ denotes the ensemble average, $\Omega = v/r_{\rm g}$ the angular frequency of the unperturbed orbit, and $\tau_\parallel$ and $\tau_\perp$ are the effective timescales for the decorrelation of the trajectories along and perpendicular to the background field, respectively.

The BAM model assumes the Field-line Random Walk (FLRW) coefficient as a measure of the perpendicular mean-free path. This restrictive assumption is discarded for the sake of generality below since the description of perpendicular transport as FLRW [158, 167] is not realistic in all key astrophysical environments for the particle energies considered in the present thesis. Gyroresonant scattering influences the perpendicular component in the RSR significantly via the cross-field diffusion (see [52] for a discussion).

The TGK formalism allows for the computation of diffusion coefficients as [159],

$$\kappa_\perp = \lim_{t\to\infty} \int_0^t \mathrm{d}\tau \, \frac{v^2}{3} \cdot \cos(\Omega\tau) \cdot e^{-\tau/\tau_\perp} = \frac{v\, r_{\rm g}}{3} \frac{\Omega\tau_\perp}{1+\Omega^2\tau_\perp^2} \,, \tag{4.43}$$

$$\kappa_\parallel = \lim_{t\to\infty} \int_0^t \mathrm{d}\tau \, \frac{v^2}{3} \cdot e^{-\tau/\tau_\parallel} = \frac{v^2\tau_\parallel}{3} = \frac{v\lambda_\parallel}{3} \,. \tag{4.44}$$

Note that this is the same expression for the parallel diffusion coefficient as shown in Equation (3.8). Inserting the angular frequency $\Omega = v/r_{\rm g}$ of the unperturbed orbit

yields

$$\frac{\kappa_\perp}{\kappa_\parallel} = \frac{\tau_\perp}{\tau_\parallel} \frac{1}{1 + v^2\,\tau_\perp^2 / r_\mathrm{g}^2}\,. \tag{4.45}$$

Note that in this section, the gyroradii are defined only with respect to the background field and not with respect to the total magnetic field as in the other sections. The reason for this is the better comparability with other studies on CSR.

Diffusion timescales of diffusion tensor components The physical assumption that the same physical effects, e.g. resonant scattering or FLRW, lead to diffusion along the perpendicular and parallel directions suggest the adoption of

$$\tau_\perp = \tau_\parallel. \tag{4.46}$$

Note that this assumption also underlies the telegraph transport equation since only one timescale τ_diff is specified in Equation (4.1) for the diffusion timescale, even for the anisotropic case. Equal parallel and perpendicular diffusion timescales do not lead to identical diffusion coefficient components, as can be seen in Figure 4.2. Inserting Equation (4.46) and $\tau_\parallel = \lambda_\parallel / v$ from Equation (4.44) into Equation (4.45) yields

$$\frac{\kappa_\perp}{\kappa_\parallel} = \frac{1}{1 + \lambda_\parallel^2 / r_\mathrm{g}^2}\,. \tag{4.47}$$

This result is similar to the hard-sphere model introduced by [72], also known as the classical scattering relation (CSR) within standard kinetic theory. Finally, inserting the definition of the parallel mean-free path,

$$\kappa_\parallel = \frac{v \lambda_\parallel}{3}\,, \tag{4.48}$$

into Equation (4.47) results in

$$\frac{\kappa_\perp}{\kappa_\parallel} = \left(1 + \frac{9\kappa_\parallel^2}{v^2\, r_\mathrm{g}^2}\right)^{-1}\,. \tag{4.49}$$

The simulation results of the parallel and perpendicular diffusion coefficients shown in Figure 4.4 are used to evaluate Equation (4.49). The deviation from the simulation

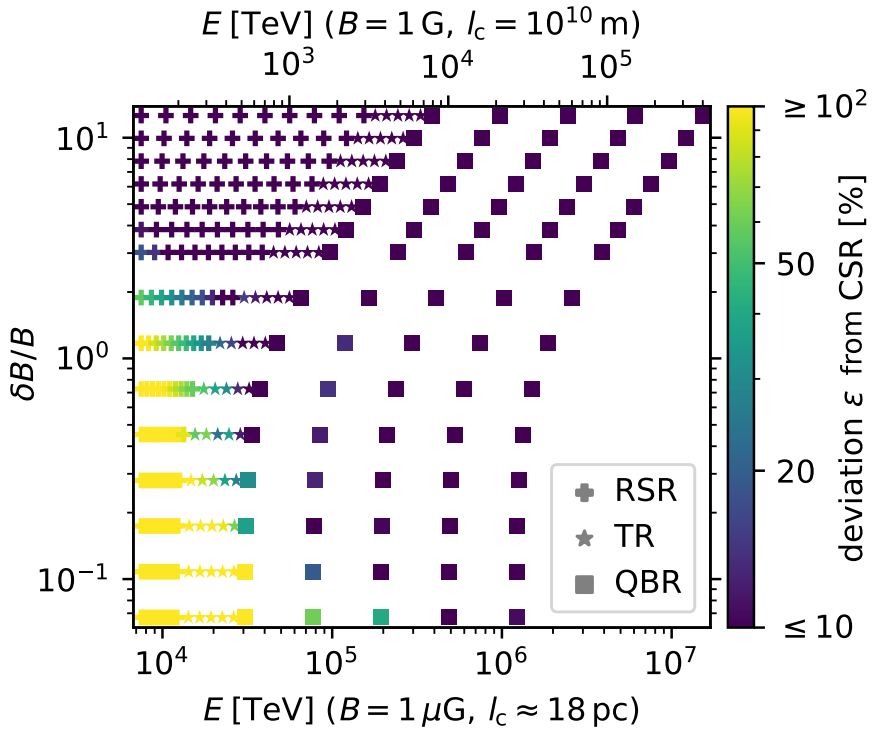

Figure 4.11: Comparison between simulation results and CSR predictions for $\kappa_\perp/\kappa_\parallel$ according to Equation (4.47). The parameter space is shown in Figure 4.4 and its caption, where all individual diffusion coefficient component are shown. Deviations between simulation results and CSR are computed via Equation (4.51) and color coded. Taken from Reichherzer et al. (2021, [139]).

result from the CSR prediction are computed via

$$\varepsilon = \left| \left(\frac{\kappa_\perp}{\kappa_\parallel}\right)_{\text{sim}} - \left(\frac{\kappa_\perp}{\kappa_\parallel}\right)_{\text{CSR}} \right| \cdot \left(\frac{\kappa_\perp}{\kappa_\parallel}\right)^{-1}_{\text{CSR}} \tag{4.50}$$

$$= \left| \left(\frac{\kappa_\perp}{\kappa_\parallel}\right)_{\text{sim}} - \frac{1}{1 + (3\kappa_{\parallel,\text{sim}})^2/(v\, r_\text{g})^2} \right| \cdot \left(1 + \frac{(3\kappa_{\parallel,\text{sim}})^2}{(v r_\text{g})^2}\right) , \tag{4.51}$$

and presented in Figure 4.11 via the color code.

Since only the ratio r_g/l_c is relevant for the diffusion coefficients shown in Figure 4.4, this plot is more universal than indicated by the limited range of particle energies on the lower x-axis of Figure 4.11 that corresponds to the exact simulation parameters. With an arbitrary factor, the range of particle energy can be scaled to another if, at the same time, the magnetic field or the correlation length is scaled in the same way. For illustration, the upper x-axis labels are obtained with a magnetic field 10^6 times larger than that on the lower x-axis label. At the same time, the correlation length is scaled down by a factor of $5 \cdot 10^7$. Effectively, therefore, the energy range has decreased by a factor of 50 and represents the particle energies in the setup of an exemplary AGN

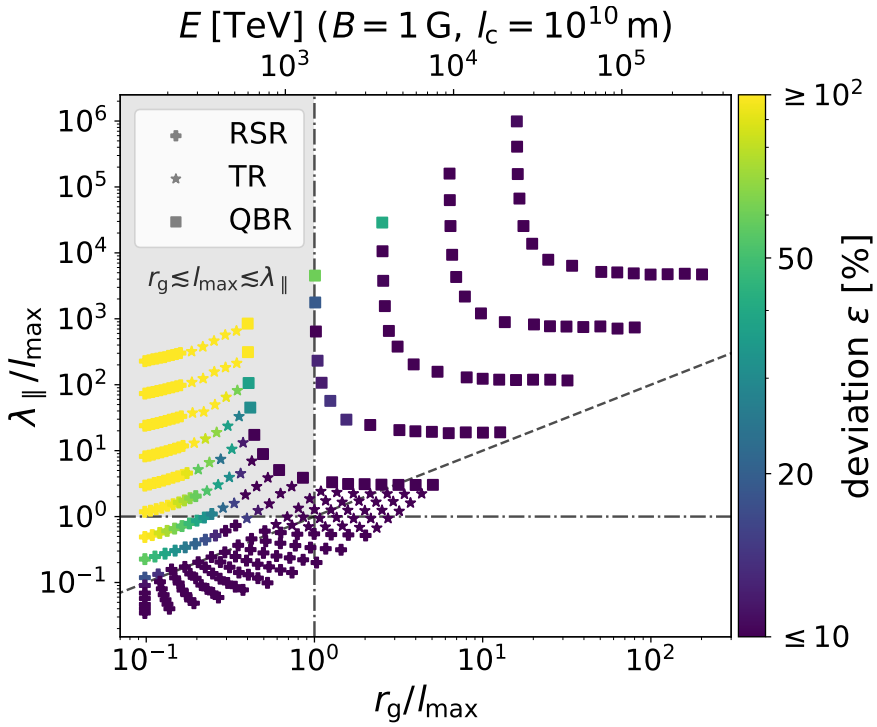

Figure 4.12: Plot of the ratios $\lambda_\parallel/l_{\rm max}$ vs the ratios $r_{\rm g}/l_{\rm max}$. The parameter space $r_{\rm g} \lesssim l_{\rm max} \lesssim \lambda_\parallel$ is highlighted with gray color. Taken from Reichherzer et al. (2021, [139]).

plasmoid as described in Section 4.1.3.

The agreement between simulation results and CSR is given over a wide range of parameters. Significant deviations only occur in the RSR $r_{\rm g} \lesssim l_{\rm max}$ for low turbulence levels, where the parallel mean-free paths are large $l_{\rm max} \lesssim \lambda_\parallel$. By showing $\lambda_\parallel/l_{\rm max}$ vs $r_{\rm g}/l_{\rm max}$ in Figure 4.12, the parameter space $r_g \lesssim l_{\rm max} \lesssim \lambda_\parallel$ is visualized in the grey area. Poor agreement between the CSR and the simulation results is found within this area, which suggests that although these particles are scattered by resonant waves, a significant part of the perpendicular displacement is due to FLRW. The latter part of the inequality arises from the fact that these deviations appear for low turbulence levels, where the parallel mean-free paths are particularly large and typically much larger than $l_{\rm max}$.

Figure 4.13 presents the ratio $\kappa_\perp/\kappa_\parallel$ as a function of the ratio $\lambda_\parallel/r_{\rm g}$, where $\lambda_\parallel = 3\kappa_\parallel/v$ is determined according to Equation (4.47). The theoretical CSR prediction from Equation (4.49) is shown as the gray line. Note that the turbulence level is not fixed and varies according to the parameter space shown in Figure 4.11. Deviations of the simulation results from these CSR predictions are computed via Equation (4.51) and shown in the lower panel. Here, as well as in Figure 4.11, good agreement between theory and simulation results for higher particle energies are evident. Wherever the CSR prediction fits the simulation results, the assumption $\lambda_\parallel = \lambda_\perp$ underlying Equa-

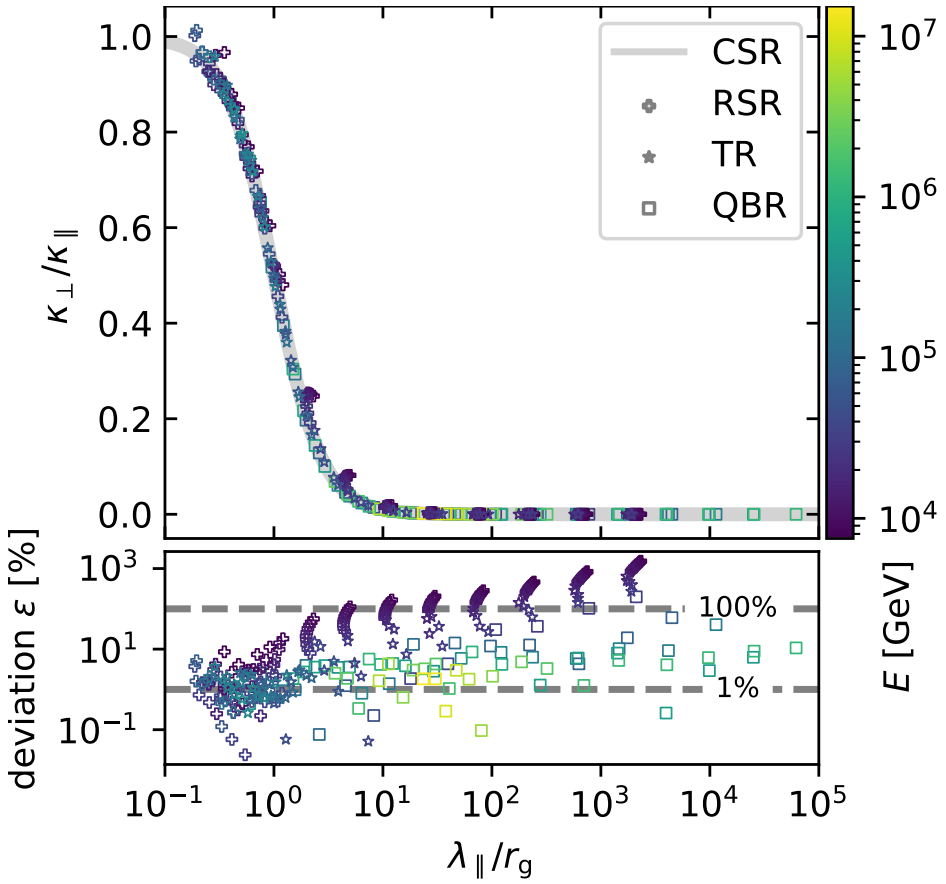

Figure 4.13: Top panel shows the ratio of perpendicular to parallel diffusion coefficient as a function of the ratio $\lambda_\parallel/r_g$. The particle energy is color coded. The entire parameter space is shown in Figure 4.11. The theory prediction is indicated by the gray line. The lower panel shows the deviation of the simulation results from the theory prediction, which is determined by Equation (4.51). Taken from Reichherzer et al. (2021, [139]).

tion (4.49) is satisfied to a certain degree. This fits a wide range except for the RSR for low turbulence levels. The good agreement over the large parameter space, especially for high turbulence levels and particle energies, stems from the following two reasons:

1. High turbulence levels isotropize the diffusion process and consequently also the diffusion timescales. This consideration is valid regardless of the particle energy and favors the assumption of CSR $\tau_\perp = \tau_\parallel$.

2. High-energy particles in the QBR exhibit a behavior of $\kappa_\parallel \propto \lambda_\parallel \propto E^2$ and $\kappa_\perp \propto \lambda_\perp \propto E^0$ (see Section 4.1.2 for details). The energy-independent FLRW dominates the energy-independent diffusion along the perpendicular component since resonant scattering is suppressed in the QBR according to the gyroresonance criterion. This finding is in agreement with [122]. The effect of the FLRW arises from isotropic diffusion and consequently leads to identical diffu-

sion timescales perpendicular and parallel to the oriented background magnetic field.

Predictive theory for perpendicular diffusion coefficient In addition to statements about the identical timescales in the perpendicular and parallel directions, the results can be used to derive an expression for the perpendicular diffusion coefficients. According to the argumentation from above, the following relation derived from Equation (4.49) is valid wherever a sufficiently good agreement between CSR and simulation results in Figure 4.11 is given:

$$\kappa_\perp = \frac{\kappa_\parallel}{1 + (3\kappa_\parallel)^2/(v\, r_\mathrm{g})^2}. \tag{4.52}$$

In the QBR $\lambda_\parallel \gg r_\mathrm{g}$ holds and thus

$$\kappa_\perp = \frac{\kappa_\parallel}{1 + \lambda_\parallel^2/r_\mathrm{g}^2} \overset{\lambda_\parallel \gg r_\mathrm{g}}{\approx} \frac{v\, r_g^2}{3\lambda_\parallel}. \tag{4.53}$$

With $\kappa_\parallel \propto r_\mathrm{g}^2$ from Equation (4.13), $\kappa_\perp \propto r_\mathrm{g}^0 \propto E^0$ applies, a scaling that that can be seen in Figure 4.4.

These relations are useful in that one may recover under consideration of a few physically well-motivated assumptions the difficult-to-evaluate perpendicular diffusion from the better-understood and more accessible parallel diffusion.

4.4 Summary

1. **Influence of CR-transport effects on multi-messenger signatures**
   The transport of charged particles in magnetized source regions alters their spectra and escape times. These modifications are carried over from the cosmic rays (CRs) to the secondaries by interaction processes. Therefore, understanding charged particle transport contributes to a better understanding of multi-messenger signatures through a further layer of complexity.

2. **Analytical description of isotropic running diffusion coefficients**
   By solving the telegraph equation, an analytical form of the running diffusion coefficient is provided in Section 4.1. This is important to describe particle distributions statistically accurately at any time and not just in the limit of large times as available with diffusion coefficients. Furthermore, this analytical description serves as a reference for evaluating different numerical propagation methods of CRs in turbulence. The comparison in astrophysical source environments demonstrates the excellent agreement between simulation results of the correlated random walk routine with concomitant performance gains.

3. **Criterion for classifying the CR transport into ballistic and diffusive regimes and its consequences for multi-messenger spectra**
   In Section 4.2, criteria for the justification of the diffusive description of particle transport are derived, depending on the particle energy and the properties of the source environment. It follows immediately that particles in the resonant-scattering regime can always be described diffusively. According to the leaky-box model, the classification into diffusive and ballistic transport has immediate consequences for the spectrum of CRs and secondary particles, as only energy-dependent diffusion modifies its shape.

4. **Unified description of escape times from source environments**
   The criterion for classifying the CR transport into diffusive and ballistic allows statements on the spectrum and predictions on escape times from source environments. The three regimes are:

   (a) Escaping particles in the RSR $r_\mathrm{g} \lesssim 5\, l_\mathrm{c}/2\pi$ can be considered diffusively.

   (b) If the particles are in the QBR $r_\mathrm{g} \gtrsim 5\, l_\mathrm{c}/2\pi$, but the escape distances are very large $d_\mathrm{esc} \gg l_\mathrm{c}$ due to large source environments, there is a range $5\, l_\mathrm{c}/2\pi \lesssim r_\mathrm{g} \lesssim \sqrt{d_\mathrm{esc}\, l_\mathrm{c}}$ for which particles escape diffusively.

   (c) Escaping particles in the QBR for which $r_\mathrm{g} \gtrsim \sqrt{d_\mathrm{esc}\, l_\mathrm{c}}$ holds must be considered ballistically.

   The expression for escape times across these three different regimes is derived as a function of the gyration radius of the particles, the magnetic field strength and the correlation length of the turbulence. Numerical simulation results presented support these predictions.

5. **The transition to the diffusive phase coincides in perpendicular and parallel directions**
   Even though the diffusion coefficients perpendicular and parallel to an oriented magnetic field may differ significantly, the time required to reach the respective steady-state values is similar, especially for high-energy particles in astrophysical sources. This finding offers a convenient formula for the otherwise difficult-to-evaluate perpendicular diffusion coefficient based on the better-understood and more accessible parallel diffusion.

Chapter 5

Journey of Messengers from Sources to Earth

The running diffusion coefficient exhibits a transition from ballistic to diffusive transport phase, where the running diffusion coefficients remain constant. Both phases, including the transition, can be described through the telegraph equation. Section 4.2 explains this concept in more detail and illustrates its implications for transient phenomena in astrophysical high-energy particle sources. It is shown that the transport properties of charged particles in source regions with high proton and photon target densities determine how long particles are confined. Therefore, the associated escape times of charged particles directly and significantly influence the secondaries created by interaction processes.

In the present chapter, the focus shifts towards the journeys of these particles between sources and the Milky Way. During most of the journey, the particles move through astrophysical regions with low particle density. The analogy between transport in source regions and between the sources and the Earth is exploited. The description of the escape times in the three regimes, diffusive RSR, diffusive QBR, and ballistic QBR, found in source regions, can be adopted to describe the required source-to-Earth travel time.

This chapter is divided into two parts, the source-to-Galaxy (Section 5.1) and the Galaxy-to-Earth (Section 5.2) propagation. The focus of the first part is the discussion on the transport of charged particles through the intergalactic magnetic field (IGMF) as it modifies the arrival times and isotropizes the arrival directions of CRs at the Milky Way. Fundamentally, the effects of the presence, albeit weak, of magnetic fields can add up due to the large distances between sources and the Milky Way. The following discussion on transport-related effects is based on my contributions to the papers and proceedings on CRPropa [17] and PropPy [138] (see details in disclaimer in Chapter 4).

Furthermore, my analytical consideration of the particle distribution as a function of time and the diffusion coefficient, which I contributed to the publication

- L. Schlegel*, A. Frie, B. Eichmann, **P. Reichherzer**, and J. Becker Tjus, "Interpolation of Turbulent Magnetic Fields and Its Consequences on Cosmic Ray Propagation", *The Astrophysical Journal*, 889, 2, 2020 — doi:10.3847/1538-4357/ab643b,
  where I developed statistical criteria to quantify the effect of turbulence interpolation on cosmic-ray propagation. Furthermore, I supported L. Schlegel in finding the final simulation setup,

is employed.

The second part of this chapter describes how messengers reaching our Galaxy after a long journey through the IGMF are exposed to renewed environmental changes. This affects particularly charged particles due to the significant increase in the magnetic field strength. The influence on the transport of charged particles in the Galaxy is discussed in Section 5.2 and applies some aspects of the publication

- **P. Reichherzer***, L. Merten, J. Dörner, J. Becker Tjus, M.J. Pueschel, and E.G. Zweibel, "Regimes of cosmic-ray diffusion in Galactic turbulence", *SN Applied Sciences*, 4, 15, 2022 — doi:10.1007/s42452-021-04891-z.

5.1 Particle Journey from Source to Galaxy

5.1.1 Transport Effects

The influence of the IGMF on the transport behavior of charged particles depends on their energies and the magnetic field properties. Knowledge of this influence is essential for determining the direction of origin and arrival times. Here, a fundamental question is whether particles can be described diffusively based on their energy and as a function of the distance between sources and the Milky Way. This question shall be treated equivalently to the one concerning the diffusivity of particles in sources according to Section 4.2. Even if the mean-free-path lengths in the IGMF become much larger than in source regions, it must be noted that these are now compared to the astronomical distances between sources and the Milky Way. For particles that become diffusive before reaching our Galaxy, the directional information is completely lost. In contrast, sufficiently high-energy particles arrive at the Galaxy with only minor deflections. At the very highest energies, the hope is thus to observe UHECRs attributable to a point source.

In analogy to whether particle transport in sources can be described diffusively, now follows a similar discussion for transport between sources and the Milky Way. The escape distance used to describe the escape times translates for determining the time needed for the source-to-Galaxy transport into the distance between source and Milky Way $d_{\mathrm{s-MW}} \approx d_{\mathrm{esc}}$. The difference in this analogy, however, is that particles escape after traveling the distance d_{esc} from sources, whereas diffusive particles in the IGMF can move temporarily farther away from the source than $d_{\mathrm{s-MW}}$. Diffusion could

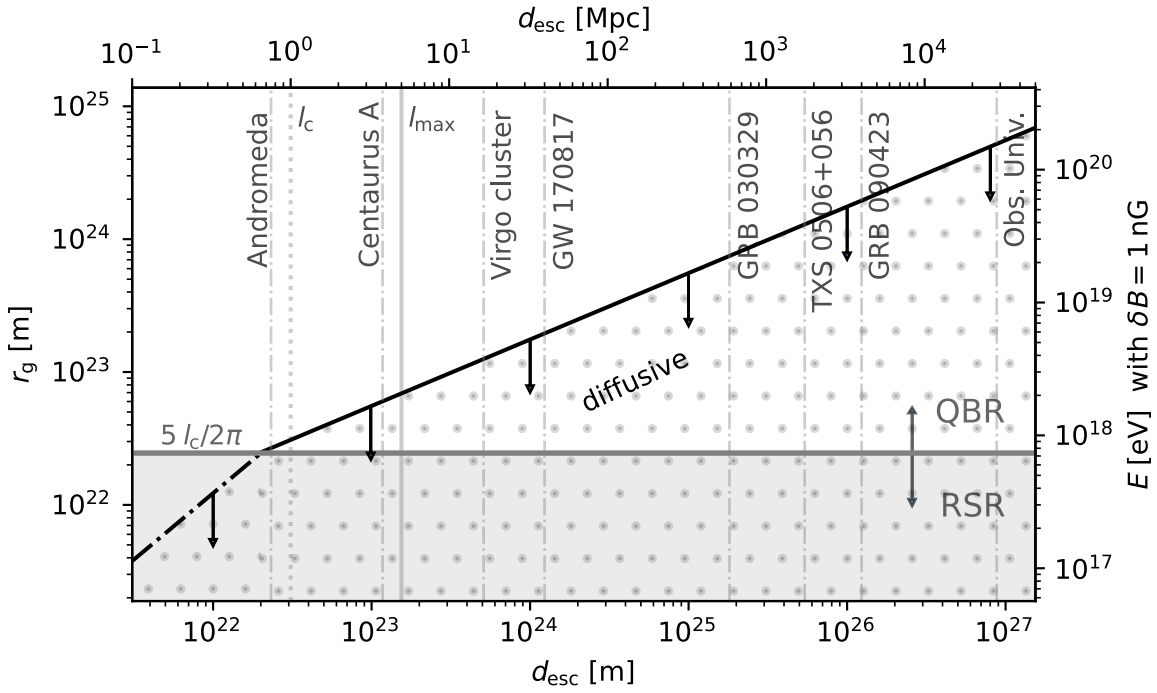

Figure 5.1: Visualization of the criterion from Equation (4.32) for determining the validity of a diffusive particle description as a function of the distance between source and Milky Way $d_{\rm s-MW} \approx d_{\rm esc}$ and particle energies. Particles below the black line can be considered diffusive. The entire parameter space for diffusive transport is highlighted with dots. The details of the figure are discussed in the context of the similar Figure 4.8.

cause them to return to the Milky Way. This difference is noticeable in the expected time needed,

$$\tau_{\rm s-MW,\,diff} \approx \frac{d^2_{\rm s-MW}}{2\kappa}\,, \tag{5.1}$$

which is consequently larger in comparison with the case described in Equation (4.22) within sources. The time needed for particles to travel between sources and the Milky Way for the ballistic transport yields

$$\tau_{\rm s-MW,\,ball} \approx \frac{d_{\rm s-MW}}{c}\,. \tag{5.2}$$

The conditions for diffusive transport derived in Section 4 lead to a plot similar to Figure 4.8 for the distinction between diffusive and ballistic transport. This is shown in Figure 5.1. The discussion of this function is equivalent to that for Figure 4.8 with the only difference that the distance between sources and Milky Way may be smaller than l_c. However, the most important conclusions are summarized here:

1. The figure shows that from the Andromeda galaxy on, the transport for particles

in the RSR is always diffusive.

2. In the QBR, particle transport for $5\,l_\mathrm{c}/2\pi \lesssim r_\mathrm{g} \lesssim \sqrt{l_\mathrm{c}\,d_{\mathrm{s-MW}}}$ can be described diffusively.

3. In the QBR, particle transport for $r_\mathrm{g} \gtrsim \sqrt{l_\mathrm{c}\,d_{\mathrm{s-MW}}}$ cannot be described diffusively.

For the three regimes, the RSR (always diffusive), the QBR (diffusive), and the QBR (ballistic), the travel times yields in average

$$\tau_{\mathrm{s-MW}} \approx \begin{cases} 9.0\cdot 10^6\,\mathrm{yr}\,\left(\frac{d_{\mathrm{s-MW}}}{\mathrm{Mpc}}\right)^2\left(\frac{B}{\mathrm{nG}}\right)\left(\frac{E}{\mathrm{EeV}/2}\right)^{-1} & \text{diffusive (RSR, Bohm)} \\ 5.6\cdot 10^6\,\mathrm{yr}\,\left(\frac{d_{\mathrm{s-MW}}}{\mathrm{Mpc}}\right)^2\left(\frac{l_\mathrm{c}}{\mathrm{Mpc}}\right)\left(\frac{B}{\mathrm{nG}}\right)^2\left(\frac{E}{\mathrm{EeV}/2}\right)^{-2} & \text{diffusive (QBR)} \\ 3.3\cdot 10^6\,\mathrm{yr}\,\left(\frac{d_{\mathrm{s-MW}}}{\mathrm{Mpc}}\right) & \text{ballistic (QBR)} \end{cases} . \tag{5.3}$$

Note that the Bohm scaling applies to isotropic 3D Kolmogorov turbulence without a directed magnetic field.

5.1.2 Comparison of Simulation Techniques

Consequently, the transport of particles of a broad energy spectrum from distant sources to the Galaxy must account for the ballistic and the diffusive regime. Due to the large distances involved, efficient methods are necessary. In search for suitable propagation methods and in analogy to the comparison of the different transport methods in source regions (see Figure 4.7), a comparison for the propagation of charged particles in the IGFM is presented. The simulation setup contains an isotropic 3D Kolmogorov turbulence with a spectral index = 5/3, a magnetic field strength $B_\mathrm{rms} = 1\,\mathrm{nG}$, a correlation length $l_\mathrm{c} = 1\,\mathrm{Mpc}$, wich is within the current constrained parameter space [16]. In each simulation, 10^3 particles are propagated with $E = 10\,\mathrm{EeV}$. These particles are in the QBR as $r_\mathrm{g} \gg l_\mathrm{c}$ with $\kappa \approx 1.1\,\mathrm{pc}^2/\mathrm{s}$ following Equation (4.13). Figure 5.2 shows the required computation times of the simulations as a function of the resolution expressed in the step sizes. The trajectory lengths $l_\mathrm{traj} = 1.3\cdot 10^5\,\mathrm{Mpc}$ in the simulation exceed the mean-free paths $\lambda = 3\kappa/c \approx 350\,\mathrm{Mpc}$. According to Equation (4.6) all particles are diffusive at the end. The deviations from the analytical prediction are shown color-coded in Figure 4.7. Since the particles in this setup are diffusive, the description is applicable to all methods, particularly the diffusive ones. The correlated random walk (CRW) and the diffusive approach show again the best performance. For the case of smaller distances between source and earth $d_\mathrm{s} \ll \lambda$, the diffusive approach is not applicable anymore. Here, the failure of the diffusive approach is equivalent to the behavior shown in the lower panel of Figure 4.7 for the ballistic case.

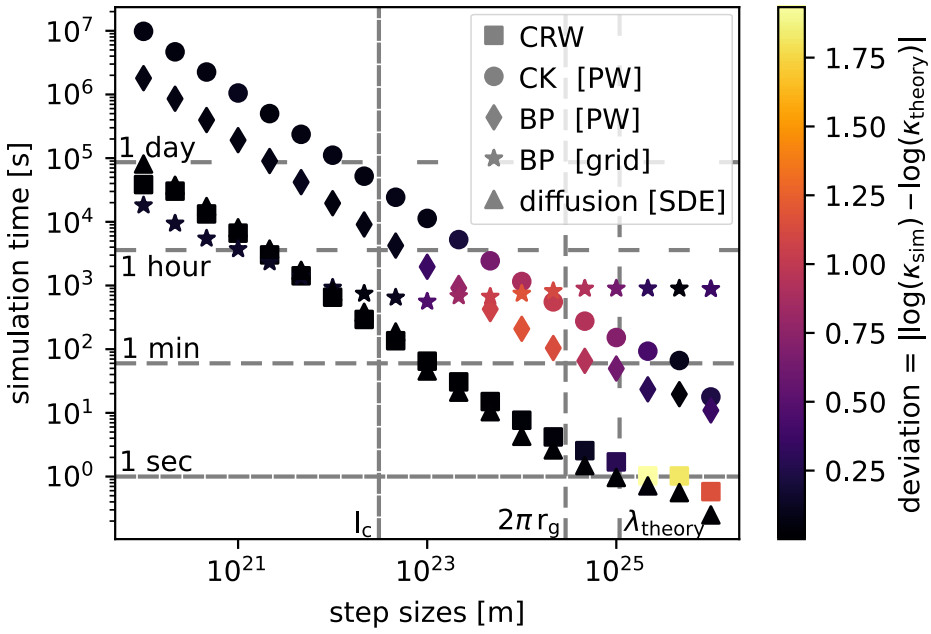

Figure 5.2: Comparison of simulation time (sum of the system and user CPU) for numerical simulations with propagation techniques presented in Section 3.2.2 as functions of step sizes. Taken from Reichherzer et al. (2022, [138]).

5.2 Propagation in the Galaxy Towards Earth

The Galactic magnetic field strengths are at least 3 orders larger than those of the IGMF ($B_{\mathrm{MW}}/B_{\mathrm{IGMF}} \approx 10^3$), accompanied by significantly smaller correlation lengths $l_c \lesssim 100\,\mathrm{pc}$ of the turbulence ($l_{c,\mathrm{MW}}/l_{c,\mathrm{IGMF}} \approx 10^{-4}$) [16]. Applied to the findings of Chapter 4, it follows that the scales $d \approx r_g^2/l_c$ on which the transport of charged particles becomes diffusive yields

$$d_{\mathrm{MW}} = \left(\frac{B_{\mathrm{IGMF}}}{B_{\mathrm{MW}}}\right)^2 \left(\frac{l_{c,\mathrm{IGMF}}}{l_{c,\mathrm{MW}}}\right) d_{\mathrm{IGMF}} \approx 10^{-2}\, d_{\mathrm{IGMF}}, \tag{5.4}$$

and thus decreases compared to the IGMF for particles with fixed energy. Hence, the following two questions arise from this aspect:

1. What is the influence of the Galactic magnetic fields on the high-energy particles from extragalactic sources that are propagated to us through the IGMF? At what energies do charged particles become diffusive when traveling from the edge of our Galaxy to Earth?

2. At what energies will CR transport from Galactic sources of different distances become diffusive? This question is particularly relevant for nearby sources, as point sources may be identified for ballistic, non-yet diffusive, transport.

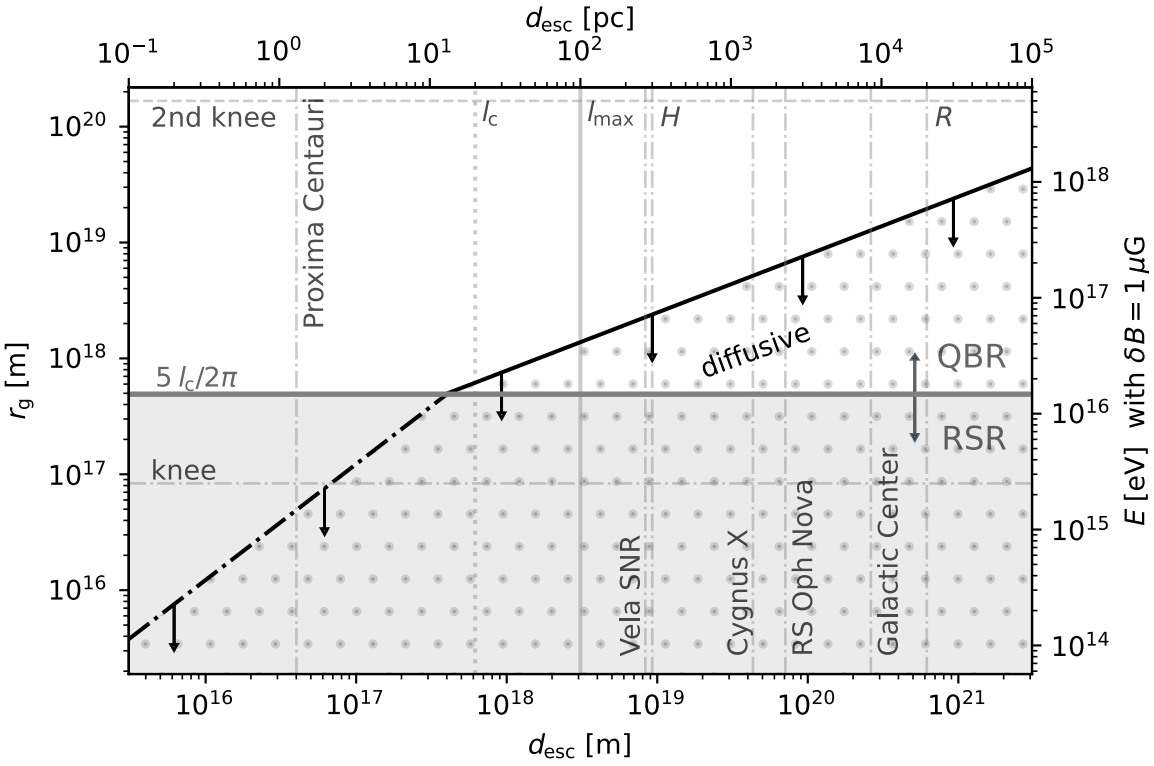

Figure 5.3: Visualization of the criterion from Equation (4.32) for determining the validity of a diffusive particle description as a function of their energies ($Z = 1$) and the distance of Galactic sources to Earth ($\approx d_{\mathrm{esc}}$). Particles below the black line can be considered diffusive. The complete parameter space for diffusive transport is highlighted with dots. The details of the figure are discussed in the context of the similar Figure 4.8.

In analogy to Figures 4.8 and 5.1, Figure 5.3 shows the critical gyroradii and energies in the context of the Milky Way, below which particle transport can be described diffusively, for the given source distance. The Galaxy's scale height $H \approx 300\,\mathrm{pc}$ and its radial extent $R \approx 20\,\mathrm{kpc}$ are marked. These provide references to the minimum and maximum distances that extragalactic particles must travel in the Galactic magnetic field in order to be observed on Earth. If particle energies from extragalactic sources are below 100-500 PeV, their transport can be described diffusively within our Galaxy according to Figure 5.3. Consequently, the directional information is lost upon arrival on Earth. Furthermore, examples of sources of Galactic CRs discussed in the literature [37, 78] are marked in the figure. The H.E.S.S. and MAGIC detection of very-high-energy gamma rays from the recurrent nova RS Ophiuchi and their analysis in [78, 112] has provided a maximum energy $E \approx 10\,\mathrm{TeV}$ up to which protons can be accelerated in Galactic nova with similar properties. When compared with Figure 5.3, it becomes clear that charged particles from these events will reach Earth diffusively and thus cannot provide any clues about their origin by means of arrival directions.

The horizontal lines in Figure 5.3 show the knee and the 2nd knee (see Figure 2.2). All charged particles below the knee from extrasolar sources (except Proxima Centauri) are diffusive on arrival at Earth. Particles above the 2nd knee of the cosmic-ray energy spectrum, on the other hand, cannot be described diffusively and therefore do not lose their directional information when crossing the Galaxy. Consequently, these particles of Galactic origin should be traceable to their origin on nearly rectilinear trajectories. However, whether statements about their extragalactic origin are possible depends also on their source distance, according to the discussion in Section 5.1.

5.3 Summary

1. **Generalizing criterion for classifying the CR transport into ballistic and diffusive regimes**
   Extragalactic CRs that satisfy $r_\mathrm{g} \lesssim \sqrt{d_{\mathrm{s-MW}}\, l_\mathrm{c}}$ have lost their directional information upon reaching our Galaxy. The diffusion equation describes their transport. Figure 5.1 provides instantaneous statements about the classification into diffusive and ballistic propagation depending on the distance of the source and the particle energy.

2. **Which conditions permit tracing CRs origin from their arrival directions?**
   In Section 5.2, the influence of the Galactic magnetic field on the trajectories of charged particles toward Earth is discussed. Criteria are shown to discern which particles of (extra-)Galactic origin can be considered diffusive. On the other hand, conditions are presented to infer the origin of CRs based on the arrival direction.

3. **Advantages of the correlated random walk propagation method**
   Comparisons of numerical simulations in the intergalactic magnetic field underline the excellent applicability of the CRW-based propagation method.

Chapter 6

Conclusions & Outlook

The joint observation of gravitational waves and the electromagnetic counterparts of a binary neutron star merger and the first evidence for a blazar being a source of high-energy neutrino in 2017 contributed significantly to ushering in the era of multi-messenger astronomy. Key challenges in multi-messenger astronomy include associating observed messengers with physical processes and their temporal and spatial characterization of transient phenomena, as summarized in Chapter 2. Furthermore, different astrophysical processes create other messengers, which reveal complementary information about their sources. Only the account of these aspects allows a detailed understanding of transient phenomena.

The investigation of these key aspects under consideration of realistic modeling requires the usage of numerical tools. These tools were described in Chapter 3 and used to investigate the transient phenomena subsequently. Observation of one of these messenger types of a transient event demands coordinated searches for other messengers. Using software to coordinate follow-up observations of complementary messengers is described in Chapter 3.1.4.

In this thesis, numerical propagation tools are improved and utilized to investigate analytical predictions as the messengers escape from their sources (see Chapter 4) and travel through the intergalactic magnetic field and the Galactic magnetic field to Earth (see Chapter 5).

The key conclusions are:

1. **Novel tool for the planning of follow-up campaigns** Tools commonly used for planning follow-up observations constitute a patchwork of disparate systems, data formats, communication techniques of relevant information, and alerts of transient phenomena. Astro-COLIBRI acts as a comprehensive platform accommodating the information transmitted through this ecosystem of real-time multi-messenger systems. In addition, the platform further automates the coordination of follow-up observations by providing bundled event information and linking detailed information through its graphical interface that is easily understandable for humans.

2. **Detection of most distant very-high-energy AGN** Dynamical effects discussed in the thesis in the source region induced variability on timescales that allowed follow-up observations of H.E.S.S. based on an alert emitted by *Fermi*. Astro-COLIBRI has assisted in coordinating follow-up observations by providing helpful information and offering mobile access, especially useful during the coordination over the weekends.

3. **Enhancing propagation software to study real-time effects in transient sources** Physical processes in transient sources provide a variety of highly complex phenomena with different timescales and temporal variations of multi-messenger signatures. Their understanding requires performing numerical simulations with realistic modeling of astronomical environments. With the development of a novel routine based on the correlated random walk, efficient modeling of charged particle transport is realized that correctly describes both the initial ballistic and the later diffusive transport phase.

4. **Classification into ballistic and diffusive transport** An analytical expression for the running diffusion coefficients is found by solving the transport equation. This allows the description of distributions of charged particles at arbitrary times in turbulence. Moreover, proceeding from this expression, criteria are derived to infer the applicability of a diffusive propagation description.

5. **Theory for transport-related escape times from source regions** The aspects discussed in the thesis are reconciled with deriving an analytical expression for the escape times across energy- and transport regimes. Building on the study of the transition from ballistic to diffusive transport, three distinct regimes with different scalings of the escape time is found:

   (a) Escaping particles in the RSR ($r_\mathrm{g} \lesssim 5\, l_\mathrm{c}/2\pi$) can be considered diffusively.

   (b) If the particles are in the QBR ($r_\mathrm{g} \gtrsim 5\, l_\mathrm{c}/2\pi$), but the escape distances are very large $d_\mathrm{esc} \gg l_\mathrm{c}$ due to large source environments, there is a range $5\pi\, l_\mathrm{c}/2\pi \lesssim r_\mathrm{g} \lesssim \sqrt{d_\mathrm{esc}\, l_\mathrm{c}}$ for which particles escape diffusively.

   (c) Escaping particles in the QBR for which $r_\mathrm{g} \gtrsim \sqrt{d_\mathrm{esc}\, l_\mathrm{c}}$ holds must be considered ballistically.

   Numerical simulations verify these predictions. Applied to particle spectra, the predictions for the escape time differ significantly from the assumptions of purely diffusive or ballistic transport commonly employed in the literature.

6. **Theory for CR source-to-Earth travel time** The theory for transport-related escape times from source regions is generalized to describe the influence of deflections in the IGMF and the Galactic magnetic field on the travel times of charged particles between sources and the Earth. Criteria are presented to

discern which particles of (extra-)Galactic origin can be considered diffusive on arrival on Earth.

Outlook The current landscape of tools for different, mostly highly specialized cases of multi-messenger astrophysics requires adaptation to the challenge of next-generation observatories through connections and joint structures. The development of Astro-COLIBRI as a holistic platform is one step in this direction. To further proceed, we will organize an international multi-messenger workshop[1] at Ruhr-University Bochum in September 2022. The key objective of this workshop is to develop and disseminate a research agenda on interconnecting software tools in real-time multi-messenger astronomy. In addition to presentations by international experts in the field, a hackathon-like event forms an essential part of the workshop, in which the objective is pursued in concrete steps. In addition to the usage of Astro-COLIBRI for the planning of follow-up observations in H.E.S.S., other possible applications are elaborated on. There are already advanced tests for using Astro-COLIBRI by the scientists on call, the burst proponents, for the upcoming SVOM satellite launching in mid 2023.

In addition to planning coordinated follow-up campaigns, modeling of physical effects in source regions and effects during the transport towards Earth requires improvement. For example, the influence of the transport-related modifications of CR spectra and escape times on multi-messenger observables warrants quantification in further studies. Especially, the findings on escape times serve as input for complex semi-analytical models of transient sources. However, these studies or simulation codes typically employ too-simplified assumptions of energy-independent [36, 149] or purely diffusive [51, 103] scaling of the escape times or no escape at all [126] and would thus benefit from the analytical expressions for escape times presented here.

The excellent suitability of the correlated random walk for ballistic and equally diffusive extragalactic propagation paves the way for more efficient simulations of the CR transport from sources to the Galaxy.

[1] `https://astrophysics-workshop.web.app/`

Bibliography

[1] Aartsen, M. G. *et al.*, "Observation of High-Energy Astrophysical Neutrinos in Three Years of IceCube Data", Phys. Rev. Lett., vol. 113, no. 10, p. 101101, Sep. 2014.

[2] Abbasi, R. *et al.*, "Search for Quantum Gravity Using Astrophysical Neutrino Flavour with IceCube", arXiv e-prints, arXiv:2111.04654, Nov. 2021.

[3] Abbott, B. P. *et al.*, "GW170817: Observation of Gravitational Waves from a Binary Neutron Star Inspiral", Phys. Rev. Lett., vol. 119, no. 16, p. 161101, Oct. 2017.

[4] Abbott, B. P. *et al.*, "Multi-messenger Observations of a Binary Neutron Star Merger", ApJ, vol. 848, no. 2, p. L12, Oct. 2017.

[5] Abbott, B. P. *et al.*, "Prospects for observing and localizing gravitational-wave transients with Advanced LIGO, Advanced Virgo and KAGRA", Living Reviews in Relativity, vol. 21, no. 1, p. 3, Apr. 2018.

[6] Abbott, R. *et al.*, "GWTC-3: Compact Binary Coalescences Observed by LIGO and Virgo During the Second Part of the Third Observing Run", arXiv e-prints, arXiv:2111.03606, Nov. 2021.

[7] Abbott, R. *et al.*, "Observation of Gravitational Waves from Two Neutron Star-Black Hole Coalescences", ApJ, vol. 915, no. 1, p. L5, Jul. 2021.

[8] Abdo, A. A. *et al.*, "A limit on the variation of the speed of light arising from quantum gravity effects", Nature, vol. 462, no. 7271, p. 331, Nov. 2009.

[9] Abdollahi, S. *et al.*, "The Second Catalog of Flaring Gamma-Ray Sources from the Fermi All-sky Variability Analysis", ApJ, vol. 846, no. 1, p. 34, Sep. 2017.

[10] Aharonian, F. *et al.*, "Observations of the Crab Nebula with H.E.S.S", A&A, vol. 457, p. 899, Sep. 2006.

[11] Ahlers, M. and Mertsch, P., "Origin of small-scale anisotropies in Galactic cosmic rays", Progress in Particle and Nuclear Physics, vol. 94, p. 184, May 2017.

[12] Ahnen, M. L. *et al.*, "Detection of very high energy gamma-ray emission from the gravitationally-lensed blazar QSO B0218+357 with the MAGIC telescopes", A&A, vol. 595, A98, Nov. 2016.

[13] Ajello, M. *et al.*, "The Fourth Catalog of Active Galactic Nuclei Detected by the Fermi Large Area Telescope", ApJ, vol. 892, no. 2, p. 105, Apr. 2020.

[14] Albert, A. *et al.*, "Constraints on Lorentz Invariance Violation from HAWC Observations of Gamma Rays above 100 TeV", Phys. Rev. Lett., vol. 124, no. 13, p. 131101, Apr. 2020.

[15] Alfaro, J., Morales-Técotl, H. A., and Urrutia, L. F., "Loop quantum gravity and light propagation", Phys. Rev. D, vol. 65, no. 10, p. 103509, May 2002.

[16] Alves Batista, R. and Saveliev, A., "The Gamma-Ray Window to Intergalactic Magnetism", Universe, vol. 7, no. 7, p. 223, Jul. 2021.

[17] Alves Batista, R. *et al.*, "CRPropa 3.2: a framework for high-energy astroparticle propagation", in *37th International Cosmic Ray Conference. 12-23 July 2021. Berlin*, Mar. 2022, p. 978.

[18] Angioni, R., Nesci, R., Finke, J. D., Buson, S., and Ciprini, S., "The large gamma-ray flare of the flat-spectrum radio quasar PKS 0346-27", A&A, vol. 627, A140, Jul. 2019.

[19] Ashkar, H. *et al.*, "The H.E.S.S. gravitational wave rapid follow-up program", J. Cosmology Astropart. Phys., vol. 2021, no. 3, p. 045, Mar. 2021.

[20] Astropy Collaboration and more, "The Astropy Project: Building an Open-science Project and Status of the v2.0 Core Package", AJ, vol. 156, no. 3, p. 123, Sep. 2018.

[21] Baker, J. C., Hunstead, R. W., Kapahi, V. K., and Subrahmanya, C. R., "The Molonglo Reference Catalog 1 JY Radio Source Survey. IV. Optical Spectroscopy of a Complete Quasar Sample", ApJS, vol. 122, no. 1, p. 29, May 1999.

[22] Barthelmy, S. D. *et al.*, "GRB Coordinates Network (GCN): A status report", in *Gamma-ray Bursts, 5th Huntsville Symposium*, ser. American Institute of Physics Conference Series, vol. 526, Sep. 2000, p. 731.

[23] Bartos, I. and Kowalski, M., *Multimessenger Astronomy*. IOP ebooks. Bristol, UK: IOP Publishing, 2017.

[24] Becker Tjus, J. and Merten, L., "Closing in on the origin of Galactic cosmic rays using multimessenger information", Phys. Rep., vol. 782, p. 1, Feb. 2020.

[25] Becker Tjus, J. *et al.*, "Propagation of Cosmic Rays in Plasmoids of AGN Jets-Implications for Multimessenger Predictions", Physics, vol. 4, no. 2, p. 473, Apr. 2022.

[26] Bell, A. R., Matthews, J. H., and Blundell, K. M., "Cosmic ray acceleration by shocks: spectral steepening due to turbulent magnetic field amplification", MNRAS, vol. 488, no. 2, p. 2466, Sep. 2019.

[27] Bell, A. R., Matthews, J. H., Blundell, K. M., and Araudo, A. T., "Cosmic ray acceleration in hydromagnetic flux tubes", MNRAS, vol. 487, no. 4, p. 4571, Aug. 2019.

[28] Belov, A., Garcia, H., Kurt, V., and Mavromichalaki, E., "Proton events and x-ray flares in the last three solar cycles", Cosmic Research, vol. 43, no. 3, p. 165, May 2005.

[29] Beresnyak, A. and Lazarian, A., "MHD Turbulence, Turbulent Dynamo and Applications", in *Magnetic Fields in Diffuse Media*, ser. Astrophysics and Space Science Library, vol. 407, Jan. 2015, p. 163.

[30] Berge, D., Funk, S., and Hinton, J., "Background modelling in very-high-energy γ-ray astronomy", A&A, vol. 466, no. 3, p. 1219, May 2007.

[31] Bieber, J. W. and Matthaeus, W. H., "Perpendicular diffusion and drift at intermediate cosmic-ray energies", ApJ, vol. 485, no. 2, p. 655, Aug. 1997.

[32] Biermann, P. L. *et al.*, "The Origin of Cosmic Rays: Explosions of Massive Stars with Magnetic Winds and Their Supernova Mechanism", ApJ, vol. 725, no. 1, p. 184, Dec. 2010.

[33] Blumenthal, G. R. and Gould, R. J., "Bremsstrahlung, Synchrotron Radiation, and Compton Scattering of High-Energy Electrons Traversing Dilute Gases", Reviews of Modern Physics, vol. 42, no. 2, p. 237, Jan. 1970.

[34] Boch, T. and Fernique, P., "Aladin Lite: Embed your Sky in the Browser", in *Astronomical Data Analysis Software and Systems XXIII*, ser. Astronomical Society of the Pacific Conference Series, vol. 485, May 2014, p. 277.

[35] Boris, J. P. and Shanny, R. A., *Proceedings: fourth conference on numerical simulation of plasmas, November 2, 3, 1970*. Naval Research Laboratory, 1972.

[36] Böttcher, M., Reimer, A., Sweeney, K., and Prakash, A., "Leptonic and Hadronic Modeling of Fermi-detected Blazars", ApJ, vol. 768, no. 1, p. 54, May 2013.

[37] Bouyahiaoui, M., Kachelriess, M., and Semikoz, D. V., "Vela as the source of Galactic cosmic rays above 100 TeV", J. Cosmology Astropart. Phys., vol. 2019, no. 1, p. 046, Jan. 2019.

[38] Buffie, K., Heesen, V., and Shalchi, A., "Theoretical Explanation of the Cosmic-Ray Perpendicular Diffusion Coefficient in the Nearby Starburst Galaxy NGC 253", ApJ, vol. 764, no. 1, p. 37, Feb. 2013.

[39] Burd, P. R. *et al.*, "Ornstein-Uhlenbeck parameter extraction from light curves of Fermi-LAT observed blazars", A&A, vol. 645, A62, Jan. 2021.

[40] Candia, J. and Roulet, E., "Diffusion and drift of cosmic rays in highly turbulent magnetic fields", J. Cosmology Astropart. Phys., vol. 2004, no. 10, p. 007, Oct. 2004.

[41] Cash, J. R. and Karp, A. H., "A variable order runge-kutta method for initial value problems with rapidly varying right-hand sides", ACM Trans. Math. Softw., vol. 16, no. 3, p. 201, Sep. 1990.

[42] Casse, F., Lemoine, M., and Pelletier, G., "Transport of cosmic rays in chaotic magnetic fields", Phys. Rev. D, vol. 65, no. 2, p. 023002, Dec. 2001.

[43] Cerruti, M., Zech, A., Boisson, C., and Inoue, S., "A hadronic origin for ultra-high-frequency-peaked BL Lac objects", MNRAS, vol. 448, no. 1, p. 910, Mar. 2015.

[44] Cliver, E. W., Ling, A. G., Belov, A., and Yashiro, S., "Size distributions of solar flares and solar energetic particle events", ApJ, vol. 756, no. 2, p. L29, Sep. 2012.

[45] Codling, E. A., Plank, M. J., and Benhamou, S., "Random walk models in biology", Journal of The Royal Society Interface, vol. 5, no. 25, p. 813, Apr. 2008.

[46] Cohen, A. G. and Glashow, S. L., "Pair Creation Constrains Superluminal Neutrino Propagation", Phys. Rev. Lett., vol. 107, no. 18, p. 181803, Oct. 2011.

[47] Cruz-Osorio, A. *et al.*, "State-of-the-art energetic and morphological modelling of the launching site of the M87 jet", Nature Astronomy, Nov. 2021.

[48] de Naurois, M. and Rolland, L., "A high performance likelihood reconstruction of γ-rays for imaging atmospheric Cherenkov telescopes", ApJ, vol. 32, no. 5, p. 231, Dec. 2009.

[49] Deligny, O., "Transport of Charged Particles Propagating in Turbulent Magnetic Fields as a Red-noise Process", ApJ, vol. 920, no. 2, p. 87, Oct. 2021.

[50] DeMarco, D., Blasi, P., and Stanev, T., "Numerical propagation of high energy cosmic rays in the Galaxy: I. Technical issues", J. Cosmology Astropart. Phys., vol. 2007, no. 6, p. 027, Jun. 2007.

[51] Dermer, C. D., Murase, K., and Inoue, Y., "Photopion production in black-hole jets and flat-spectrum radio quasars as PeV neutrino sources", Journal of High Energy Astrophysics, vol. 3, p. 29, Sep. 2014.

[52] Desiati, P. and Zweibel, E. G., "The Transport of Cosmic Rays Across Magnetic Fieldlines", ApJ, vol. 791, no. 1, p. 51, Aug. 2014.

[53] Diesing, R. and Caprioli, D., "Steep Cosmic-Ray Spectra with Revised Diffusive Shock Acceleration", ApJ, vol. 922, no. 1, p. 1, Nov. 2021.

[54] Dimitrakoudis, S., Mastichiadis, A., Protheroe, R. J., and Reimer, A., "The time-dependent one-zone hadronic model. First principles", A&A, vol. 546, A120, Oct. 2012.

[55] Dorner, D., Mostafá, M., and Satalecka, K., "High-Energy Alerts in the Multi-Messenger Era", Universe, vol. 7, no. 11, p. 393, Oct. 2021.

[56] Douglas, M. R. and Nekrasov, N. A., "Noncommutative field theory", Reviews of Modern Physics, vol. 73, no. 4, p. 977, Oct. 2001.

[57] Drury, L. O., "Review Article: An introduction to the theory of diffusive shock acceleration of energetic particles in tenuous plasmas", Reports on Progress in Physics, vol. 46, no. 8, p. 973, Aug. 1983.

[58] Dundovic, A., Pezzi, O., Blasi, P., Evoli, C., and Matthaeus, W. H., "Novel aspects of cosmic ray diffusion in synthetic magnetic turbulence", Phys. Rev. D, vol. 102, no. 10, p. 103016, Nov. 2020.

[59] Evans, P. A. *et al.*, "Methods and results of an automatic analysis of a complete sample of Swift-XRT observations of GRBs", MNRAS, vol. 397, no. 3, p. 1177, Aug. 2009.

[60] Evoli, C., Gaggero, D., Grasso, D., and Maccione, L., "Cosmic ray nuclei, antiprotons and gamma rays in the galaxy: a new diffusion model", J. Cosmology Astropart. Phys., vol. 2008, no. 10, p. 018, Oct. 2008.

[61] Fatuzzo, M., Melia, F., Todd, E., and Adams, F. C., "High-energy Cosmic-ray Diffusion in Molecular Clouds: A Numerical Approach", ApJ, vol. 725, no. 1, p. 515, Dec. 2010.

[62] Förster, F. *et al.*, "The Automatic Learning for the Rapid Classification of Events (ALeRCE) Alert Broker", AJ, vol. 161, no. 5, p. 242, May 2021.

[63] Friedrich, J., Margazoglou, G., Biferale, L., and Grauer, R., "Multiscale velocity correlations in turbulence and Burgers turbulence: Fusion rules, Markov processes in scale, and multifractal predictions", Phys. Rev. E, vol. 98, no. 2, p. 023104, Aug. 2018.

[64] Gagnon, O. and Moore, G. D., "Limits on Lorentz violation from the highest energy cosmic rays", Phys. Rev. D, vol. 70, no. 6, p. 065002, Sep. 2004.

[65] Galaverni, M. and Sigl, G., "Lorentz violation and ultrahigh-energy photons", Phys. Rev. D, vol. 78, no. 6, p. 063003, Sep. 2008.

[66] Gao, S., Pohl, M., and Winter, W., "On the Direct Correlation between Gamma-Rays and PeV Neutrinos from Blazars", ApJ, vol. 843, no. 2, p. 109, Jul. 2017.

[67] Garrappa, S. *et al.*, "Investigation of Two Fermi-LAT Gamma-Ray Blazars Coincident with High-energy Neutrinos Detected by IceCube", ApJ, vol. 880, no. 2, p. 103, Aug. 2019.

[68] Gerasimov, R., Bhoj, P., and Kislat, F., "New Constraints on Lorentz Invariance Violation from Combined Linear and Circular Optical Polarimetry of Extragalactic Sources", Symmetry, vol. 13, no. 5, p. 880, May 2021.

[69] Giacalone, J. and Jokipii, J. R., "The Transport of Cosmic Rays across a Turbulent Magnetic Field", ApJ, vol. 520, no. 1, p. 204, Jul. 1999.

[70] Giacinti, G., Kachelrieß, M., and Semikoz, D. V., "Reconciling cosmic ray diffusion with Galactic magnetic field models", J. Cosmology Astropart. Phys., vol. 2018, no. 7, p. 051, Jul. 2018.

[71] Ginsburg, A. *et al.*, "astroquery: An Astronomical Web-querying Package in Python", AJ, vol. 157, no. 3, p. 98, Mar. 2019.

[72] Gleeson, L. J., "The equations describing the cosmic-ray gas in the interplanetary region", Planet. Space Sci., vol. 17, p. 31, Jan. 1969.

[73] Goldstein, A. *et al.*, "Evaluation of Automated Fermi GBM Localizations of Gamma-Ray Bursts", ApJ, vol. 895, no. 1, p. 40, May 2020.

[74] Gottlieb, O., Lalakos, A., Bromberg, O., Liska, M., and Tchekhovskoy, A., "Black hole to breakout: 3D GRMHD simulations of collapsar jets reveal a wide range of transients", MNRAS, vol. 510, no. 4, p. 4962, Mar. 2022.

[75] Grinberg, M., *Flask web development: developing web applications with python*. O'Reilly Media, Inc., 2018.

[76] Guenduez, M., Becker Tjus, J., Ferrière, K., and Dettmar, R., "A novel analytical model of the magnetic field configuration in the Galactic center", A&A, vol. 644, A71, Dec. 2020.

[77] H. E. S. S. Collaboration *et al.*, "H.E.S.S. and MAGIC observations of a sudden cessation of a very-high-energy γ-ray flare in PKS 1510–089 in May 2016", A&A, vol. 648, A23, Apr. 2021.

[78] H. E. S. S. Collaboration, "Time-resolved hadronic particle acceleration in the recurrent nova RS Ophiuchi", Science, vol. 376, no. 6588, p. 77, Apr. 2022.

[79] Halzen, F., Kheirandish, A., Weisgarber, T., and Wakely, S. P., "On the Neutrino Flares from the Direction of TXS 0506+056", ApJ, vol. 874, no. 1, p. L9, Mar. 2019.

[80] Harari, D., Mollerach, S., and Roulet, E., "Anisotropies of ultrahigh energy cosmic rays diffusing from extragalactic sources", Phys. Rev. D, vol. 89, no. 12, p. 123001, Jun. 2014.

[81] Harris, C. R. *et al.*, "Array programming with NumPy", Nature, vol. 585, no. 7825, p. 357, Sep. 2020.

[82] Hawkins, M. R. S., "Timescale of variation and the size of the accretion disc in active galactic nuclei", A&A, vol. 462, no. 2, p. 581, Feb. 2007.

[83] Herbst, K., Papaioannou, A., Banjac, S., and Heber, B., "From solar to stellar flare characteristics. On a new peak size distribution for G-, K-, and M-dwarf star flares", A&A, vol. 621, A67, Jan. 2019.

[84] Hillas, A. M., "The Origin of Ultra-High-Energy Cosmic Rays", ARA&A, vol. 22, p. 425, Jan. 1984.

[85] Hodgkin, S. T. *et al.*, "Gaia Early Data Release 3. Gaia photometric science alerts", A&A, vol. 652, A76, Aug. 2021.

[86] Hoerbe, M. R., Morris, P. J., Cotter, G., and Becker Tjus, J., "On the relative importance of hadronic emission processes along the jet axis of active galactic nuclei", MNRAS, vol. 496, no. 3, p. 2885, Aug. 2020.

[87] Hunter, J. D., "Matplotlib: A 2D Graphics Environment", Computing in Science and Engineering, vol. 9, no. 3, p. 90, May 2007.

[88] IceCube Collaboration, "Evidence for High-Energy Extraterrestrial Neutrinos at the IceCube Detector", Science, vol. 342, no. 6161, p. 1242856, Nov. 2013.

[89] IceCube Collaboration *et al.*, "Multimessenger observations of a flaring blazar coincident with high-energy neutrino IceCube-170922A", Science, vol. 361, no. 6398, eaat1378, Jul. 2018.

[90] IceCube Collaboration, "Neutrino interferometry for high-precision tests of Lorentz symmetry with IceCube", Nature Physics, vol. 14, no. 9, p. 961, Jul. 2018.

[91] Jansson, R. and Farrar, G. R., "A new model of the Galactic magnetic field", ApJ, vol. 757, no. 1, p. 14, Sep. 2012.

[92] Jokipii, J. R., "Cosmic-Ray Propagation. I. Charged Particles in a Random Magnetic Field", ApJ, vol. 146, p. 480, Nov. 1966.

[93] Jokipii, J. R. and Morfill, G. E., "Ultra-high-energy cosmic rays in a galactic wind and its termination shock", ApJ, vol. 312, p. 170, Jan. 1987.

[94] Jokipii, J. R. and Parker, E. N., "Stochastic Aspects of Magnetic Lines of Force with Application to Cosmic-Ray Propagation", ApJ, vol. 155, p. 777, Mar. 1969.

[95] Katrin Collaboration *et al.*, "Direct neutrino-mass measurement with sub-electronvolt sensitivity", Nature Physics, vol. 18, no. 2, p. 160, Feb. 2022.

[96] Kleimann, J., Schorlepp, T., Merten, L., and Becker Tjus, J., "Solenoidal improvements for the jf12 Galactic magnetic field model", ApJ, vol. 877, no. 2, p. 76, Jun. 2019.

[97] Kotera, K. and Lemoine, M., "Inhomogeneous extragalactic magnetic fields and the second knee in the cosmic ray spectrum", Phys. Rev. D, vol. 77, no. 2, p. 023005, Jan. 2008.

[98] Kotera, K. and Olinto, A. V., "The Astrophysics of Ultrahigh-Energy Cosmic Rays", ARA&A, vol. 49, no. 1, p. 119, Sep. 2011.

[99] Krimm, H. A. *et al.*, "The Swift/BAT Hard X-Ray Transient Monitor", ApJS, vol. 209, no. 1, p. 14, Nov. 2013.

[100] Kun, E. *et al.*, "Cosmic Neutrinos from Temporarily Gamma-suppressed Blazars", ApJ, vol. 911, no. 2, p. L18, Apr. 2021.

[101] Lagage, P. O. and Cesarsky, C. J., "Cosmic-ray shock acceleration in the presence of self-excited waves", A&A, vol. 118, no. 2, p. 223, Feb. 1983.

[102] Lenain, J. P., "FLaapLUC: A pipeline for the generation of prompt alerts on transient Fermi-LAT γ-ray sources", Astronomy and Computing, vol. 22, p. 9, Jan. 2018.

[103] Lewis, T. R., Finke, J. D., and Becker, P. A., "A Steady-state Spectral Model for Electron Acceleration and Cooling in Blazar Jets: Application to 3C 279", ApJ, vol. 853, no. 1, p. 6, Jan. 2018.

[104] Li, T. P. and Ma, Y. Q., "Analysis methods for results in gamma-ray astronomy.", ApJ, vol. 272, p. 317, Sep. 1983.

[105] Lin, H. N., Li, X., and Chang, Z., "Gamma-ray burst polarization reduction induced by the Lorentz invariance violation", MNRAS, vol. 463, no. 1, p. 375, Nov. 2016.

[106] Litvinenko, Y. E. and Schlickeiser, R., "The telegraph equation for cosmic-ray transport with weak adiabatic focusing", A&A, vol. 554, A59, Jun. 2013.

[107] Litvinenko, Y. E., Effenberger, F., and Schlickeiser, R., "The Telegraph Approximation for Focused Cosmic-Ray Transport in the Presence of Boundaries", ApJ, vol. 806, no. 2, p. 217, Jun. 2015.

[108] Litvinenko, Y. E. and Noble, P. L., "A Numerical Study of Diffusive Cosmic-Ray Transport with Adiabatic Focusing", ApJ, vol. 765, no. 1, p. 31, Mar. 2013.

[109] Mace, R. L., Matthaeus, W. H., and Bieber, J. W., "Numerical Investigation of Perpendicular Diffusion of Charged Test Particles in Weak Magnetostatic Slab Turbulence", ApJ, vol. 538, no. 1, p. 192, Jul. 2000.

[110] Madore, B. F. *et al.*, "The NASA/IPAC Extragalactic Database", in *Astronomical Data Analysis Software and Systems I*, ser. Astronomical Society of the Pacific Conference Series, vol. 25, Jan. 1992, p. 47.

[111] MAGIC Collaboration *et al.*, "Constraining Lorentz Invariance Violation Using the Crab Pulsar Emission Observed up to TeV Energies by MAGIC", ApJS, vol. 232, no. 1, p. 9, Sep. 2017.

[112] MAGIC Collaboration *et al.*, "Gamma rays reveal proton acceleration in thermonuclear novae explosions", arXiv e-prints, arXiv:2202.07681, Feb. 2022.

[113] Magnier, E. A. *et al.*, "The Pan-STARRS Data-processing System", ApJS, vol. 251, no. 1, p. 3, Nov. 2020.

[114] Matthaeus, W. H., Qin, G., Bieber, J. W., and Zank, G. P., "Nonlinear collisionless perpendicular diffusion of charged particles", ApJ, vol. 590, no. 1, p. L53, May 2003.

[115] McKinney, W., "Data Structures for Statistical Computing in Python", in *Proceedings of the 9th Python in Science Conference*, 2010, p. 56.

[116] Mereghetti, S. *et al.*, "INTEGRAL Discovery of a Burst with Associated Radio Emission from the Magnetar SGR 1935+2154", ApJ, vol. 898, no. 2, p. L29, Aug. 2020.

[117] Mereghetti, S., "Ten years of the INTEGRAL Burst Alert System (IBAS)", PoS, vol. INTEGRAL2012, p. 126, 2013.

[118] Merín, B. *et al.*, "ESA Sky: a new Astronomy Multi-Mission Interface", arXiv e-prints, arXiv:1512.00842, Dec. 2015.

[119] Merten, L., Becker Tjus, J., Fichtner, H., Eichmann, B., and Sigl, G., "CR-Propa 3.1—a low energy extension based on stochastic differential equations", J. Cosmology Astropart. Phys., vol. 2017, no. 6, p. 046, Jun. 2017.

[120] Miceli, D. *et al.*, "Following up GW alerts with MAGIC: the third LIGO/Virgo observation run", in *ICRC2019*, vol. 36, Jul. 2019, p. 743.

[121] Minnie, J., Bieber, J. W., Matthaeus, W. H., and Burger, R. A., "On the ability of different diffusion theories to account for directly simulated diffusion coefficients", ApJ, vol. 663, no. 2, p. 1049, 2007.

[122] Minnie, J., Matthaeus, W. H., Bieber, J. W., Ruffolo, D., and Burger, R. A., "When do particles follow field lines?", Journal of Geophysical Research (Space Physics), vol. 114, no. A1, A01102, Jan. 2009.

[123] Möller, A. *et al.*, "FINK, a new generation of broker for the LSST community", MNRAS, vol. 501, no. 3, p. 3272, Mar. 2021.

[124] Morse, P. M. and Feshbach, H., *Methods of theoretical physics*. International Series in Pure and Applied Physics, New York: McGraw-Hill, 1953.

[125] Murase, K., Guetta, D., and Ahlers, M., "Hidden Cosmic-Ray Accelerators as an Origin of TeV-PeV Cosmic Neutrinos", Phys. Rev. Lett., vol. 116, no. 7, p. 071101, Feb. 2016.

[126] Nigro, C. *et al.*, "agnpy: An open-source python package modelling the radiative processes of jetted active galactic nuclei", A&A, vol. 660, A18, Apr. 2022.

[127] Nordin, J. *et al.*, "Transient processing and analysis using AMPEL: alert management, photometry, and evaluation of light curves", A&A, vol. 631, A147, Nov. 2019.

[128] Observatory, C. T. A. and Consortium, C. T. A., "CTAO Instrument Response Functions - prod5 version v0.1", version v0.1, Zenodo, Sep. 2021.

[129] Ohm, S. and Hoischen, C., "On the expected γ-ray emission from nearby flaring stars", MNRAS, vol. 474, no. 1, p. 1335, Oct. 2017.

[130] Onken, C. A. *et al.*, "SkyMapper Southern Survey: Second data release (DR2)", PASA, vol. 36, e033, Aug. 2019.

[131] Ostrowski, M. and Siemieniec-Oziebło, G., "Diffusion in momentum space as a picture of second-order Fermi acceleration", ApJ, vol. 6, no. 3-4, p. 271, Mar. 1997.

[132] Papaioannou, A. *et al.*, "Solar flares, coronal mass ejections and solar energetic particle event characteristics", Journal of Space Weather and Space Climate, vol. 6, no. 27, A42, Dec. 2016.

[133] Pérez, F. and Granger, B. E., "IPython: A system for interactive scientific computing", Computing in Science and Engineering, vol. 9, no. 3, p. 21, May 2007.

[134] Petroff, E. *et al.*, "VOEvent Standard for Fast Radio Bursts", arXiv e-prints, arXiv:1710.08155, Oct. 2017.

[135] Plotnikov, I., Pelletier, G., and Lemoine, M., "Particle transport in intense small-scale magnetic turbulence with a mean field", A&A, vol. 532, A68, Aug. 2011.

[136] Potter, W. J. and Cotter, G., "Synchrotron and inverse-Compton emission from blazar jets - I. A uniform conical jet model", MNRAS, vol. 423, no. 1, p. 756, Jun. 2012.

[137] Qin, H. *et al.*, "Why is Boris algorithm so good?", Physics of Plasmas, vol. 20, no. 8, p. 084503, Aug. 2013.

[138] Reichherzer, P. and Becker Tjus, J., "Efficient charged particle propagation methods", arXiv e-prints, arXiv:2204.08784, Apr. 2022.

[139] Reichherzer, P., Becker Tjus, J., Zweibel, E. G., Merten, L., and Pueschel, M. J., "Anisotropic cosmic ray diffusion in isotropic Kolmogorov turbulence", MNRAS, vol. 514, no. 2, p. 2658, Aug. 2022.

[140] Reichherzer, P., Becker Tjus, J., Zweibel, E. G., Merten, L., and Pueschel, M. J., "Turbulence-level dependence of cosmic ray parallel diffusion", MNRAS, vol. 498, no. 4, p. 5051, Nov. 2020.

[141] Reichherzer, P., Schüssler, F., Lefranc, V., Alkan, A., and Becker Tjus, J., "Realtime alerts of the transient sky on mobile devices", arXiv e-prints, arXiv:2111.05427, Nov. 2021.

[142] Reichherzer, P. and Tjus, J., "PropPy - Correlated random walk propagation of cosmic rays in magnetic turbulence", The Journal of Open Source Software, vol. 7, no. 74, p. 4243, Jun. 2022.

[143] Reichherzer, P. *et al.*, "Astro-COLIBRI-The COincidence LIBrary for Real-time Inquiry for Multimessenger Astrophysics", ApJS, vol. 256, no. 1, p. 5, Sep. 2021.

[144] Reichherzer, P. *et al.*, "Cosmic-ray transport in blazars: diffusive or ballistic propagation?", in *37th International Cosmic Ray Conference. 12-23 July 2021. Berlin*, Mar. 2022, p. 468.

[145] Reichherzer, P. *et al.*, "Regimes of cosmic-ray diffusion in Galactic turbulence", SN Applied Sciences, vol. 4, p. 15, Jan. 2022.

[146] Reichherzer, P., "Calculation of the diffusion tensor for the galactic magnetic field", Master thesis at Ruhr-University Bochum, Nov. 2018.

[147] Reichherzer, P., "Comparison of propagation tools crpropa and proppy", Zenodo, Feb. 2022.

[148] Reynolds, C. S., Fabian, A. C., Celotti, A., and Rees, M. J., "The matter content of the jet in m87: Evidence for an electron—positronjet", MNRAS, vol. 283, no. 3, p. 873, Jul. 1996.

[149] Rodrigues, X., Gao, S., Fedynitch, A., Palladino, A., and Winter, W., "Leptohadronic Blazar Models Applied to the 2014-2015 Flare of TXS 0506+056", ApJ, vol. 874, no. 2, p. L29, Apr. 2019.

[150] Rutledge, R. E., "The Astronomer's Telegram: A Web-based Short-Notice Publication System for the Professional Astronomical Community", PASP, vol. 110, no. 748, p. 754, Jun. 1998.

[151] Rybicki, G. B. and Lightman, A. P., *Radiative processes in astrophysics*. A Wiley-Interscience Publication, New York: Wiley, 1979.

[152] Saha, A. *et al.*, "ANTARES: a prototype transient broker system", in *Observatory Operations: Strategies, Processes, and Systems V*, ser. Society of Photo-Optical Instrumentation Engineers (SPIE) Conference Series, vol. 9149, Jul. 2014, p. 914908.

[153] Schlegel, L., Frie, A., Eichmann, B., Reichherzer, P., and Becker Tjus, J., "Interpolation of Turbulent Magnetic Fields and Its Consequences on Cosmic Ray Propagation", ApJ, vol. 889, no. 2, p. 123, Feb. 2020.

[154] Schlickeiser, R., *Cosmic Ray Astrophysics*. Astronomy, Astrophysics Library; Physics, and Astronomy Online Library. Berlin: Springer, 2002.

[155] Schröder, F. G. *et al.*, "High-Energy Galactic Cosmic Rays (Astro2020 Science White Paper)", arXiv e-prints, arXiv:1903.07713, Mar. 2019.

[156] Schüssler, F., Alkan, A. K., Lefranc, V., and Reichherzer, P., "Astro-COLIBRI: a new platform for real-time multi-messenger astrophysics", in *37th International Cosmic Ray Conference. 12-23 July 2021. Berlin*, Mar. 2022, p. 935.

[157] Seta, A., "Cosmic ray propagation in turbulent galactic magnetic fields", PhD thesis published at Newcastle University, 2019.

[158] Shalchi, A., "Field line random walk in magnetic turbulence", Physics of Plasmas, vol. 28, no. 12, p. 120501, Dec. 2021.

[159] Shalchi, A., Skoda, T., Tautz, R. C., and Schlickeiser, R., "Analytical description of nonlinear cosmic ray scattering: isotropic and quasilinear regimes of pitch-angle diffusion", A&A, vol. 507, no. 2, p. 589, Nov. 2009.

[160] Shalchi, A., "Nonlinear cosmic ray diffusion theories", Springer-Verlag, Berlin, Heidelberg, vol. 362, Jan. 2009.

[161] Shalchi, A., "Perpendicular Transport of Energetic Particles in Magnetic Turbulence", Space Sci. Rev., vol. 216, no. 2, p. 23, Feb. 2020.

[162] Shukurov, A., Rodrigues, L. F. S., Bushby, P. J., Hollins, J., and Rachen, J. P., "A physical approach to modelling large-scale galactic magnetic fields", A&A, vol. 623, A113, Mar. 2019.

[163] Shukurov, A., Snodin, A. P., Seta, A., Bushby, P. J., and Wood, T. S., "Cosmic Rays in Intermittent Magnetic Fields", ApJ, vol. 839, no. 1, p. L16, Apr. 2017.

[164] Smith, K. W. *et al.*, "Lasair: The Transient Alert Broker for LSST:UK", Research Notes of the American Astronomical Society, vol. 3, no. 1, p. 26, Jan. 2019.

[165] Smith, M. W. E. *et al.*, "The Astrophysical Multimessenger Observatory Network (AMON)", ApJ, vol. 45, p. 56, May 2013.

[166] Snodin, A. P., Shukurov, A., Sarson, G. R., Bushby, P. J., and Rodrigues, L. F. S., "Global diffusion of cosmic rays in random magnetic fields", MNRAS, vol. 457, no. 4, p. 3975, Apr. 2016.

[167] Sonsrettee, W. *et al.*, "Magnetic Field Line Random Walk in Isotropic Turbulence with Varying Mean Field", ApJS, vol. 225, no. 2, p. 20, Aug. 2016.

[168] Staley, T. D. and Fender, R., "The 4 Pi Sky Transient Alerts Hub", arXiv e-prints, arXiv:1606.03735, Jun. 2016.

[169] Stecker, F. W. and Glashow, S. L., "New tests of Lorentz invariance following from observations of the highest energy cosmic /γ-rays", Astroparticle Physics, vol. 16, no. 1, p. 97, Oct. 2001.

[170] Stein, R. *et al.*, "A tidal disruption event coincident with a high-energy neutrino", Nature Astronomy, vol. 5, p. 510, Jan. 2021.

[171] Strong, A. W. and Moskalenko, I. V., "Propagation of Cosmic-Ray Nucleons in the Galaxy", ApJ, vol. 509, no. 1, p. 212, Dec. 1998.

[172] Subedi, P. *et al.*, "Charged Particle Diffusion in Isotropic Random Magnetic Fields", ApJ, vol. 837, no. 2, p. 140, Mar. 2017.

[173] Swinbank, J., "Comet: A VOEvent broker", Astronomy and Computing, vol. 7, p. 12, Nov. 2014.

[174] Tautz, R. C. and Dosch, A., "On numerical turbulence generation for test-particle simulations", Physics of Plasmas, vol. 20, no. 2, p. 022302, Feb. 2013.

[175] Tautz, R. C. and Lerche, I., "Application of the three-dimensional telegraph equation to cosmic-ray transport", Research in Astronomy and Astrophysics, vol. 16, no. 10, p. 162, Oct. 2016.

[176] Terral, P. and Ferrière, K., "Constraints from Faraday rotation on the magnetic field structure in the Galactic halo", A&A, vol. 600, A29, Apr. 2017.

[177] Unger, M., Farrar, G. R., and Anchordoqui, L. A., "Origin of the ankle in the ultrahigh energy cosmic ray spectrum, and of the extragalactic protons below it", Phys. Rev. D, vol. 92, no. 12, p. 123001, Dec. 2015.

[178] Vasileiou, V. *et al.*, "Constraints on Lorentz invariance violation from Fermi-Large Area Telescope observations of gamma-ray bursts", Phys. Rev. D, vol. 87, no. 12, p. 122001, Jun. 2013.

[179] Virtanen, P. *et al.*, "SciPy 1.0: Fundamental Algorithms for Scientific Computing in Python", Nature Methods, vol. 17, p. 261, Feb. 2020.

[180] von Kienlin, A. *et al.*, "The Fourth Fermi-GBM Gamma-Ray Burst Catalog: A Decade of Data", ApJ, vol. 893, no. 1, p. 46, Apr. 2020.

[181] Wakely, S. P. and Horan, D., "TeVCat: An online catalog for Very High Energy Gamma-Ray Astronomy", in *International Cosmic Ray Conference*, ser. International Cosmic Ray Conference, vol. 3, Jan. 2008, p. 1341.

[182] Wardle, J. F. C., Homan, D. C., Ojha, R., and Roberts, D. H., "Electron–positron jets associated with the quasar 3c279", Nature, vol. 395, no. 6701, p. 457, Oct. 1998.

[183] Wenger, M. *et al.*, "The SIMBAD astronomical database. The CDS reference database for astronomical objects", A&AS, vol. 143, p. 9, Apr. 2000.

[184] White, G. L. *et al.*, "Redshifts of Southern Radio Sources. VII.", ApJ, vol. 327, p. 561, Apr. 1988.

[185] Woosley, S. E. and Bloom, J. S., "The Supernova Gamma-Ray Burst Connection", ARA&A, vol. 44, no. 1, p. 507, Sep. 2006.

[186] AL-Zetoun, A. and Achterberg, A., "The effects of drift and winds on the propagation of Galactic cosmic rays", MNRAS, vol. 504, no. 4, p. 6067, Jul. 2021.

[187] Zhang, B., "The delay time of gravitational wave — gamma-ray burst associations", Frontiers of Physics, vol. 14, no. 6, p. 64402, Dec. 2019.

[188] Zimbardo, G., Perri, S., Effenberger, F., and Fichtner, H., "Fractional Parker equation for the transport of cosmic rays: steady-state solutions", A&A, vol. 607, A7, Oct. 2017.

[189] Zweibel, E. G., "The microphysics and macrophysics of cosmic rays", Physics of Plasmas, vol. 20, no. 5, p. 055501, May 2013.

Appendix A

Multi-Messenger Approach to Investigate Effects of Lorentz Invariance Violation

Lorentz invariance is a pillar of special relativity. Its predictions passed any laboratory or astrophysical test. However, various theories [15, 56] attempting to generalize general relativity and quantum theory invoke Lorentz invariance violation (LIV) at Planck scales through modifications of the Standard Theory Lagrangian. This change introduces the energy-dependent velocity of massless particles in a vacuum.

Laboratory experiments have provided constraints for LIV, which are nowadays outpaced by advances in astronomical observations due to the commissioning of ever more advanced observatories. By shifting the window of the observable particles towards higher energies and more distant sources, the tiny LIV effects accumulate to potentially detectable signatures.

Figure A.1 summarizes relevant LIV effects for messengers from gamma-ray bursts (GRBs), as this source class is particularly suitable for studying LIV given their large distances. Tests of LIV include studies of particle time-delay in arrival times during flares [8, 111, 178], vacuum Cherenkov radiation [46, 64, 65], photon and neutrino splitting and decay [14, 169], polarisation change [68, 105], anomalous neutrino flavour conversion [2], and studies of a Lorentz violating field [90]. The limits emerging from these tests for the first-order LIV energy scale extend five orders of magnitude above the Planck scale. Future telescopes and a larger statistic of observations of particularly extreme and distant flares will probe even higher magnitudes.

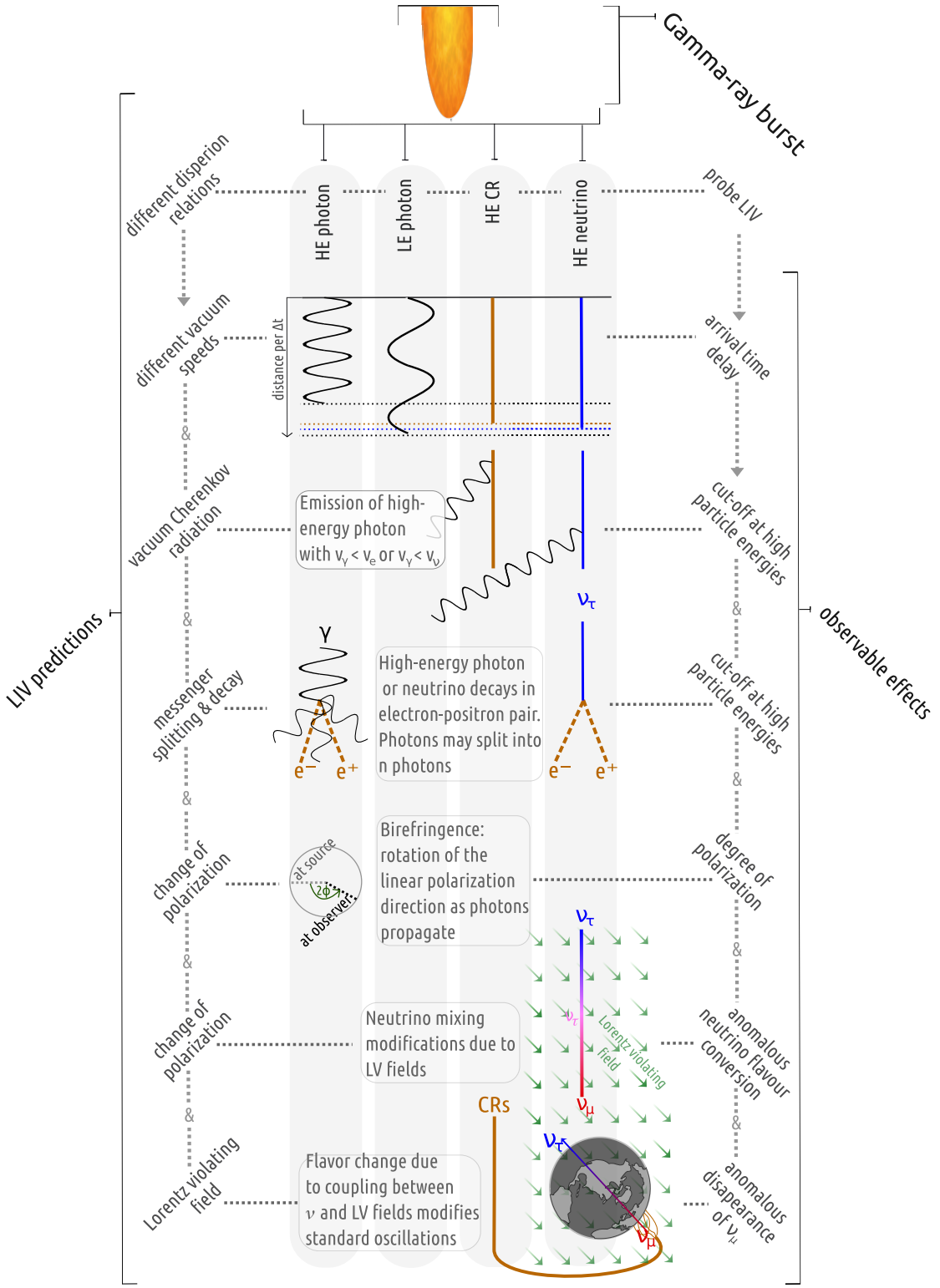

Figure A.1: Schematic summary of LIV effects of different low- (LE) and high-energy (HE) messengers from GRBs and their observable effects.

Acknowledgement

I want to express my profound gratitude to all those who supported me during my thesis. First, I would like to thank primarily my family, i.e., my parents, brothers, and grandparents, but most of all, my wife Julia, for your continuous emotional support and truly endlessly loving me.

Furthermore, likely without being complete, I wish to thank:

Supervision Julia and Fabian, for being such a source of inspiration and expertise and for your exceptional supervision. Both complemented each other and created the perfect balance between independence and guidance. Julia, for your trust in my working ethos and choice of topics, even if not everything found its way into publications, like my M-dwarf study :) I am thrilled to be part of your chair as a research assistant for the following months. I want to thank Fabian for creating the startup-compatible environment that drove the rapid development of Astro-COLIBRI and acknowledges him as an outstanding host during my stay in Paris, who always assisted me in finding my way through the slow-grinding mills of bureaucracy. I am especially excited to contribute to Gamma Catcher soon ;-)

Bochum Among the many (former) colleagues and friends at the institute who deserve acknowledgment for the scientific and intellectual exchange, I would like to name Anke, Björn, Frederik, Ilja, Jan-Niklas, Julien, Leander, Lukas, Marcel, Mario, Memo, Vera, and Vladimir. Thank you for the great time! Johan for the time spent together on the soccer field and in the shared office, which provided space for inspiring conversations. Anna for initiating an exchange between the groups about multi-messenger astronomy, proofreading, and supporting me during the international workshop organization. Jens for sharing our servers for time-lasting simulations. Horst for proofreading and supporting me during my Ph.D. thesis. Special thanks to Bernd for rescuing my computer. Behnam and Lorenzo for the great *ART* moments in Bochum and for challenging us in rock climbing.

Paris I want to thank Alessandro, Emmanuel, Hector, Jean-Francois for great canteen moments and for welcoming me far from home. Halim for guiding me through the institute and the valuable talks about H.E.S.S. and follow-up campaigns. Valentin for being keen on brainstorming endlessly about Astro-COLIBRI development, e.g., Flutter provider, streams, and databases, to fix our seemingly never-reducing list of issues and feature requests. Francois for guiding me through H.E.S.S. Paris Analysis. Atilla and Federica, for your contributions to our weekly group meetings. Polina for being keen to pause work for a cup of tea and practice French. Michael for many talks about H.E.S.S. and satirical shows as well as our weekly Pizza lunch in Paris.

Collaborators I want to thank Ellen for keeping up our fruitful collaboration since my research stay in Madison during my Master's thesis. You introduced me to the world of pitch-angle scattering, and you shaped how I think about cosmic rays' microphysics and macrophysics. MJ for really always finding time to answer questions of mine and assisting me not only during the journal-review processes. Volker for providing interesting observational data to test our theoretical CR-transport models. Sarah for inspiring talks about multi-messenger Astrophysics. Among the many from H.E.S.S. who deserve acknowledgment, I want to mention Catherine, Clemens, Dorit, Jean-Philippe, Faical, Felix, Floriane, Markus, Matteo, Stefan O., Stefan W.

Software This work was made possible by the following software packages besides the tools (CRPropa, etc.) already mentioned throughout the thesis: astropy [20], astroquery [71], flask [75], ipython [133], matplotlib [87], numpy [81] and pandas [115], scipy [179], and WolframAlpha.

Funding This work is supported by funding by the BMBF, grant number 05A20PC1. This work is supported by the "ADI 2019" project funded by the IDEX Paris-Saclay, ANR-11-IDEX-0003-02. Furthermore, there was support by the German Academic Exchange Service (DAAD) through the scholarship "Jahresstipendien für Doktorandinnen und Doktoranden bei bi-national betreuten Promotionen" and by the Ruhr-University Bochum (RUB) Research School via the *Project International* funding. Furthermore, I am extremely grateful for the funding from the RUB Research School to organize an international workshop about multi-messenger Astrophysics at the RUB that they granted me after I successfully applied in a competitive call. The workshop is named *1st Astro-COLIBRI Multi-Messenger Astrophysics Workshop*[1] and intends to provide a forum and foster communication within the real-time multi-messenger community. Finally, I would also like to thank the Ruth und Gert Massenberg-Stiftung, Wilhelm und Else Heraeus-Stiftung, and the Stiftung Lindauer Nobelpreisträgertagungen for supporting me intelectually and financially. Without these foundations and grants, the impressions from influential events would be missing that enriched my doctoral studies, such as the Lindau Nobel Laureate meetings and the Falling Walls event in Berlin.

[1] `https://astrophysics-workshop.web.app`